



HAL
open science

Synthesis, characterization, and electronic structure calculations of select families of BN doped polycyclic aromatic hydrocarbons

Chen Zhang

► **To cite this version:**

Chen Zhang. Synthesis, characterization, and electronic structure calculations of select families of BN doped polycyclic aromatic hydrocarbons. Analytical chemistry. Université de Pau et des Pays de l'Adour, 2023. English. NNT : 2023PAUU3006 . tel-04398502

HAL Id: tel-04398502

<https://theses.hal.science/tel-04398502>

Submitted on 16 Jan 2024

HAL is a multi-disciplinary open access archive for the deposit and dissemination of scientific research documents, whether they are published or not. The documents may come from teaching and research institutions in France or abroad, or from public or private research centers.

L'archive ouverte pluridisciplinaire **HAL**, est destinée au dépôt et à la diffusion de documents scientifiques de niveau recherche, publiés ou non, émanant des établissements d'enseignement et de recherche français ou étrangers, des laboratoires publics ou privés.

THÈSE

UNIVERSITE DE PAU ET DES PAYS DE L'ADOUR
École doctorale (SEA)

Présentée et soutenue le (06/04/2023)

par **(Chen ZHANG)**

pour obtenir le grade de docteur
de l'Université de Pau et des Pays de l'Adour

Spécialité: CHIMIE

SYNTHESE, CARACTERISATION ET CALCULS DE LA STRUCTURE ELECTRONIQUE DE CERTAINES FAMILLES D'HYDROCARBURES AROMATIQUES POLYCYCLIQUES DOPES AU BN

MEMBRES DU JURY

RAPPORTEURS

- Holger BETTINGER
- Emmanuel KOUKARAS

Professor / University of Tübingen
Assistant Professor / Aristotle University of Thessaloniki

EXAMINATEURS

- Anna CHROSTOWSKA
- Jean-Francois HALET

Professor / University of Pau and Adour country
Research Director / CNRS – Saint-Gobain – NIMS / Tsukuba

THESIS DIRECTEUR

- Shih-Yuan LIU

Professor / Boston College

SUPERVISEUR

- Panagiotis KARAMANIS

Researcher / University of Pau and Adour country

Synthesis, Characterization, and Electronic Structure Calculations of Select Families
of BN-doped Polycyclic Aromatic Hydrocarbons

Chen Zhang

Advisor: Prof. Shih-Yuan Liu, Dr. Panagiotis Karamanis

Abstract: Boron and nitrogen (BN) containing polycyclic aromatic hydrocarbons have potential applications in materials science. In this dissertation, a new synthetic route for the synthesis of BN-containing arenes complemented by systematic structure-property computational investigations is presented and discussed. The synthetic method developed has been applied to the preparation BN-2,1-naphthalene, a novel parental BN isostere of naphthalene, and some of its derivatives. The proposed strategy is general and could potentially be applied to other BN-doped π systems of larger sizes. The computational work of this thesis is divided into two parts. The first part is devoted to the elucidation of BN doping effects on ground and excited state properties of sixteen BN-doped phenanthrene isomers. The second part deals with the evaluation of molecular properties in BN-doped phenanthrenes functionalized with donor and acceptor groups. The properties of interest comprise ground and excited state geometries, molecular orbitals, aromaticity, dipole moments, vertical and/or adiabatic excitation energies. The computational methods mainly involved density functional theory and ab-initio methods of high predictive precision within the frameworks of coupled cluster and multi-configurational self-consistent field approximations. The obtained results bring into light useful structure-property correlations for the design of BN-doped organic systems in materials applications.

Synthèse, Caractérisation et Calculs de la Structure Électronique de Certaines
Familles d'Hydrocarbures Aromatiques Polycycliques Dopés au BN

Chen Zhang

Directeur de thèse : Prof. Shih-Yuan Liu; Encadrant : Dr. Panagiotis Karamanis

Résumé : Les hydrocarbures aromatiques polycycliques contenant du bore et de l'azote (BN) ont des applications potentielles dans la science des matériaux. Dans cette dissertation, une nouvelle voie de synthèse d'arènes contenant une liaison BN, complétée par des études computationnelles systématiques de la relation structure-propriété, est présentée et discutée. La méthode de synthèse développée a été appliquée à la préparation du BN-2,1-naphtalène, un nouvel isostère BN parental du naphthalène, et de certains de ses dérivés. La stratégie proposée est générale et pourrait potentiellement être appliquée à d'autres systèmes π dopés au BN de taille plus importante. Le travail d'évaluation calculatoire de cette thèse est divisé en deux parties. La première partie est consacrée à l'élucidation des effets du dopage BN sur les propriétés à l'état fondamental et à l'état excité de seize isomères du phénanthrène dopés au BN. La seconde partie traite de l'évaluation des propriétés moléculaires des phénanthrènes dopés au BN et fonctionnalisés avec des groupes donneurs et accepteurs. Les propriétés étudiées comprennent les géométries des états fondamental et excité, les orbitales moléculaires, l'aromaticité, les moments dipolaires, les énergies d'excitation verticales et/ou adiabatiques. Les méthodes de calcul impliquent principalement la théorie de la fonctionnelle de la densité et des méthodes ab-initio d'une grande précision prédictive dans le cadre d'approximations de champs auto-cohérent, couplés et multi-configurationnels. Les résultats obtenus mettent en lumière des corrélations structure-propriétés utiles pour la conception de systèmes organiques dopés au BN pour des applications potentielles.

ACKNOWLEDGEMENTS

First of all, I would like to thank my supervisor Prof. Shih-Yuan Liu for giving me the opportunity to study for my PhD at Université de Pau et des Pays de l'Adour (UPPA). Prof. Liu also invited me to his research group at Boston College for a ten-month long study. During that time, I learned a lot from Prof. Liu's chemistry class and every weekly group meeting. I also want to thank Liu's group members, especially Maxwell Eaton who helped me with the photophysical and X-ray single crystal characterization, Jiangpeng Liu who provided a strategy for my synthetic work, as well as Mario Alvarado and Kevin Byrne. I appreciate for the instrumentation support from Dr. Bo Li and Dr. Thusitha Jayasundera at Boston College.

I also would like to thank my co-supervisor Dr. Panagiotis Karamanis and Prof. Anna Chrostowska. Dr. Panagiotis, we usually call him Panos, always gives me comments and tips in computational chemistry as well as my life. Prof. Anna provided me with numerous administrative supports. Also, thanks to Prof. Anna and Prof. Patrick Baylere for their help with the photoelectronic characterization. I want to thank Dr. Clovis Darrigan for the initial help with the guidance of computational chemistry. I am grateful too to Dr. Stéphane Labat for his support of our laboratory construction. I would like to thank my family, my colleague Danylo Hatych, Yuping Dai and other friends for their encouragement and support.

I would also like to thank the committee members, Prof. Holger Bettinger and Prof. Emmanuei Koukaras, for reading my thesis and for helpful feedback. I also appreciate Dr. Jean-Francois Halet for attending my oral presentation.

List of Abbreviations

CASSCF	Complete active space self-consistent field	MR-TADF	Multiple resonance-induced thermally activated delayed fluorescence
CCSD	Coupled cluster singles and doubles	NBS	N-bromosuccinimide
COSY	Correlated Spectroscopy	NICS	Nucleus-independent chemical shift
DDQ	2,3-dichloro-4,5-dicyanobenzoquinone	NMR	Nuclear magnetic resonance
DFT	Density-functional theory	NTO	Natural transition orbitals
EA	Electron affinity	OFETs	Organic field-effect transistors
ELF	Electron localization function	OLEDs	Organic light-emitting diodes
EOM-CCSD	Equation-of-motion coupled cluster singles and doubles	PAHs	Polycyclic aromatic hydrocarbons
EQE	External quantum efficiency	PDI	Perylene diimide
ESP	Electrostatic potential	RT	Room temperature
FMO	Frontier molecular orbital	SF	Single fission
FWHM	Full width at half maximum	TBAF	Tetrabutylammonium fluoride
HMBC	Heteronuclear multiple-bond correlation	TD-DFT	Time-dependent density functional theory
HOMO	Highest occupied molecular orbital	THF	Tetrahydrofuran
HSQC	Heteronuclear single-quantum correlation	UHF	Unrestricted Hartree-Fock
IE	Ionization energy	UV-PES	Ultraviolet photoelectron spectroscopy
iSF	Intramolecular singlet fission	UV-Vis	Ultraviolet-visible
LUMO	Lowest unoccupied molecular orbital		

TABLE OF CONTENTS

Chapter 1	BN-2,1-naphthalenes.....	1
1.1	Introduction: BN/CC Isosterism and BN-doped Polycyclic Aromatic Hydrocarbons (PAHs).....	1
1.2	BN-2,1-naphthalene: Synthesis and Characterization	18
1.2.1	Synthesis of BN-2,1-naphthalene	19
1.2.2	Optoelectronic Properties of BN-2,1-naphthalenes	21
1.2.3	Single-Crystal X-Ray Structures of BN-2,1-Naphthalenes.	28
1.3	Conclusion	31
1.4	Experimental Section	32
	Reference	52
Chapter 2	Electronic Structure Calculations of BN-doped Phenanthrene Isomers	58
2.1	Introduction.....	58
2.2	Computational details	61
2.3	Results and discussion	62
2.3.1	Bond lengths	62
2.3.2	Mayer bond orders	72
2.3.3	Electron Localization Function (ELF) π -orbitals.....	76
2.3.4	Nucleus-Independent Chemical Shift (NICS)	78
2.3.5	Electric dipole moment.....	79
2.3.6	Electrostatic Potential Map.....	81
2.3.7	Frontier molecular orbitals.....	83
2.3.8	Vertical Excitation.....	85
2.3.9	Adiabatic Excitation Energy	86
2.4	BN Doping Effects in PAHs	88
2.5	Conclusion	92
	Appendix.....	94
	Reference	116
Chapter 3	Computational Design of Donor- π -Acceptor Systems with BN-doped PAHs as Effective π -Bridges for Singlet Fission Applications.	119

3.1 Introduction.....	119
3.2 Computational details	121
3.3 Results and discussion	121
3.4 Conclusion	141
Reference	143

Chapter 1 BN-2,1-naphthalenes

1.1 Introduction: BN/CC Isosterism and BN-doped Polycyclic Aromatic Hydrocarbons (PAHs)

BN/CC isosterism arises from the fact that both boron-nitrogen unit and carbon-carbon unit have eight valence electron count in covalent systems.¹ For instance, replacing two carbon atoms with one boron atom and one nitrogen atom in benzene can lead to three BN isoelectronic family members involving 1,2-azaborine, 1,3-azaborine, and 1,4-azaborineⁱ (Figure 1.1). Despite the same electron count, these isoelectronic molecules differ in physical and chemical properties owing to distinct electronic structures.² These three isomers have been theoretically investigated in terms of their thermodynamic stability and aromaticity.³ Specifically, 1,2-azaborine has been determined to be the most thermodynamically stable, while 1,3-azaborine is the least thermodynamically stable. On the other hand, 1,3-azaborine exhibits the highest aromatic character, while 1,4-azaborine exhibits the lowest aromatic character.

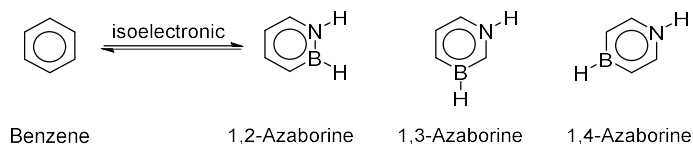


Figure 1.1. BN/CC isosterism in benzene/azaborine.

Driven by potential applications of BN/CC isosterism, the fundamental studies on azaborine chemistry are still being conducted since the pioneering work from Dewar in 1958.⁴ For monocyclic structures, the reported synthesis of azaborines illustrated in Figure 1.2 has received significant attention. Briefly, the first reported 1,2-azaborine derivative was synthesized by Dewar through the methods of electrophilic borylation and Raney nickel catalyzed reduction.⁵ White synthesized the first monosubstituted 1,2-azaborine derivative through the methods of hydroboration and dehydrogenation.⁶ Both

ⁱ Formally, these BN-heterocycles are named 1,2-, 1,3-, 1,4-dihydro-1,2, 1,3, 1,4-azaborine, respectively. As an abbreviation, and to follow the naming by Ashe, 1,2-azaborine, 1,3-azaborine, 1,4-azaborine, respectively, are used.

synthesis required relatively harsh conditions (e.g. high temperature). At the turn of the millennium, Ashe applied ring-closing olefin metathesis to the synthesis of 1,2-azaborine, greatly increasing yields under milder conditions.⁷ Braunschweig provided the first example of 1,4-azaborine derivative. Liu advanced the development of all three azaborine isomers.⁸ Specifically, Liu isolated and characterized the first parental 1,2-azaborine, the intermediate *N*-TBS-*B*-Cl-1,2-azaborine played an important role in the late-stage studies as a synthon.⁹ In addition, Liu also reported the first 1,3-azaborine and provided a unique synthetic method of 1,4-azaborine.¹⁰

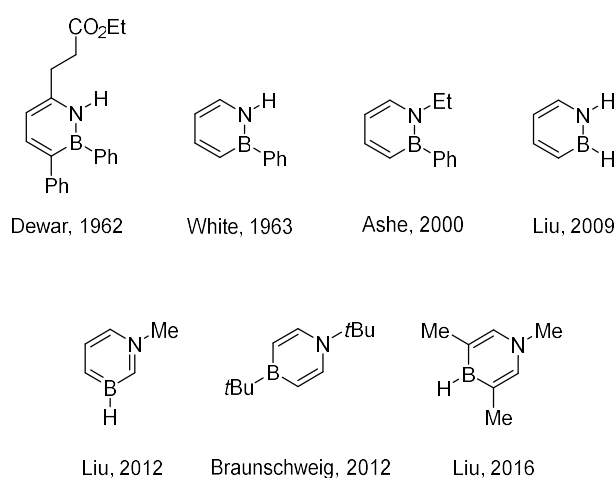


Figure 1.2. Representative monocyclic azaborines.

Research interest in monocyclic azaborines was mostly motivated by understanding its fundamental properties.¹¹ Among these three isosteres, 1,2-azaborine received the most attention due to its relative stability and readily synthetic access. A number of publications from Liu group indicated that 1,2-azaborine scaffold had potential applications in biomedical research.¹² Compared to limited applications of monocyclic azaborines in material chemistry, ring-fused azaborines, specifically BN-doped polycyclic aromatic hydrocarbons (PAHs), have numerous examples of potentially applicable materials. In the past decade, BN-doped PAHs have been discovered to have potential applications in many optoelectronic materials such as organic field-effect transistors (OFETs)¹³, organic light-emitting diodes (OLEDs)¹⁴ and single fission (SF) materials¹⁵. Pei demonstrated several compounds involving BN-doped heterosuperbenzenes, tetrathienonaphthalenes as well as its polymers, and

tetrabenzopentacene had potential application in OFETs with a hole mobility from 0.05 $\text{cm}^2\text{V}^{-1}\text{s}^{-1}$ to 0.35 $\text{cm}^2\text{V}^{-1}\text{s}^{-1}$ (Figure 1.3).¹⁶ Furthermore, Direct comparison between BN-doped perylene diimide (PDI) (0.06 $\text{cm}^2\text{V}^{-1}\text{s}^{-1}$) and its all-carbon analogue (0.004 $\text{cm}^2\text{V}^{-1}\text{s}^{-1}$) in OFET performance indicated improved charge transport properties by BN doping.¹⁷ Wang demonstrated BN-doped anthracene existed excellent OFET performance with a hole mobility of up to 1.35 $\text{cm}^2\text{V}^{-1}\text{s}^{-1}$, which is so far the highest record among all reported BN-doped PAHs.¹⁸

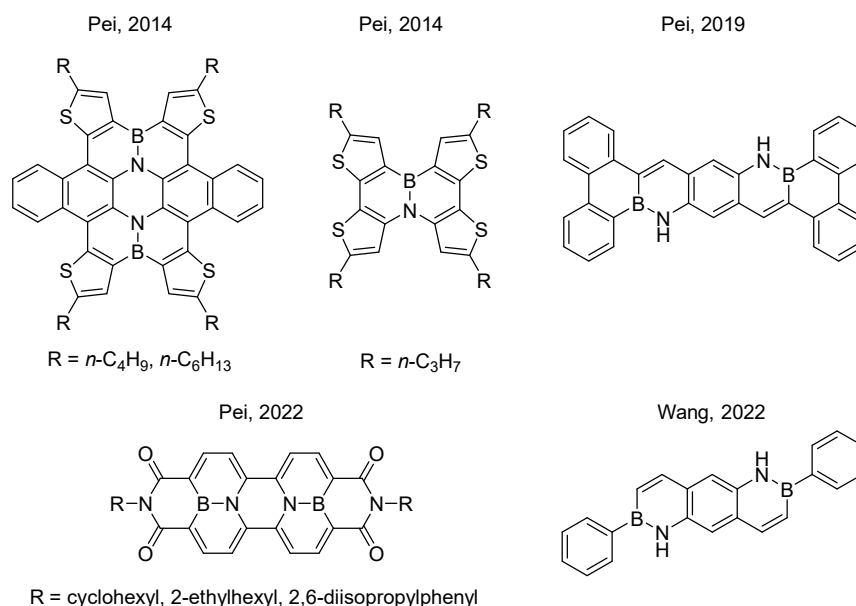


Figure 1.3. Selected examples of BN-doped PAHs in application of OFETs.

Many BN-doped PAHs displayed strong emission, which makes them appropriate for application in OLED devices (Figure 1.4). Perepichka synthesized a deep-blue emissive BN-doped thiophene through a classic electrophilic borylation reaction.¹⁹ Feng developed a ladder-type BN-doped heteroacenes which exhibited blue luminescence with emission of 418 nm. Assembled emitters in OLEDs from this molecule exhibited external quantum efficiency (EQE) of 1.4%.²⁰ The BN-doped coronene, synthesized independently by Pei and Zhang, showed potential of being a blue emitter in OLEDs.²¹ Besides fluorescent emitters, Hatakeyama demonstrated a phosphorescent emitter in OLEDs using BN-doped tetrabenzonaphthalene as a host material.²² Furthermore, varied light emitters had also been explored, such as BN-doped

PDI reported by Zhang.²³

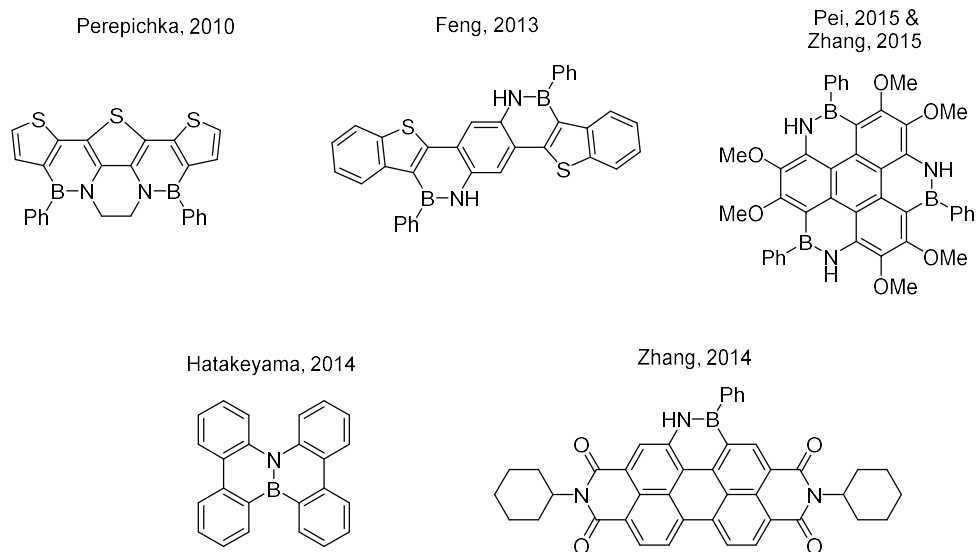


Figure 1.4. Selected examples of BN-doped PAHs in application of OLEDs.

In recent years, the multiple resonance-induced thermally activated delayed fluorescence (MR-TADF) emitter for OLEDs have attracted extreme attention due to the remarkable performances performing light purity and external quantum efficiency.²⁴ Most of MR-TADF molecules were designed using the 1,4-azaborine motif fused in PAHs (Figure 1.5). The first example of MR-TADF molecule was developed by Hatakeyama in 2016, with blue emission located at 467 nm and a full width at half maximum (FWHM) of 28 nm and a high external quantum efficiency (EQE_{max}) upwards of 20%.²⁵ Then, an advanced emitter was reported in 2019, with blue emission located at 469 nm and a FWHM of 18 nm and a EQE_{max} of 34.4%.²⁶ Duan reported a pure green emitter, which emission located at 493 nm with a FWHM of 31.6 nm and a EQE_{max} of 20.9%.²⁷ Li reported a pure red emitter, with emission located at 618 nm and a FWHM of 47 nm, and a EQE_{max} of 20.1%.²⁸

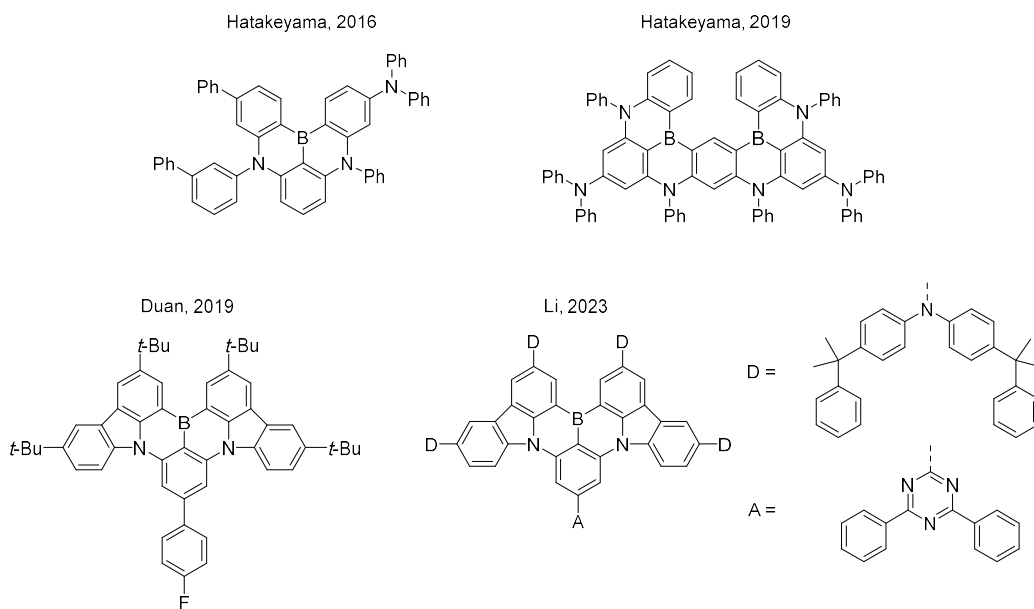


Figure 1.5. Selected examples of BN-doped PAHs as MR-TADF emitters.

Furthermore, theoretical and experimental studies demonstrated potential application of BN-doped PAHs in singlet fission (SF), a concept that has the potential to enhance solar energy conversion efficiency.²⁹ To the best of our knowledge, only one candidate of BN-doped PAHs had been experimentally demonstrated to exhibit SF properties, leaving synthetic room for further development.³⁰

Despite the promising applications of BN doped PAHs, the synthetic access for these compounds has been limiting the progress. Many synthetic methods to prepare 1,2-azaborine-fused PAHs have been developed over the past decades. Herein, we will review the typical methods or strategies of 1,2-azaborine-fused PAHs which could provide inspirations for synthesis of unknown BN-doped PAHs. Beginning with the simplest structure of PAHs, naphthalene, CC/BN replacement in a naphthalene can generate six BN-naphthalene analogues (Figure 1.6). Among these seemingly simple structures of BN-naphthalene, two parental isomers remain unreported. The synthesis of these most basic structures requires fundamentally new approaches, and some synthetic methods can be applied to other larger systems. As a result, coming up with new strategies to synthesize these basic analogs contributes significantly to BN chemistry.

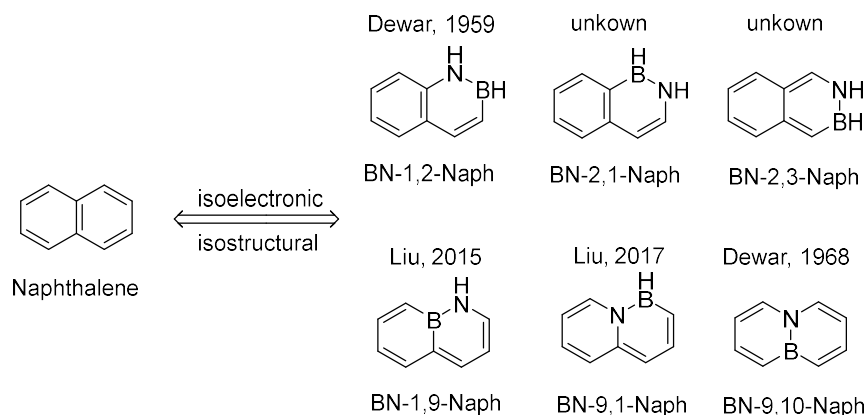
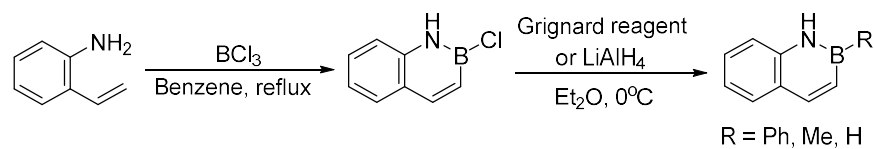


Figure 1.6. Naphthalene and BN-doped naphthalene isosteres.

Following the pioneering work on the synthesis of the BN-9,10-phenanthrene in 1958⁴, Dewar established the synthesis of BN-1,2-naphthalene in the following year (Scheme 1.1).³¹ Starting with 2-vinylaniline and boron trichloride reagents, the synthesis produced *B*-Cl-BN-1,2-naphthalene intermediate, which was subsequently processed with the Grignard reagent or lithium aluminum hydride to create substituted BN-1,2-naphthalenes or the parental structure.

Scheme 1.1. Dewar's Synthetic Strategy



This borylative cyclization approach by Dewar is one of the most popular strategies in constructing BN containing aromatic compounds based on using vinyl arylamine precursors (Figure 1.7). A large number of BN containing molecules has been synthesized via this method with high yields.³² The 2-vinylaniline core structure is necessary in the precursors for the formation of BN compounds.

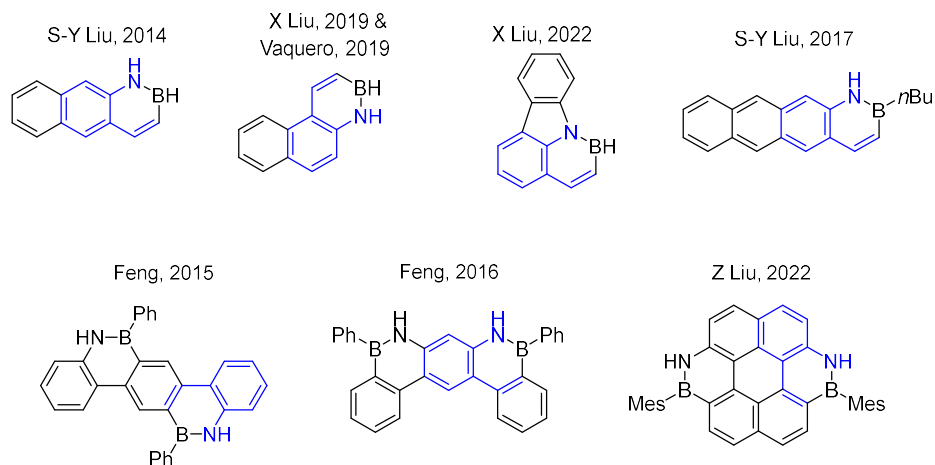
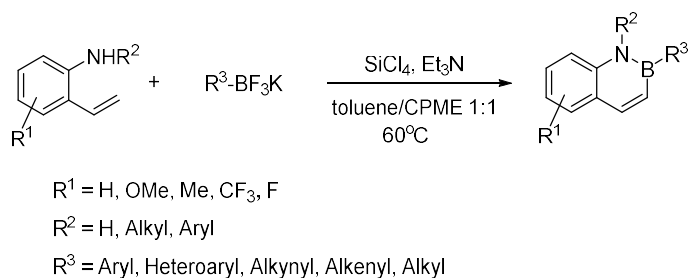


Figure 1.7. Selected examples of BN-doped PAHs synthesized by Dewar's borylation.

Molander demonstrated an approach to generate BN-1,2-naphthalene derivatives using organotrifluoroborates as a convenient boron source (Scheme 1.2).³³ To avoid using high activated trihaloboranes, potassium organotrifluoroborates alternatives can be in-situ converted to organodihaloboranes under activation with silicon tetrachloride. In his work, plenty of highly functionalized BN-1,2-naphthalene derivatives were produced under the mild reaction conditions with high yields.

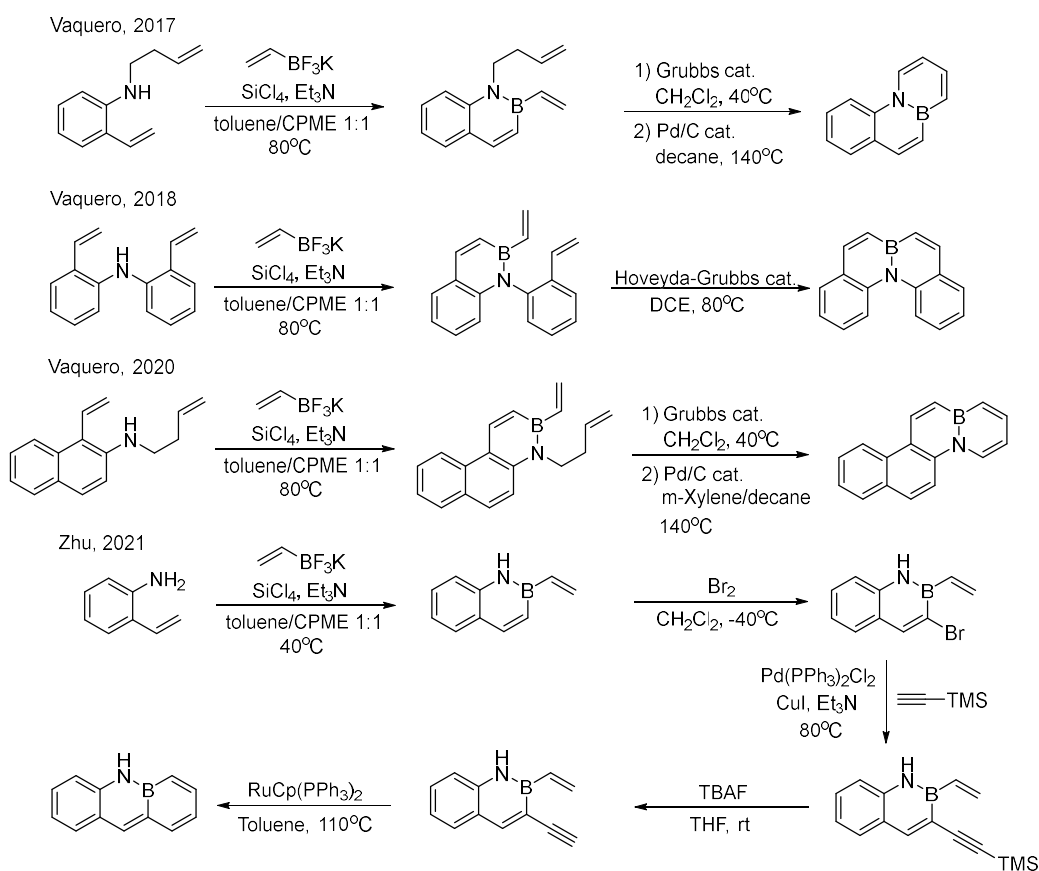
Scheme 1.2. Molander's Synthetic Strategy



Molander's borylation strategy was successfully applied by other chemists for the synthesis of BN containing compounds (Scheme 1.3). Specifically, Vaquero³⁴ and Zhu³⁵ employed the methods of Molander borylation and ring-closing metathesis in the synthesis of inner BN-doped phenanthrene, benzo[c]phenanthrene, chrysene and anthracene analogues.

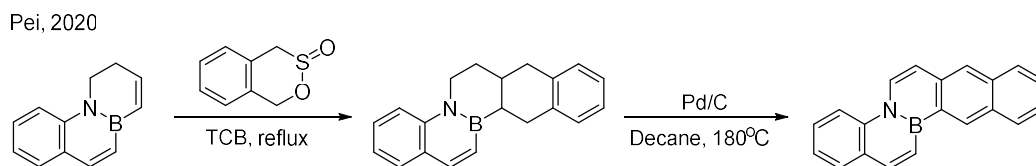
Scheme 1.3. Selected Examples of BN-doped PAHs Synthesized by Molander's

Borylation



Following this strategy, Pei offered an example that the unaromatized BN heterocycle could be extended to a larger size by Diels-Alder reaction (Scheme 1.4).³⁶ Specifically, this Diels-Alder reaction occurred between the boron-linked dienophile and the in-situ generated *o*-xylylene, then the fold-line-shaped BN-doped PAHs were formed by the dehydrogenation process.

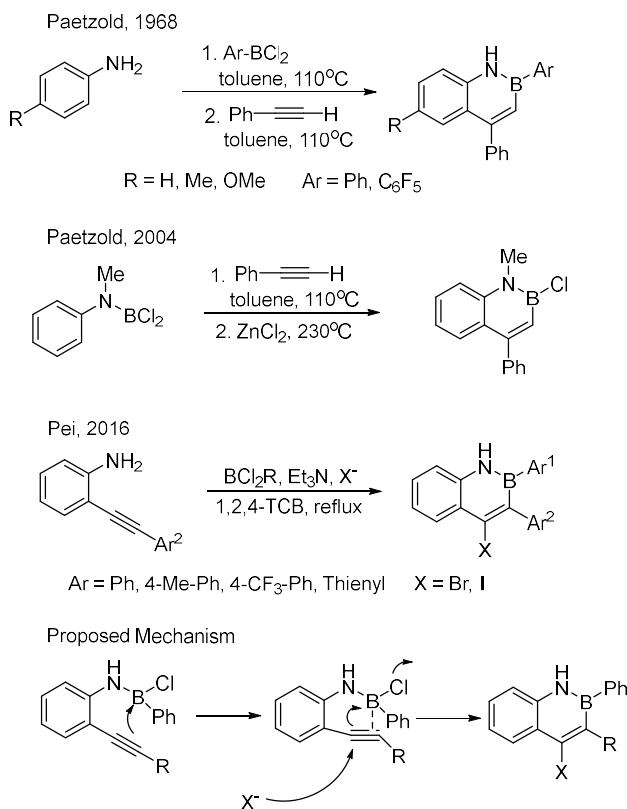
Scheme 1.4. BN Heterocycle Extended by Diels-Alder Reaction



Paetzold demonstrated the three-component reaction of aniline,

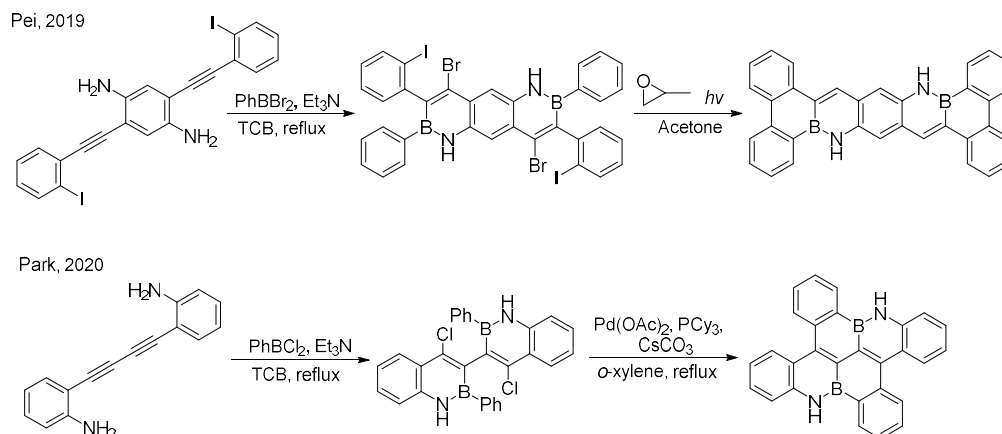
dichlorophenylborane and phenylacetylene for the synthesis of BN-1,2-naphthalene derivatives (Scheme 1.5).³⁷ Unlike Dewar's synthetic method, Paetzold's method has the advantage of straightforward synthesis of multiple substituted BN-1,2-naphthalene without late-stage functionalization. As an example, Pei developed the synthesis of tri-substituted BN-1,2-naphthalene from 2-alkynyl aniline. Most importantly, halogenation on C4 position made it possible for the further functionalization, because this non-electron-rich C4 position could be difficult to halogenate directly by nucleophilic aromatic substitution.³⁸

Scheme 1.5. Alkynyl Participant BN Heterocycle Formation



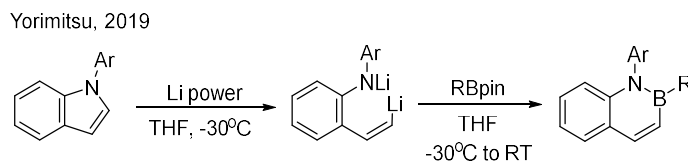
The potential of this strategy was identified by Pei in the synthesis of BN-embedded tetrabenzopentacene which could be applicable in electronic devices (Scheme 1.6).^{16d} Additionally, Pei's approach was adopted by Park in a convenient synthesis of B₂N₂-ixene in 2020.³⁹ The BN-1,2-naphthalene dimer was generated from the starting alkynyl aniline dimer via double borylative cyclization followed by intramolecular cross coupling.

Scheme 1.6. Facile Synthesis of BN-doped PAHs by Pei's Method



Yorimitsu developed a unique ring-opening and ring-closing strategy in the synthesis of BN-1,2-naphthalene structures using *N*-aryl indole as starting materials in 2019 (Scheme 1.7).⁴⁰ In this synthesis, the reductive cleavage via metal lithium allowed the insertion of boron into the C2-N σ bond of indole.

Scheme 1.7. Yorimitsu's Synthetic Strategy

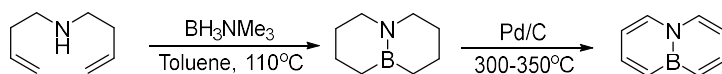


R = aryl, alkyl, Alkenyl, Alkynyl, Heterocycle

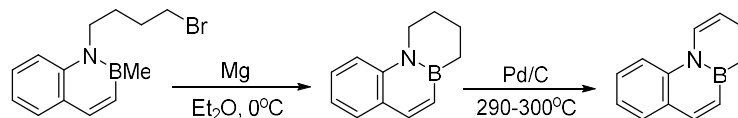
The initial synthesis of BN-9,10-naphthalene was reported by Dewar using a hydroboration-oxidation strategy in 1968 (Scheme 1.8).⁴¹ The BN bicycle was created by treating the di-3-butenylamine with trimethylamine-borane. BN-9,10-naphthalene was obtained by palladium/carbon-catalyzed dehydrogenation at $>300^{\circ}\text{C}$. In addition, Dewar also described the new expansion of BN-bicycles from an in-situ produced Grignard reagent as a method for the synthesis of inner BN-embedded compounds.⁴²

Scheme 1.8. Dewar's Synthetic Strategy

Dewar, 1968



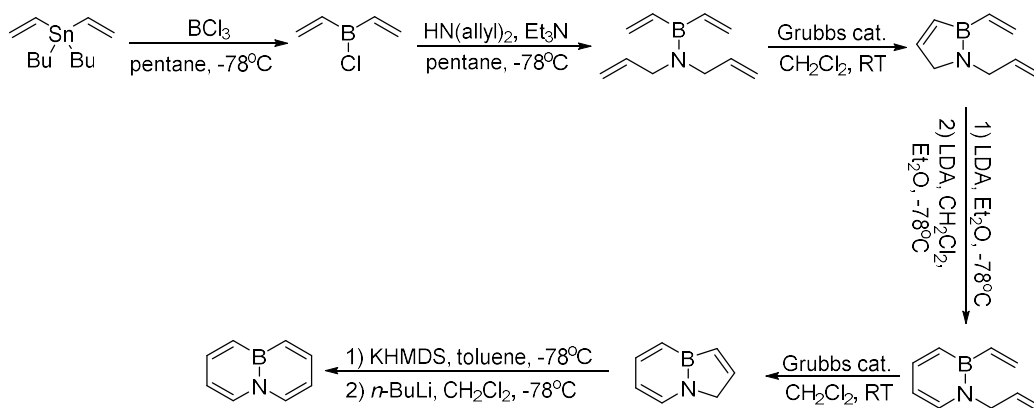
Dewar, 1962



Ashe and co-workers developed a novel strategy for the synthesis of BN-9,10-naphthalene using ring-closing metathesis in 2006 (Scheme 1.9).⁴³ Specifically, the synthesis involves two ring-closing metathesis processes and two ring-expansion processes.

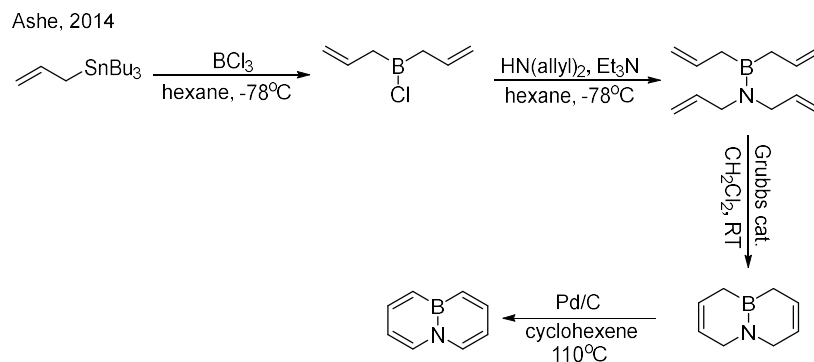
Scheme 1.9. Ashe's Synthetic Strategy

Ashe, 2006



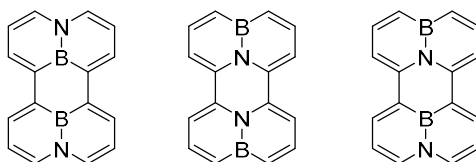
Ashe subsequently improved the synthesis of BN-9,10-naphthalene through a short synthetic route by using diallyl boron chloride instead of divinyl boron chloride to form the BN adduct (Scheme 1.10).⁴⁴ The BN bicyclohexene was generated from the subsequent ring-closing metathesis. Both BN-9,10-naphthalene and partial hydrogenated azaborine side product were observed from the Pd/C -catalyzed dehydrogenation process. Apparently, the BN bicyclohexene can be dehydrogenated at milder condition and higher yield comparing with the BN bicyclohexane. Fang found that DDQ was also a suitable oxidized reagent in the dehydrogenation step.⁴⁵

Scheme 1.10. Ashe's Synthetic Strategy

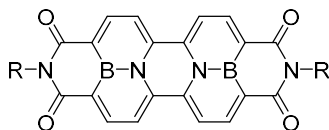


Based on this important BN-9,10-naphthalene synthon, Pei developed facile synthetic strategies of various parental B_2N_2 -perylene structures and B_2N_2 -PDI analogue in last few years (Figure 1.8).^{46,17}

Pei, 2021



Pei, 2022

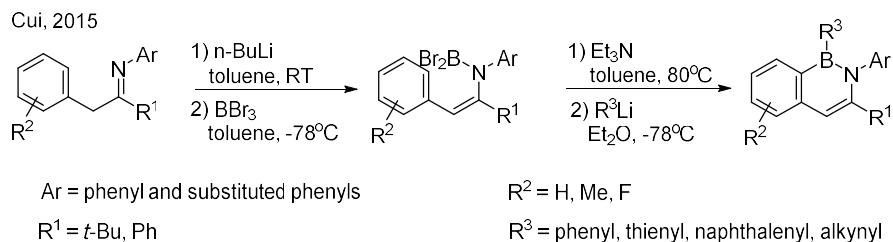


R = cyclohexyl, 2-ethylhexyl, 2,6-diisopropylphenyl

Figure 1.8. BN-doped PAHs synthesized by late-stage functionalization of BN-9,10-naphthalene.

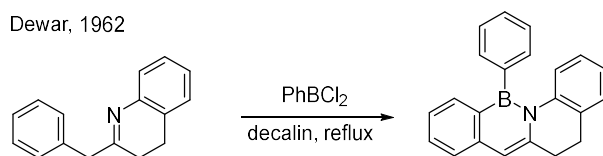
The first BN-2,1-naphthalene derivative was reported by Cui in 2015 (Scheme 1.11).⁴⁷ Benzyl imine derivatives were employed as starting materials which upon treatment with *n*-butyl lithium generated the conjugated enamine intermediates. To prevent competition with the *n*-BuLi nucleophilic addition process, secondary ketimines need to be employed. The enamine intermediates could readily produce cyclized BN adducts when treated with boron tribromide.

Scheme 1.11. Cui's Synthetic Strategy



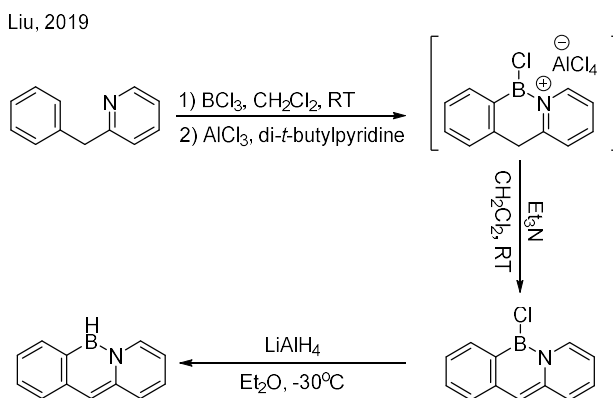
The imine-directed borylation process can be traced to the work of Dewar in the synthesis of a BN heterocyclic compound as early as 1962 (Scheme 1.12).⁴⁸ The high temperature required in Dewar's work indicated that the formation of aromatized BN heterocycle was inhibited without the deprotonation by *n*-BuLi.

Scheme 1.12. Dewar's Synthetic Strategy



Similar to the benzyl imine precursor, Liu developed a simple one-pot synthesis of BN-9a,9-anthracene starting from 2-benzyl pyridine (Scheme 1.13).⁴⁹ With the optimization of the reaction conditions, a strong Lewis acid such as aluminum trichloride was determined to the intramolecular electrophilic borylation under mild conditions. The aromatization process was achieved by deprotonation with triethylamine.

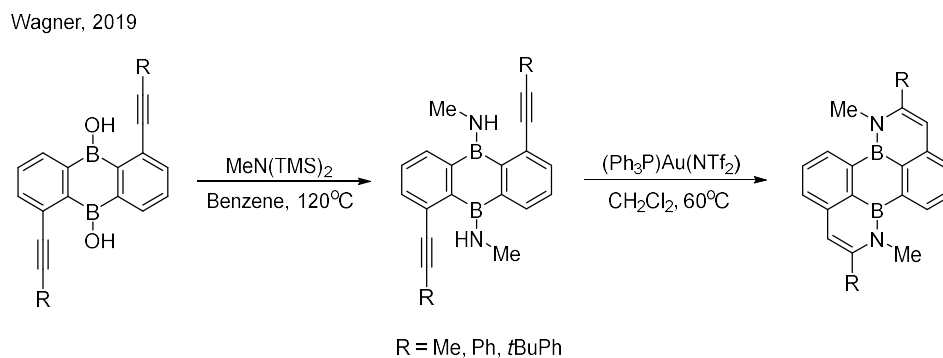
Scheme 1.13. Liu's Synthetic Strategy



A novel synthetic strategy of Au-catalyzed amino-alkynyl addition was developed

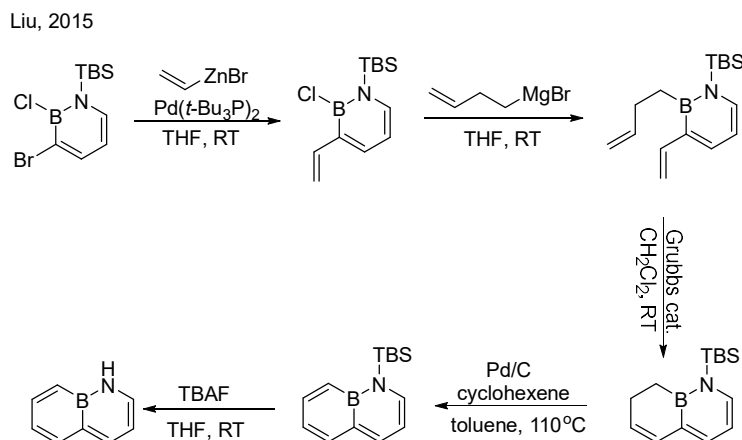
by Wagner for the synthesis of B₂N₂-perylene analogues (Scheme 1.14).⁵⁰ Unlike the classical borylative cyclization, the BN heterocycle of the B₂N₂-perylene was ring-closed by inserting a nitrogen atom.

Scheme 1.13. Wagner's Synthetic Strategy



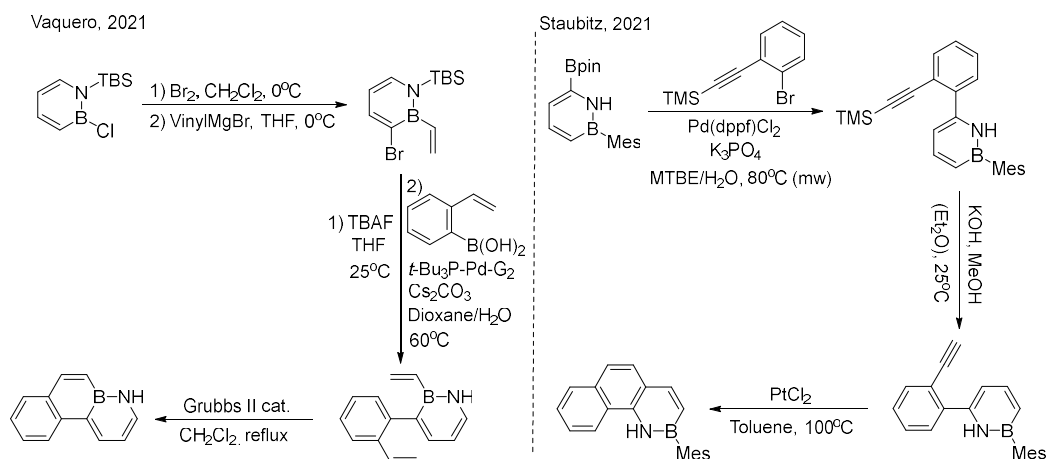
Liu demonstrated the synthesis of the parental BN-1,9-naphthalene in 2015 (Scheme 1.15).⁵¹ The discovery that the Negishi cross-coupling reaction was compatible with a reactive B-Cl bond enabled the feasible synthesis of the 3-vinyl-*N*-TBS-*B*-Cl-azaborine precursor. The boron position was functionalized by allyl Grignard reagent, and subsequent ring-closing metathesis produced the bicyclic intermediate. The *N*-TBS-BN-1,9-naphthalene was generated via the dehydrogenation of palladium carbon. In the end, the removal of the *N*-TBS protection group with tetrabutylammonium fluoride (TBAF) resulted in the formation of the parental compound.

Scheme 1.15. Liu's Synthetic Strategy



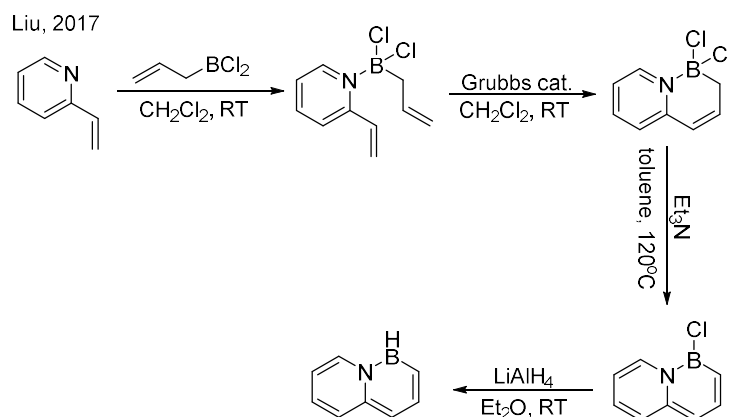
The strategy of “late-stage” functionalization from the *N*-TBS-*B*-Cl-1,2-azaborine precursor was successfully applied to the synthesis of the parental BN-1,10a-phenanthrene by Vaquero.⁵² In addition, Staubitz demonstrated the synthesis of BN-4,3-phenanthrene starting from the 6-Bpin-*B*-Mes-1,2-azaborine building block, followed by Suzuki-Miyaura cross-coupling, deprotection and electrophilic ring-closing three steps. (Scheme 1.16).⁵³

Scheme 1.16. BN-doped PAHs Synthesized from Azaborine Synthons



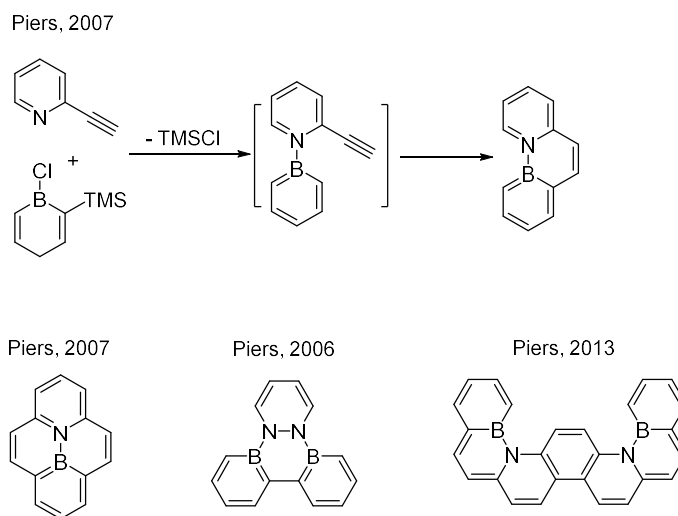
Another parental BN-naphthalene isostere was reported by Liu using a straightforward four-step synthesis in 2017 (Scheme 1.17).⁵⁴ The synthesis of BN-9,1-naphthalene started from treatment of 2-vinylpyridine with the in situ generated allylboron dichloride to form the BN adduct. The bicyclic BN intermediate was subsequently generated from ring-closing metathesis without any purification. The intramolecular dehydrochlorination process was promoted by triethylamine and reflux to obtain aromatic *B*-Cl-BN-9,1-naphthalene. The parent BN-9,1-naphthalene was produced after further treatment with lithium aluminum hydride.

Scheme 1.17. Liu's Synthetic Strategy



In addition to the naphthalene motif, several unique synthetic methods of more conjugated BN-doped PAHs have also been reported. Piers developed a novel strategy for the synthesis of BN-4a,4b-phenanthrene by using combination of two independent nitrogen heterocycle and boron heterocycle fragments in 2007 (Scheme 1.18).⁵⁵ BN-4a,4b-phenanthrene was obtained from 2-ethynyl pyridine and the in-situ generated 1-chloro-2-trimethylsilyl-boracyclohexa-2,5-diene in one step. This method was successfully applied in a number of BN conjugated systems by Piers.⁵⁶

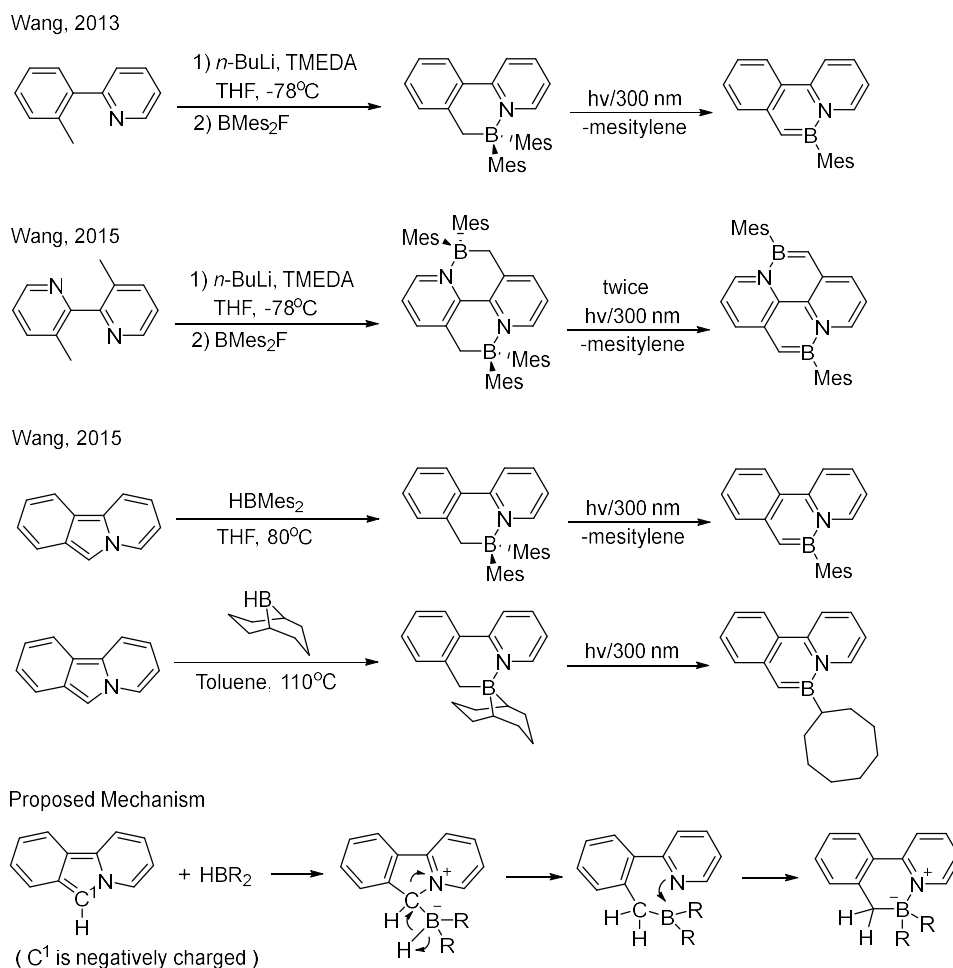
Scheme 1.18. Piers's Synthetic Strategy



Wang established a novel photoelimination reaction of BN-heterocyclic compounds resulting in the synthesis of BN phenanthrene and BN pyrene derivatives (Scheme 1.19).⁵⁷ The mesityl substituted BN-8a,9-phenanthrene and B₂N₂-pyrene were

synthesized by three processes involving lithiation, borylation and photoelimination. Furthermore, a unique 1,1-hydroboration reaction allowing boryl insertion into a C-N bond to generate same type of BN phenanthrene derivatives was reported.⁵⁸

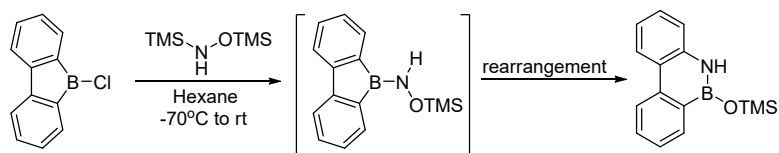
Scheme 1.19. Wang's Synthetic Strategy



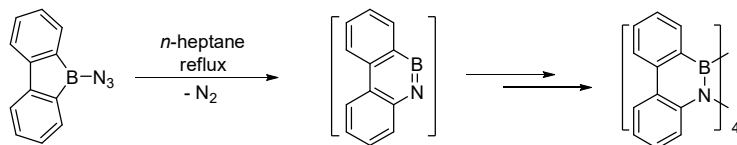
Bettinger demonstrated a strategy for BN-9,10-phenanthrene formation from borafluorene and silylated hydroxyl amine via a spontaneous ring expansion (Scheme 1.20).⁵⁹ Furthermore, the same group discovered BN-9,10-phenanthryne using a ring expansion reaction of *B*-azidodibenzoborole, which cyclotetramerized in-situ to create a severely deformed BN-9,10-phenanthrene tetramer.⁶⁰ Braunschweig showed that heavily substituted 1,2-azaborine could be formed via insertion of an azide into a B-C bond of borole.⁶¹ Martin employed this strategy for the synthesis of BN-9,10-phenanthrene derivatives which permitted preservation of the facilely substitutable boron center.⁶²

Scheme 1.20. The Synthesis of BN-doped PAHs through Ring Expansion

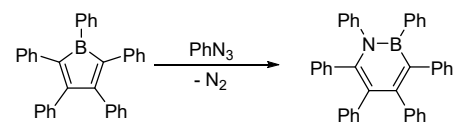
Bettinger, 2012



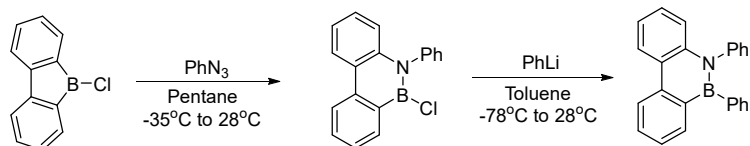
Bettinger, 2014



Braunschweig, 2014



Martin, 2018

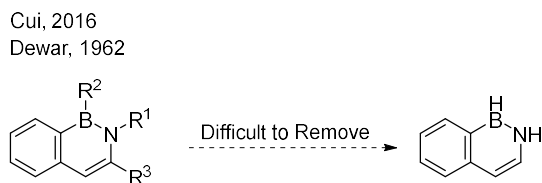


The chemistry of BN-2,1-naphthalene, family of compounds remains underdeveloped to date. To fill this gap, this chapter will focus on the synthesis and characterization of parental BN-2,1-naphthalene and its derivatives.

1.2 BN-2,1-naphthalene: Synthesis and Characterization

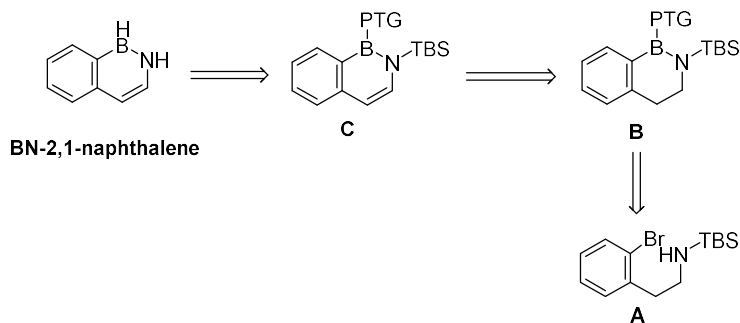
As mentioned before, both Cui⁴⁷ and Dewar⁴⁸ have put efforts into the synthesis of highly substituted BN-2,1-naphthalene derivatives. For Cui's method, secondary ketimines need to be employed as the starting materials in the synthesis of the BN-2,1-naphthalene isomer to suppress side reaction as a result of the alkyllithium nucleophilic addition to imine. Thus, it is particularly challenging to synthesize the parental BN-2,1-naphthalene (or even a monosubstituted BN-2,1-naphthalene) by removing the extra substituents R¹, R², R³ in Scheme 1.21. To the best of our knowledge, none of the reported methods can be directly applied in the synthesis of the parental BN-2,1-naphthalene.

Scheme 1.21. Synthetic Strategies of Parental BN-2,1-naphthalene



Scheme 1.22 shows a retrosynthetic analysis for accessing the parental BN-2,1-naphthalene. We envisioned that the target compound can be obtained from a suitably protected compound **C** which can in turn be synthesized from the TBS-protected amino aryl bromide **A** via a boron inserted intermediate **B**. The key to successfully implement this strategy is identifying a suitable boron protecting group and developing a deprotection strategy. We ultimately identified the Ph group to be a suitable boron protecting group, and we have developed a Ir-catalyzed boron deprotection method as part of our synthesis.ⁱⁱ

Scheme 1.22. Retrosynthetic Analysis of Parental BN-2,1-naphthalene



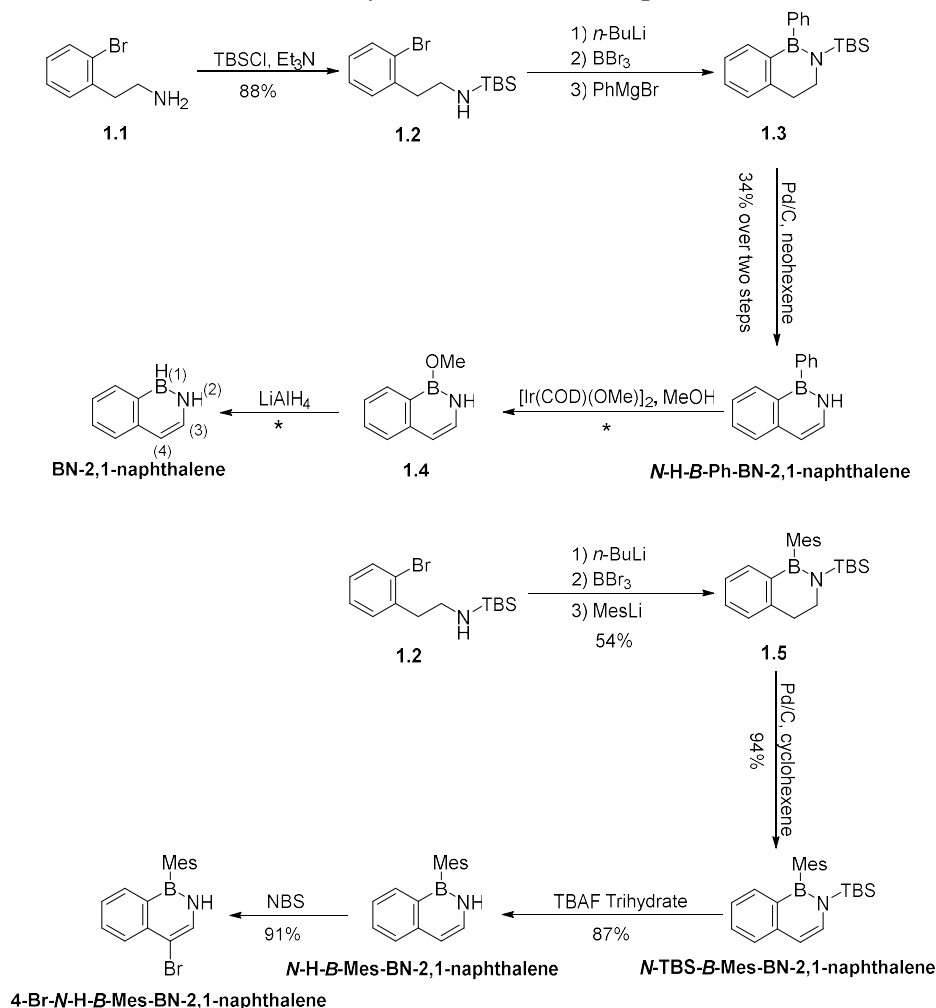
1.2.1 Synthesis of BN-2,1-naphthalene

As can be seen from Scheme 1.23, the synthesis of BN-2,1-naphthalene begins with the commercially available amine **1.1**, which upon *N*-protection with TBSCl affords precursor **1.2**. The resulting protected amine **1.2** was treated with two equivalents of *n*-butyl lithium to generate a strong organobislithium nucleophile, which upon quenching with BBr₃ and PhMgBr generates the key BN cyclization intermediate

ⁱⁱ Unpublished results by Mr. Jiangpeng Liu.

1.3. This intermediate undergoes Pd/C-catalyzed dehydrogenation and deprotection to give the aromatized *B*-Ph-BN-2,1-naphthalene. The phenyl group on boron undergoes an iridium-catalyzed sigma bond metathesis with MeOH to give compound **1.4**. The *B*-OMe species was reduced by lithium aluminum hydride to finish the parental BN-2,1-naphthalene. Additionally, the air-stable *N*-H-*B*-Mes-BN-2,1-naphthalene and *N*-TBS-*B*-Mes-BN-2,1-naphthalene were synthesized by a similar synthetic route via the intermediate **1.5**. Furthermore, treatment of *N*-H-*B*-Mes-BN-2,1-naphthalene with *N*-bromosuccinimide (NBS) selectively installs the Br functional group at the C(4) position.

Scheme 1.23. Synthesis of BN-2,1-naphthalene



* The parental compound BN-2,1-naphthalene and intermediate **1.4** were not isolated but observed from ^1H and ^{11}B NMR.

1.2.2 Optoelectronic Properties of BN-2,1-naphthalenes

N-TBS-*B*-Mes-BN-2,1-naphthalene and *N*-H-*B*-Mes-BN-2,1-naphthalene were subjected to UV-photoelectron spectroscopy (UV-PES). The UV-PES is the experimental technique for determining the energies of occupied molecular orbitals owing to the accurate measurement of ionization energies.⁶³ For the rational interpretation of spectra, a combined UV-PES / theoretical approach is necessary, which was developed by Chrostowska and coworkers to investigate the electronic structures.⁶⁴ In the past decade, the Liu group has investigated several BN-heterocycles with UV-PES.^{65,2,32a,54}

The UV-photoelectron spectra of *N*-H-*B*-Mes-BN-2,1-naphthalene and *N*-TBS-*B*-Mes-BN-2,1-naphthalene are illustrated in Figure 1.9. For the reliable assignment of PE bands, DFT (Δ SCF/TD-DFT (CAM-B3LYP)) calculations of IEs using the 6-311G(d,p) basis set have been carried out on optimized geometrical parameters of these two compounds. Theoretically (x_{th}) and experimentally (x_{exp}) “corrected” Koopman ionization energies with the MOs visualization of the two compounds in comparison with experimental results are given in Table 1.2 and Table 1.3. Table 1.2 shows that the first ionization of *N*-H-*B*-Mes-BN-2,1-naphthalene occurs at 7.8 eV and corresponds to ejection of an electron from the HOMO. The second, third, fourth, fifth and sixth ionizations occur at 8.2, 8.4, 8.9, 9.8 and 10.3 eV and correspond to HOMO–1, HOMO–2, HOMO–3, HOMO–4 and HOMO–5, respectively. *N*-TBS-*B*-Mes-BN-2,1-naphthalene has a very similar PE spectrum with *N*-H-*B*-Mes-BN-2,1-naphthalene. The first PE band of *N*-TBS-*B*-Mes-BN-2,1-naphthalene is located at 7.6 eV (shifted by 0.2 eV) and followed by 8.1, 8.3, 8.8, 9.4 and 9.6 eV, which are slightly lower than each IE of *N*-H-*B*-Mes-BN-2,1-naphthalene. Both theoretically and experimentally “corrected” Koopman ionization energies are consistent with the experimental results. The Δ SCF/TD-DFT predicted ionization energies are very close to PE values, which can be potentially applied to other unknown compounds. The results are consistent with the *N*-TBS group exerting a donating effect, raising the HOMO of *N*-TBS-*B*-Mes-BN-2,1-naphthalene relative to *N*-H-*B*-Mes-BN-2,1-naphthalene.

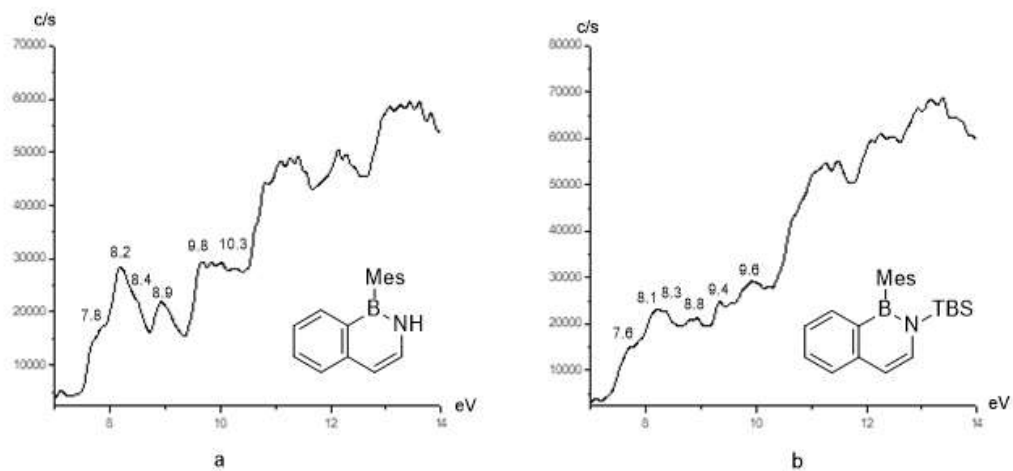


Figure 1.9. UV-photoelectron spectra of a) *N*-H-*B*-Mes-BN-2,1-naphthalene, b) *N*-TBS-*B*-Mes-BN-2,1-naphthalene.

Table 1.2 Calculated Kohn-Sham energies of MO ($-\varepsilon^{\text{K-S}}$), $\Delta\text{SCF/TD-DFT}$ (CAM-B3LYP/6-311G(d,p)), and theoretically (x_{th}) and experimentally (x_{exp}) “corrected” Koopman ionization energies with the MOs visualization of *N-H-B-Mes-BN-2,1-naphthalene* in comparison with experimental results (in eV).

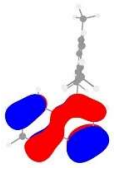
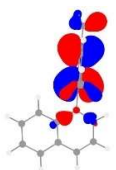
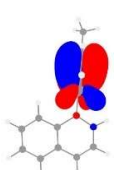

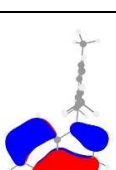
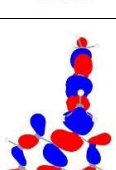
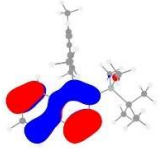
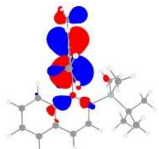
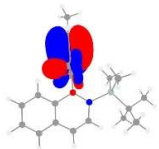
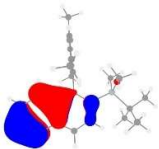
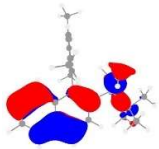
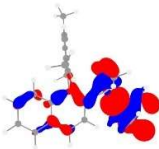
MO	$-\varepsilon^{\text{K-S}}$	$\Delta\text{SCF/TD-DFT}$	Koopman corrected $x_{\text{th}} = 0.50$	Koopman corrected $x_{\text{exp}} = 0.63$	Exp.
	7.17	7.67	7.67	7.80	7.8
	7.61	8.07	8.11	8.24	8.2
	7.76	8.28	8.26	8.39	8.4
	8.37	9.15	8.87	9.00	8.9
	9.19	9.81	9.69	9.82	9.8
	9.73	10.13	10.23	10.36	10.3

Table 1.3 Calculated Kohn-Sham energies of MO ($-\varepsilon^{\text{K-S}}$), $\Delta\text{SCF/TD-DFT}$ (CAM-B3LYP/6-311G(d,p)), and theoretically (x_{th}) and experimentally (x_{exp}) “corrected” Koopman ionization energies with the MOs visualization of *N-TBS-B-Mes-BN-2,1-naphthalene* in comparison with experimental results (in eV).

MO	$-\varepsilon^{\text{K-S}}$	$\Delta\text{SCF/TD-DFT}$	Koopman corrected $x_{\text{th}} = 0.36$	Koopman corrected $x_{\text{exp}} = 0.57$	Exp.
	7.03	7.39	7.39	7.60	7.6
	7.62	8.10	7.98	8.19	8.1
	7.77	8.35	8.13	8.34	8.3
	8.29	8.78	8.65	8.86	8.8
	8.99	9.27	9.35	9.56	9.4
	9.11	9.49	9.47	9.68	9.6

The photophysical properties of BN-2,1-naphthalenes were investigated by UV-Vis absorption spectra and compared with all-carbon naphthalene as well as other reported BN naphthalene isomers (Figure 1.10). The λ_{onset} of each absorption spectrum may indicate the excitation energy from ground state to the first singlet excited state. From our calculation (Table 1.4), the optical gaps of naphthalene and BN analogues are consistent with the experimentally observed λ_{onset} wavelengths. Specifically, high energy of optical gap is corresponding to low wavelength of λ_{onset} . In addition, *N-H-B-Ph-BN-2,1-naphthalene* and *N-H-B-Mes-BN-2,1-naphthalene* have similar absorption spectra, whereas the emission spectra have a slight shift because phenyl is more conjugated to BN-2,1-naphthalene plane than mesityl. The quantum yield of *N-H-B-Ph-BN-2,1-naphthalene* and *N-H-B-Mes-BN-2,1-naphthalene* are 0.27 and 0.22, respectively, which are determined by the reference of perylene.⁶⁶ With an observed λ_{abs} of 323 nm, *N-H-B-Ph-BN-2,1-naphthalene* exhibits a very similar lowest-energy absorption band to its orientational isomer *N-H-B-H-BN-1,2-naphthalene* (317 nm).^{67,46}

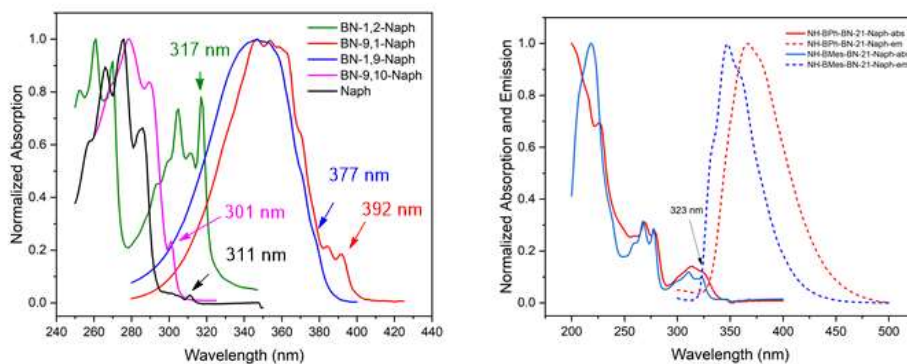


Figure 1.10. Normalized absorption spectra of naphthalene, BN-1,2-naphthalene, BN-1,9-naphthalene, BN-9,1-naphthalene and BN-9,10-naphthalene in cyclohexane. Comparison of normalized absorption and emission spectra of *N-H-B-Ph-BN-2,1-naphthalene* and *N-H-B-Mes-BN-2,1-naphthalene*.

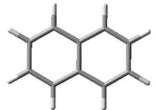
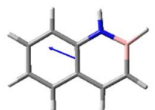
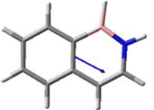
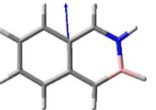
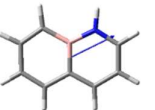
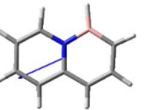
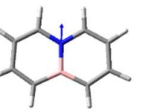
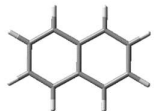
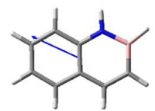
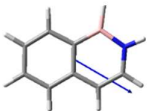

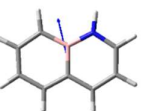

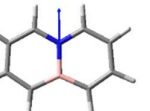
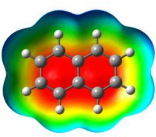
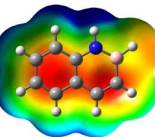
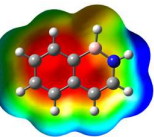
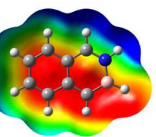
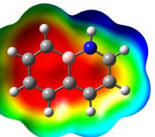
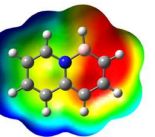
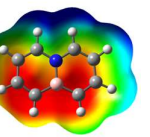
Coupled UV-Photoelectron Spectroscopy – Mass Spectrometry Measurements.

The UV-PES spectra were recorded on a home-built (IPREM/ECP), three-part spectrometer equipped with a main body device, He-I radiation source (21.21 eV and/or 48 eV) and a 127° cylindrical analyzer. The spectrometer works at constant analyzer energy under 5×10^{-6} hPa working pressure and $\leq 10^{-7}$ hPa for channeltron (X914L) pressure. The monitoring is done by a microcomputer supplemented by a digital–analogue converter (AEI spectrum). The spectra resulting from a single scan are built from 2048 points and are accurate within 0.05 eV. Spectra are calibrated with lines of xenon (12.13 and 13.44 eV) and of argon (15.76 and 15.94 eV). The accuracy of the ionization energies is ± 0.03 eV for sharp peaks and ± 0.05 eV for broad and overlapping signals. Mass spectra were recorded on a modified quadrupole mass spectrometer (PFEIFFER Prisma QMS200) with an electron-impact at 50 eV (mass range: 200 amu; detection limit: $\leq 10^{-14}$ hPa; working pressure: 2×10^{-7} hPa; operating temperature: 200 °C; electronic amplifier in working conditions: 10^{-10} A, QUAD STAR422 software for recording and treatment of MS data). The samples were slowly vaporized under low pressure (10^{-6} Torr) inside a handmade three-valve injector (3/4 inch diameter; 10 cm length; working temperature: $-190 \text{ °C} \leq T \leq +300 \text{ °C}$), and the gaseous flow was then continuously and simultaneously analyzed by both UV-photoelectron and mass spectrometers.

Computational Methods.

All calculations were performed using the Gaussian 09 (D.01)⁶⁸ program package. The geometries were initially optimized with tight convergence restrictions at the density functional theory (DFT) level with the hybrid CAM-B3LYP functional and 6-311G(d,p) basis set. All positive vibrational frequencies were checked to ensure that the structures were minima. The optimized geometries were used as starting points for all other calculations. Extra diffuse functions (6-311++G(d,p)) are included in the basis set to improve the description of the electron affinities (EA). The predicted UV-Vis spectra were calculated in the gas phase at TD-CAM-B3LYP/6-311++G(d,p) level. Ionization energies ($IE = E_{\text{cation}} - E_{\text{neutral}}$) were calculated with Δ SCF/TD-DFT combined method at CAM-B3LYP/6-311G(d,p) level.

Table 1.4. CAM-B3LYP/6-311G(d,p) Ground and First Excited-State Dipole Moment (Debye), Electrostatic Potential Map at the 0.001 Electron au Density Isocontour Level (from +12.55 to -12.55 kcal/mol), Δ SCF IE (eV), Kohn–Sham Energies (eV) of HOMO, LUMO, and HOMO–LUMO (H-L) Gap (eV), a CAM-B3LYP/6-311++G(d,p) electron affinity (eV), Δ (IE-EA) and optical gap (eV) for naphthalene and six BN analogues.

	Naphtalene	BN-1,2-Naph	BN-2,1-Naph	BN-2,3-Naph	BN-1,9-Naph	BN-9,1-Naph	BN-9,10-Naph
Ground state dipole moment							
[Debye]	0.0	1.55	1.71	2.56	2.51	2.54	1.69
First excited state dipole moment							
[Debye]	0.0	2.70	3.33	2.36	1.03	1.39	2.39
Electrostatic potential map							
HOMO [eV]	-7.39	-7.70	-7.22	-6.76	-7.10	-6.73	-7.57
LUMO [eV]	0.00	-0.10	0.39	-0.45	-0.48	-0.12	0.14
H-L gap [eV]	7.40	7.60	7.61	6.31	6.62	6.61	7.71
IE [eV]	8.07	8.32	7.87	7.39	7.71	7.34	8.25
EA [eV]	-0.43	-0.30	-0.77	0.04	0.11	-0.22	-0.55
Δ (IE+EA) [eV]	7.64	8.02	7.10	7.44	7.82	7.12	7.71
optical gap [eV]	4.73	4.66	4.63	3.75	3.98	3.89	4.89

1.2.3. Single-Crystal X-Ray Structures of BN-2,1-Naphthalenes.

Single crystals of *N-H-B-Ph-BN-2,1-naphthalene* were grown by slow evaporation of a Et₂O/pentane solution, and single crystals of *N-H-B-Mes-BN-2,1-naphthalene* were grown from a Et₂O/pentane solution at -30 °C. The dihedral angles of the phenyl and mesityl groups to the BN-2,1-naphthalene plane in solid state are 45.1° and 88.5°, respectively (Figure 1.11). In addition, *N-H-B-Ph-BN-2,1-naphthalene* packs in asymmetric face-to-face dimers featuring 3.45 Å average spacing, whereas *N-H-B-Mes-BN-2,1-naphthalene* packs with the herringbone motif (Figure 1.12).

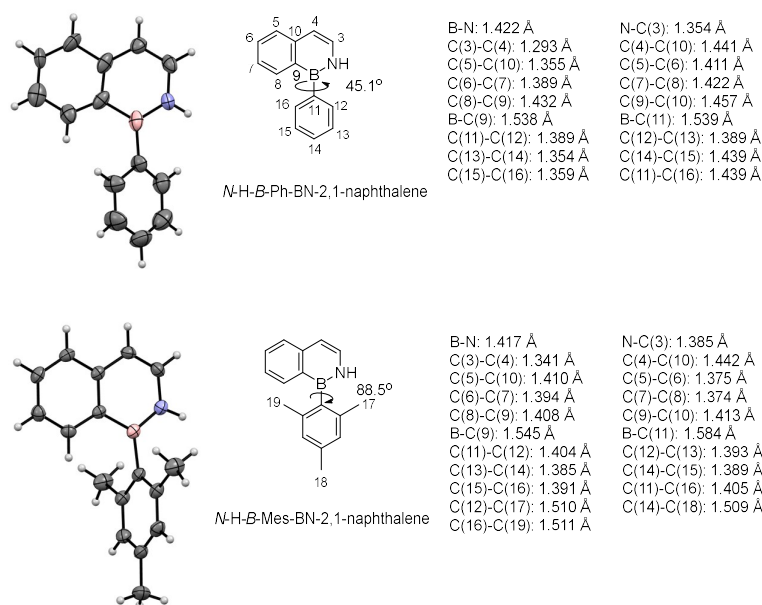


Figure 1.11. Solid-state structures of *N-H-B-Ph-BN-2,1-naphthalene* and *N-H-B-Mes-BN-2,1-naphthalene*. Thermal ellipsoids are set at the 50% probability level.

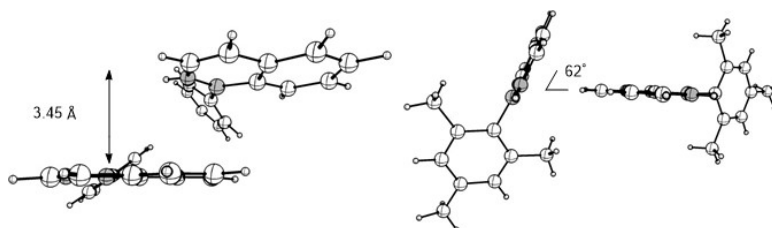


Figure 1.12. The face-to-face π -stacking of *N-H-B-Ph-BN-2,1-naphthalene* and the edge-to-face π -stacking of *N-H-B-Mes-BN-2,1-naphthalene*.

Crystal data and structure refinement for *N-H-B-Ph-BN-2,1-Naphthalene*.

Identification code	C14H12BN	
Empirical formula	C14 H12 B N	
Formula weight	205.06	
Temperature	173(2) K	
Wavelength	1.54178 Å	
Crystal system	Monoclinic	
Space group	Cc	
Unit cell dimensions	a = 15.4481(9) Å	a = 90°.
	b = 15.4554(7) Å	b = 98.891(5)°.
	c = 37.579(3) Å	g = 90°.
Volume	8864.5(10) Å ³	
Z	32	
Density (calculated)	1.229 Mg/m ³	
Absorption coefficient	0.535 mm ⁻¹	
F(000)	3456	
Crystal size	0.320 x 0.220 x 0.200 mm ³	
Theta range for data collection	4.071 to 66.631°.	
Index ranges	-18<=h<=17, 0<=k<=18, 0<=l<=44	
Reflections collected	7790	
Independent reflections	7790 [R(int) = ?]	
Completeness to theta = 66.631°	98.6 %	
Absorption correction	Semi-empirical from equivalents	
Max. and min. transmission	0.7528 and 0.3954	
Refinement method	Full-matrix least-squares on F ²	
Data / restraints / parameters	7790 / 2 / 1155	
Goodness-of-fit on F ²	1.070	
Final R indices [I>2sigma(I)]	R1 = 0.0842, wR2 = 0.2403	
R indices (all data)	R1 = 0.0873, wR2 = 0.2444	
Extinction coefficient	0.00030(9)	
Largest diff. peak and hole	0.554 and -0.374 e.Å ⁻³	

Crystal data and structure refinement for *N-H-B-Mes-BN-2,1-Naphthalene*.

Identification code	C17H18BN
Empirical formula	C17 H18 B N
Formula weight	247.13
Temperature	173(2) K
Wavelength	1.54178 Å
Crystal system	Orthorhombic
Space group	P2 ₁ 2 ₁ 2 ₁
Unit cell dimensions	a = 7.3908(5) Å a = 90°. b = 18.4518(13) Å b = 90°. c = 20.9766(15) Å g = 90°.
Volume	2860.7(3) Å ³
Z	8
Density (calculated)	1.148 Mg/m ³
Absorption coefficient	0.491 mm ⁻¹
F(000)	1056
Crystal size	0.310 x 0.210 x 0.170 mm ³
Theta range for data collection	3.190 to 66.728°.
Index ranges	-8<=h<=8, -21<=k<=21, -23<=l<=24
Reflections collected	51395
Independent reflections	5042 [R(int) = 0.0316]
Completeness to theta = 66.728°	99.3 %
Absorption correction	Semi-empirical from equivalents
Max. and min. transmission	0.7528 and 0.7121
Refinement method	Full-matrix least-squares on F ²
Data / restraints / parameters	5042 / 0 / 356
Goodness-of-fit on F ²	1.046
Final R indices [I>2sigma(I)]	R1 = 0.0311, wR2 = 0.0854
R indices (all data)	R1 = 0.0314, wR2 = 0.0858
Absolute structure parameter	0.2(5)
Extinction coefficient	n/a
Largest diff. peak and hole	0.161 and -0.147 e.Å ⁻³

1.3. Conclusion

In conclusion, we synthesized BN-2,1-naphthalene derivatives and investigated the optoelectrical properties of *N*-TBS-*B*-Mes-BN-2,1-naphthalene and *N*-H-*B*-Mes-BN-2,1-naphthalene using UV-PES technique. The first ionization energies of *N*-TBS-*B*-Mes-BN-2,1-naphthalene and *N*-H-*B*-Mes-BN-2,1-naphthalene are located at 7.6 eV and 7.8 eV, respectively, which indicates the destabilization of HOMO by the substitution of the silicon group. The photophysical properties of *N*-H-*B*-Ph-BN-2,1-naphthalene and *N*-H-*B*-Mes-BN-2,1-naphthalene are investigated via UV-Vis and fluorescence spectroscopy. These two compounds show similar absorption and emission spectra. We further establish with the comparison between derivatives of BN-1,2-naphthalene and BN-2,1-naphthalene that orientational BN/CC isosteres exhibit vary similar absorption behavior. From the solid structures, *N*-H-*B*-Ph-BN-2,1-naphthalene shows face-to-face π -stacking and *N*-H-*B*-Mes-BN-2,1-naphthalene shows the edge-to-face π -stacking.

En conclusion, nous avons synthétisé des dérivés du BN-2,1-naphtalène et étudié les propriétés optoélectriques du *N*-TBS-*B*-Mes-BN-2,1-naphtalène et du *N*-H-*B*-Mes-BN-2,1-naphtalène en utilisant la spectroscopie photoélectronique à rayonnement UV (UV-PES). Les premières énergies d'ionisation du *N*-TBS-*B*-Mes-BN-2,1-naphtalène et du *N*-H-*B*-Mes-BN-2,1-naphtalène se situent respectivement à 7,6 eV et 7,8 eV, ce qui indique la déstabilisation de l'HOMO par la substitution du groupe contenant le silicium. Les propriétés photophysiques du *N*-H-*B*-Ph-BN-2,1-naphtalène et du *N*-H-*B*-Mes-BN-2,1-naphtalène sont étudiées par spectroscopie UV-Vis et de fluorescence. La comparaison entre les dérivés du BN-1,2-naphtalène et du BN-2,1-naphtalène montre que les isostères BN/CC présentent un comportement d'absorption très similaire. Ces deux composés présentent des spectres d'absorption et d'émission similaires. D'après les structures solides, le *N*-H-*B*-Ph-BN-2,1-naphtalène présente un empilement π face à face et le *N*-H-*B*-Mes-BN-2,1-naphtalène présente un empilement π bord à bord.

1.4 Experimental Section

All commercially available starting materials and reagents were purchased from Sigma-Aldrich, Fisher, Strem, TCI or Oakwood and used as received. Commonly used solvents such as methylene chloride, toluene, pentane, diethyl ether and tetrahydrofuran were purified by passing through a neutral alumina column and dispensed from a solvent purification system under argon.

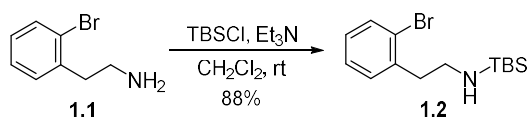
All air- and moisture-sensitive synthesis were carried out in oven-dried glassware under an inert atmosphere using the standard Schlenk technique or a nitrogen-filled glove box. Partial reagents involving mesitylene, cyclohexene and neohexene were dried over 3 Å molecular sieves, and distilled under nitrogen. Palladium on activated carbon catalyst was dried under vacuum in a 180 °C oil bath for 16 hours. Silica gel (240-300 mesh) was dried under vacuum in a 180 °C oil bath for 16 hours for all chromatography involving air- and moisture-sensitive compounds. Chromatography was carried out into a glove box using dry solvents.

¹H NMR, ¹³C NMR and ¹¹B NMR spectra were measured on a Varian Unity Inova 500 MHz or a Bruker 400 MHz spectrometer. BF₃•Et₂O (δ = 0.0 ppm) was used as an external reference in ¹¹B NMR spectra. All IR spectra were measured on a Bruker Alpha-P FT-IR. High-resolution mass spectrometry (HRMS) data were generated in Boston College facilities using direct analysis in real-time (DART) on a JEOL AccuTOF DART spectrometer or electrospray ionization (ESI) on an Advion Expression CMS. Single-crystal X-ray diffraction data were generated in Boston College facilities from measurements with a Bruker Kappa Apex Duo fully automated diffractometer. UV-visible absorption spectra were acquired on a Cary 100 spectrometer equipped with a Quantum Northwest TLC-42 dual cuvette temperature controller at 25.00 °C ± 0.05 °C. Emission spectra were acquired on a Quanta Master 40 spectrofluorimeter (Photon Technology International) equipped with a Quantum Northwest TLC-50 temperature controller set at 25.00 °C ± 0.05 °C. Fluorescence quantum yields were determined using the comparative method, referenced to anthracene (ΦF = 0.36). Quantum yields were determined in cyclohexane solutions at

room temperature using the method described by Jobin Yvon Horiba company with perylene in cyclohexane as the reference standard. *N*-H-*B*-Mes-BN-2,1-naphthalene: Single crystals were grown from a Et₂O/pentane solution at -30 °C. Quantum yield was measured with 268 nm excitation. *N*-H-*B*-Ph-BN-2,1-naphthalene: Single crystals were grown by slow evaporation of a Et₂O/pentane solution. Quantum yield was measured with 269 nm excitation.

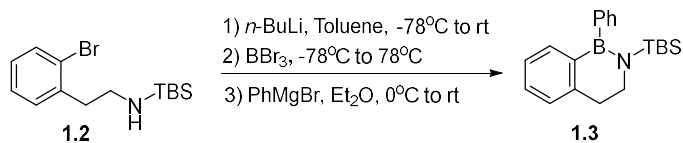
Synthetic Details

N-(2-bromophenethyl)-1-(tert-butyl)-1,1-dimethylsilanamine (**1.2**)



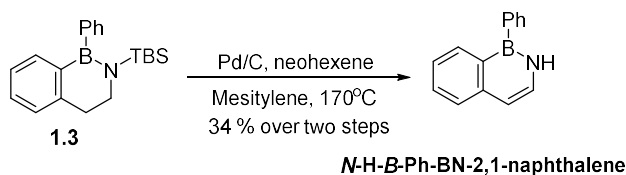
In a 250 mL round-bottomed flask, compound **1.1** (5.0 g, 25 mmol, 1.0 equiv.) and anhydrous triethylamine (5.2 mL, 37 mmol, 1.5 equiv.) were combined in anhydrous methylene chloride (40 mL), followed by the addition of *tert*-butylchlorodimethylsilane (3.8 g, 25 mmol, 1.0 equiv.) under ice-cold bath. The reaction mixture was allowed to warm up to room temperature and stirred under nitrogen for 12 hours. The methylene chloride solvent was subsequently removed using a rotary evaporator. The residue was taken up in 150 mL pentane and the salt was removed by filter paper, then the filtrate was concentrated using a rotary evaporator. The resulting crude material was purified using distillation under reduced pressure (150 °C at 0.5 Torr) to yield a bright yellow oil (6.7 g, 88%). ¹H NMR (500 MHz, CDCl₃) δ 7.53 (d, *J* = 10.0 Hz, 1H), 7.25 – 7.19 (m, 2H), 7.06 (t, *J* = 5.0 Hz, 1H), 3.01 (dd, *J* = 15.0, 6.5 Hz, 2H), 2.82 (t, *J* = 5.0 Hz, 2H), 0.86 (s, 9H), 0.42 (br, 1H), -0.04 (s, 6H). ¹³C NMR (126 MHz, CDCl₃) δ 139.6, 132.7, 131.1, 127.6, 127.2, 124.6, 42.7, 41.7, 26.4, 18.2, -5.0.

N-TBS-*B*-Ph-*BN*-2,1-dihydronaphthalene (**1.3**)



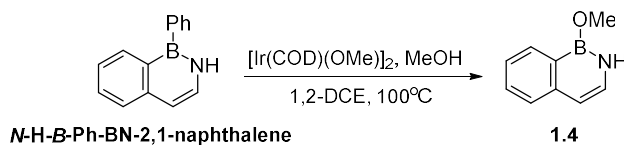
In a 50 mL round-bottomed flask, compound **1.2** (2.21 g, 7.00 mmol, 1.00 equiv.) was dissolved in dry toluene (12 mL). This solution was cooled to -78 °C and then a solution of *n*-butyllithium (2.5 M in hexane, 5.90 mL, 14.7 mmol, 2.10 equiv.) was added dropwise to the solution via syringe. At the conclusion of the addition, the reaction mixture was allowed to warm to room temperature over one hour, it was stirred for another 12 hours at room temperature. A solution of boron tribromide (1.93 g, 7.70 mmol, 1.10 equiv.) in anhydrous toluene (2 mL) was added dropwise to the reaction mixture at -78 °C via syringe before allowing the mixture to warm to room temperature over 1 hour. The mixture was stirred at room temperature for 6 hours before warming the mixture to 78 °C and allowing it to stir at 78 °C for 12 hours. The formation of B-Br intermediate could be observed by ¹¹B NMR (160 MHz, CDCl₃) δ 39.4 (s). At the conclusion of the reaction, the reaction mixture was cooled to room temperature and then the generated lithium bromide salt was removed through filter paper in a glove box. The filtrate was concentrated to dryness using Schlenk line, and the residue was dissolved in anhydrous diethyl ether (10 mL). A solution of phenylmagnesium bromide (1.0 M in THF, 7.00 mL, 7.00 mmol, 1.00 equiv.) was added dropwise to the solution via syringe under ice-cold bath. The mixture was stirred at room temperature for 2 hours before allowing the mixture to warm to room temperature over 1 hour. The formation of the desired product could be observed by ¹¹B NMR (160 MHz, CDCl₃) δ 44.2 (s). At the conclusion of the reaction, the mixture was passed through a filter paper in a glove box. The filtrate was concentrated to dryness using Schlenk line, and the residue was dissolved in dry pentane (10 mL) and subsequently passed through an acrodisc to remove extra remained salts. The filtrate was concentrated to dryness using Schlenk line, and the resulting crude product **1.3** (assuming 100% yield), a yellow oil, was carried forward without further purification because of decomposition on silica gel plug.

N-H-*B*-Ph-*N*-TBS-*BN*-2,1-naphthalene



In a glove box, crude starting material **1.3** (2.24 g, 6.97 mmol, 1.00 equiv.) was dissolved in 10 mL dry mesitylene, followed by the addition of neohexene (1.20 mL, 9.77 mmol, 1.40 equiv.) and dry Pd/C (10 wt. %, 734 mg, 0.697 mmol, 0.100 equiv.) in a 50 mL round-bottomed flask with a condenser. The mixture was subsequently removed from the glovebox and heated to reflux in a 170 °C oil bath for 72 hours. At the conclusion of the reaction, the reaction mixture was allowed to cool to room temperature, and the Pd/C was removed through a filter paper in a glove box. The filtrate was passed through a silica gel plug using pentane/methylene chloride (20:1) as the mobile phase in a glove box. The resulting solution was concentrated using a rotary evaporator to yield the desired product as a white solid (764 mg, 34%). ¹H NMR (500 MHz, CDCl₃) δ 8.25 (d, *J* = 10.0 Hz, 1H), 7.77 (d, *J* = 5.0 Hz, 1H), 7.72 – 7.62 (m, 3H), 7.52 – 7.43 (m, 3H), 7.40 (t, *J* = 5.0 Hz, 1H), 7.30 (t, *J* = 5.0 Hz, 1H), 6.73 (d, *J* = 5.0 Hz, 1H). ¹³C NMR (126 MHz, CDCl₃) δ 142.0, 135.4, 133.3, 130.6, 129.6, 128.5, 128.0, 126.6, 124.5, 111.1. Carbon adjacent to boron was not observed. ¹¹B NMR (160 MHz, CDCl₃) δ 37.3 (s).

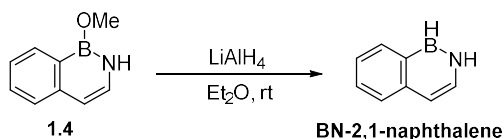
N-H-B-OMe-BN-2,1-naphthalene (1.4)



The compound *N-H-B-Ph-N-TBS-BN-2,1-naphthalene* (205 mg, 1.00 mmol, 1.00 equiv.) was combined in a 10 mL pressure vessel with Ir(COD)(OMe) dimer (33.0 mg, 0.05 mmol, 0.05 equiv.), anhydrous methanol (0.40 mL, 10.0 mmol, 10.0 equiv.) and 1.5 mL anhydrous 1,2-dichloroethane. The pressure vessel was sealed and heated to 100 °C for 24 hours. The mixture was cooled to room temperature, and then subjected to a quick silica gel chromatography using diethyl ether as the eluent in a glove box. The resulting solution was concentrated using Schlenk line to afford a yellow oil as the

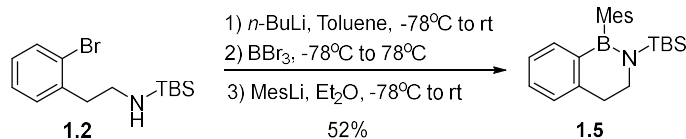
crude product (83 % NMR conversion). ^1H NMR (500 MHz, CDCl_3) δ 8.08 (d, $J = 5.0$ Hz, 1H), 7.54 (t, $J = 5.0$ Hz, 1H), 7.47 (d, $J = 10.0$ Hz, 1H), 7.33 (t, $J = 5.0$ Hz, 1H), 6.95 (t, $J = 5.0$ Hz, 1H), 6.39 (br, 1H), 6.27 (d, $J = 5.0$ Hz, 1H), 3.81 (s, 3H). ^{11}B NMR (160 MHz, CDCl_3) δ 29.2 (s).

BN-2,1-naphthalene.



In a glove box, the compound **1.4** (159 mg, 1.00 mmol, 1.00 equiv.) was dissolved in 5 mL anhydrous diethyl ether. A suspension of lithium aluminum hydride (78.0 mg, 2.00 mmol, 2.00 equiv.) in 2 mL dry diethyl ether was added slowly to the solution via a syringe. The mixture was stirred at room temperature for 2 hours in a glove box. At the conclusion of the reaction, the mixture was passed through a filter paper, and the filtrate was concentrated Schlenk line. The resulting residue was dissolved in 5 mL anhydrous pentane and passed through a filter paper. The filtrate was concentrated Schlenk line and purified via a silica gel plug using pentane/diethyl ether (20:1) as the eluent in a glove box. The desired product was observed from crude ^1H NMR and ^{11}B NMR. ^{11}B NMR (160 MHz, CDCl_3) δ 35.2 (d, $J_{\text{BH}} = 91.2$ Hz).

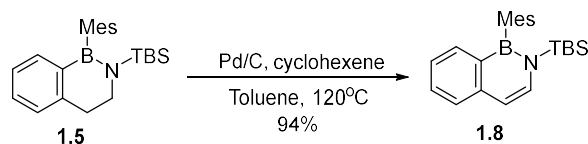
B-Mes-*N*-TBS-BN-2,1-dihydronaphthalene (**1.5**)



In a 100 mL round-bottomed flask, compound **1.2** (1.57 g, 5.00 mmol, 1.00 equiv.) was dissolved in dry toluene (10 mL), and then a solution of *n*-butyllithium (2.5 M in hexane, 4.60 mL, 10.5 mmol, 2.10 equiv.) was added dropwise to the solution via syringe at -78°C . At the conclusion of the addition, the reaction mixture was allowed to warm to room temperature over one hour and stirred for another 12 hours at room temperature. A solution of boron tribromide (1.38 g, 5.50 mmol, 1.10 equiv.) in anhydrous toluene (2.0 mL) was added dropwise to the reaction mixture at -78°C via syringe before allowing the mixture to warm to room temperature over 1 hour. The mixture was stirred

at room temperature for 6 hours before warming the mixture to 78 °C and allowing it to stir at 78 °C for 12 hours. At the conclusion of the reaction, the reaction mixture was cooled to room temperature and then passed through a filter paper in a glove box. The filtrate was concentrated to dryness using Schlenk line, and the residue was dissolved in anhydrous diethyl ether (10 mL). A suspension of mesityllithium (756 mg, 6.00 mmol, 1.20 equiv.) in 10 mL dry diethyl ether was added slowly to the solution via a syringe under -78 °C. The mixture was stirred at room temperature for 2 hours before allowing the mixture to warm to room temperature over 1 hour. At the conclusion of the reaction, the mixture was quenched with 100 mL water at 0 °C, and then extracted three times with Et₂O. The combined organic fraction was dried by anhydrous Na₂SO₄ and then passed through a filter paper. The filtrate was concentrated and purified via a silica gel plug using hexane/methylene chloride (10:1) as the eluent. The desired product was obtained as a white solid (945 mg, 52%). ¹H NMR (500 MHz, CDCl₃) δ 7.32 (t, *J* = 10.0 Hz, 1H), 7.20 (d, *J* = 5.0 Hz, 1H), 7.11 (t, *J* = 10.0 Hz, 1H), 7.07 (d, *J* = 5.0 Hz, 1H), 6.81 (s, 2H), 3.43 (t, *J* = 5.0 Hz, 2H), 2.95 (t, *J* = 5.0 Hz, 2H), 2.34 (s, 3H), 2.15 (s, 6H), 1.01 (s, 9H), -0.11 (s, 6H). ¹³C NMR (126 MHz, CDCl₃) δ 144.0, 138.5, 136.2, 135.2, 130.2, 126.7, 126.2, 126.0, 44.8, 33.4, 28.0, 22.4, 21.2, 19.4, -4.0. Carbon adjacent to boron was not observed. ¹¹B NMR (160 MHz, CDCl₃) δ 45.0 (s).

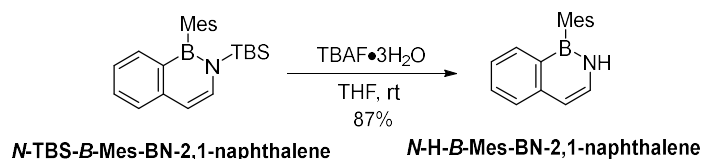
N-TBS-*B*-Mes-BN-2,1-naphthalene.



The compound **1.5** (182 mg, 0.500 mmol, 1.00 equiv.) was combined in a 25 mL pressure vessel with Pd/C (10 wt.%, 60.0 mg, 0.05 mmol, 0.10 equiv.), cyclohexene (0.12 mL, 1.2 mmol, 2.4 equiv.) and 2.5 mL toluene. The pressure vessel was sealed and heated to 120 °C for 20 hours. After cooling to room temperature, the mixture was passed through an acrodisc. The filtrate was subjected to silica gel chromatography (hexane: methylene chloride =10:1) to yield a white solid (170 mg, 94%). ¹H NMR (400 MHz, CDCl₃) δ 7.59 – 7.53 (m, 2H), 7.47 (d, *J* = 8.0 Hz, 1H), 7.34 (d, *J* = 8.0 Hz,

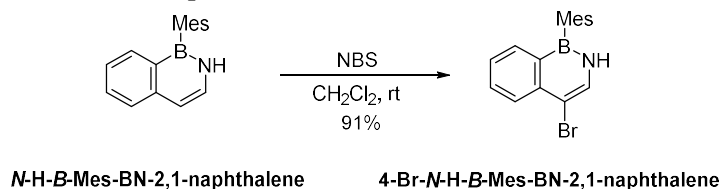
1H), 7.23 – 7.18 (m, 1H), 6.85 (s, 2H), 6.72 (d, $J = 8.0$ Hz, 1H), 2.36 (s, 3H), 2.04 (s, 6H), 0.97 (s, 9H), 0.04 (s, 6H). ^{13}C NMR (101 MHz, CDCl_3) δ 140.2, 139.4, 136.7, 135.8, 134.1, 130.9, 126.8, 125.5, 124.6, 111.8, 27.7, 23.3, 21.3, 19.5, 3.2. Carbon adjacent to boron was not observed. ^{11}B NMR (160 MHz, CDCl_3) δ 43.4 (s).

N-H-*B*-Mes-BN-2,1-naphthalene



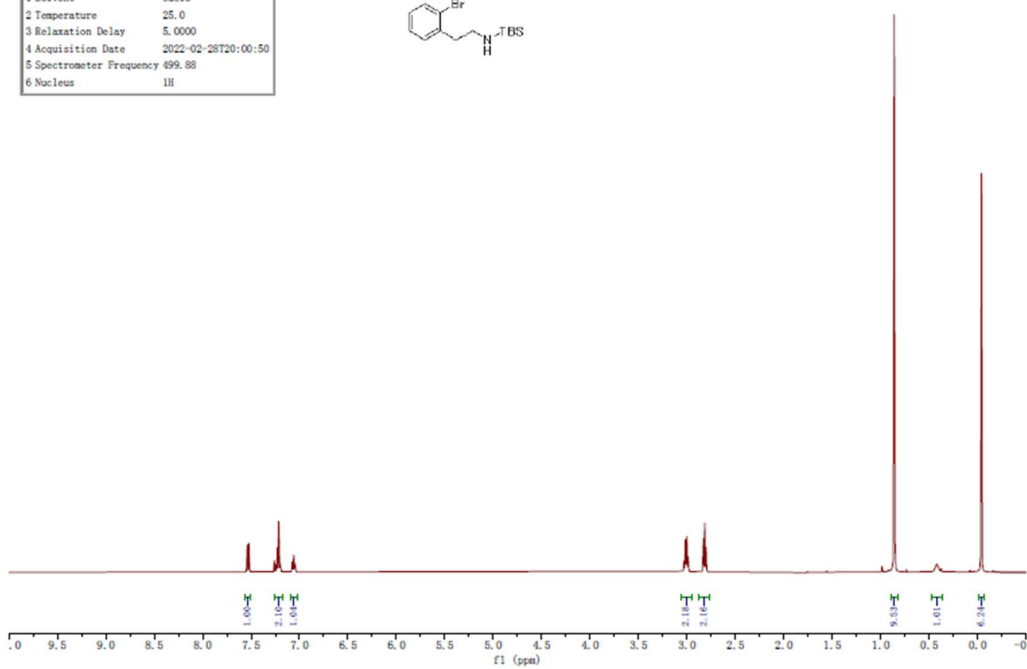
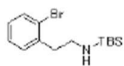
The compound *N*-TBS-*B*-Mes-BN-2,1-naphthalene (370 mg, 1.02 mmol, 1.00 equiv.) was dissolved in 5.0 mL THF. A solution of tetrabutylammonium fluoride trihydrate (388 mg, 1.23 mmol, 1.20 equiv.) in 3.0 mL THF was added to the mixture. The reaction mixture was stirred for 4 hours at room temperature. At the conclusion of the reaction, the reaction mixture was concentrated using a rotary evaporator. 50 mL water was added to the residue and subsequently extracted three times with ethyl acetate. The combined organic fraction was dried by anhydrous Na_2SO_4 and then passed through a filter paper. The filtrate was concentrated and purified via silica gel chromatography using hexane/methylene chloride (4:1) as the eluent. The desired product was obtained as a white solid (220 mg, 87%). ^1H NMR (500 MHz, CDCl_3) δ 7.80 (d, $J = 5.0$ Hz, 1H), 7.71 (d, $J = 8.0$ Hz, 1H), 7.67 (t, $J = 5.0$ Hz, 1H), 7.53 (br, 1H), 7.35 (t, $J = 5.0$ Hz, 1H), 7.30 (t, $J = 5.0$ Hz, 1H), 6.99 (s, 2H), 6.76 (d, $J = 5.0$ Hz, 1H), 2.43 (s, 3H), 2.17 (s, 6H). ^{13}C NMR (126 MHz, CDCl_3) δ 141.4, 140.5, 137.4, 135.4, 130.7, 129.6, 127.0, 126.4, 124.4, 110.8, 22.9, 21.2. Carbon adjacent to boron was not observed. ^{11}B NMR (160 MHz, CDCl_3) δ 39.3 (s).

4-Br-*N*-H-*B*-Mes-BN-2,1-naphthalene.

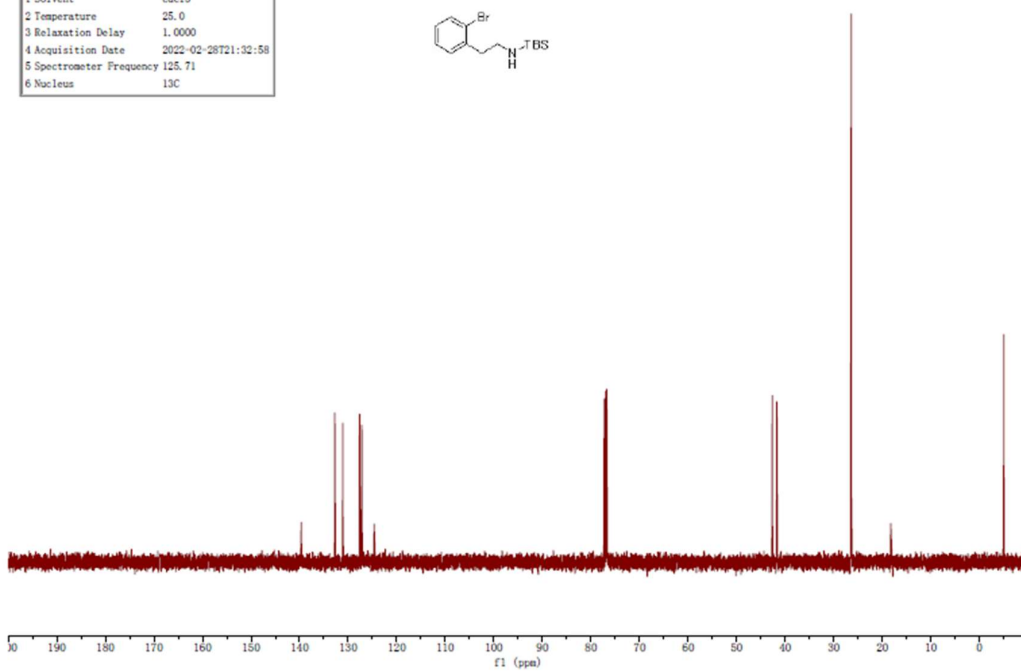
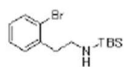


In a glovebox, the compound *N*-H-*B*-Mes-BN-2,1-naphthalene (50 mg, 0.20 mmol, 1.0 equiv.) was dissolved in 2.0 mL dry methylene chloride. N-bromosuccinimide (NBS) (43 mg, 0.24 mmol, 1.2 equiv.) was added to the solution. The reaction mixture was stirred for 4 hours at room temperature. At the conclusion of the reaction, the reaction mixture was concentrated using a rotary evaporator. The resulting residue was purified by silica gel chromatography using solution (pentane: methylene chloride = 4:1) as the eluent to yield the desired product as a white solid (60 mg, 91%). ¹H NMR (400 MHz, CDCl₃) δ 8.10 (d, *J* = 8.0 Hz, 1H), 7.78 – 7.72 (m, 2H), 7.61 (d, *J* = 8.0 Hz, 1H), 7.49 (br, 1H), 7.37 (t, *J* = 8.0 Hz, 1H), 6.94 (s, 2H), 2.38 (s, 3H), 2.10 (s, 6H). ¹³C NMR (101 MHz, CDCl₃) δ 140.4, 139.7, 137.8, 135.8, 131.8, 131.3, 127.1, 126.0, 125.5, 106.1, 22.9, 21.2. Carbon adjacent to boron was not observed. ¹¹B NMR (128 MHz, CDCl₃) δ 39.6 (s).

Parameter	Value
1 Solvent	cdcl3
2 Temperature	25.0
3 Relaxation Delay	5.0000
4 Acquisition Date	2022-02-28T20:00:50
5 Spectrometer Frequency	499.88
6 Nucleus	1H

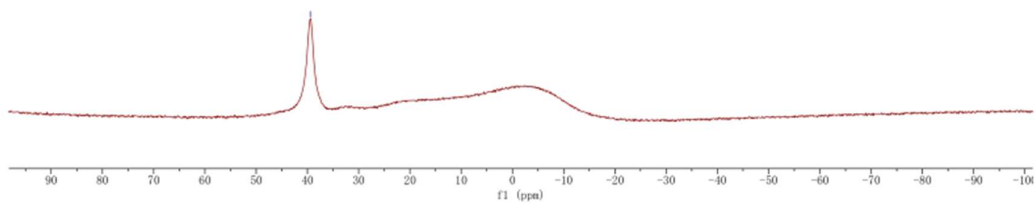
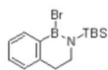


Parameter	Value
1 Solvent	cdcl3
2 Temperature	25.0
3 Relaxation Delay	1.0000
4 Acquisition Date	2022-02-28T21:32:58
5 Spectrometer Frequency	125.71
6 Nucleus	13C



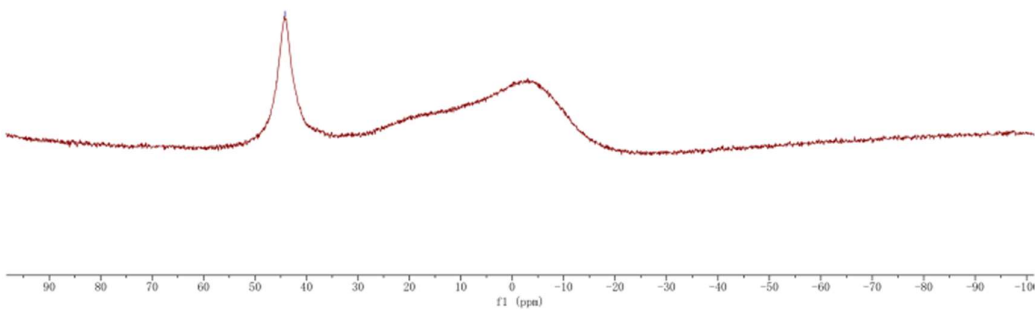
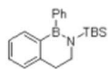
Parameter	Value
1 Solvent	cdcl3
2 Temperature	25.0
3 Relaxation Delay	0.0100
4 Acquisition Date	2022-04-07 15:07:55
5 Spectrometer Frequency	160.38
6 Nucleus	11B

38.45

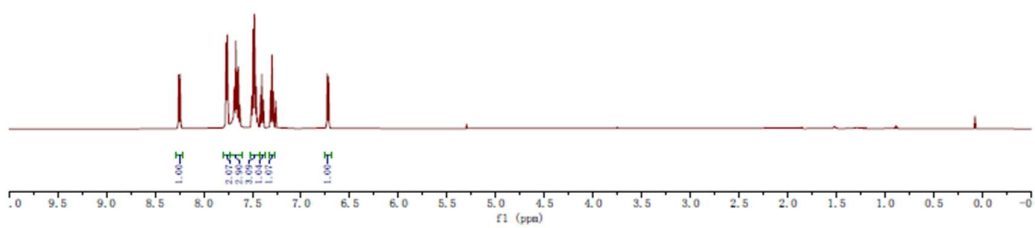


Parameter	Value
1 Solvent	cdcl3
2 Temperature	25.0
3 Relaxation Delay	0.0100
4 Acquisition Date	2022-04-11 11:25:20
5 Spectrometer Frequency	160.38
6 Nucleus	11B

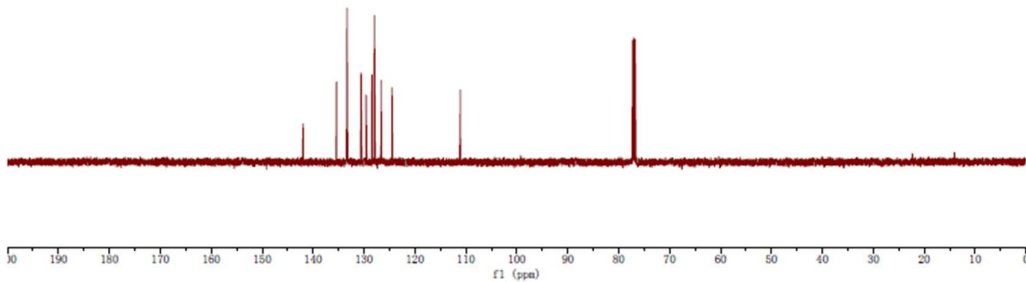
44.18



Parameter	Value
1 Solvent	cdcl3
2 Temperature	25.0
3 Relaxation Delay	10.0000
4 Acquisition Date	2022-06-22T16:45:25
5 Spectrometer Frequency	499.88
6 Nucleus	1H

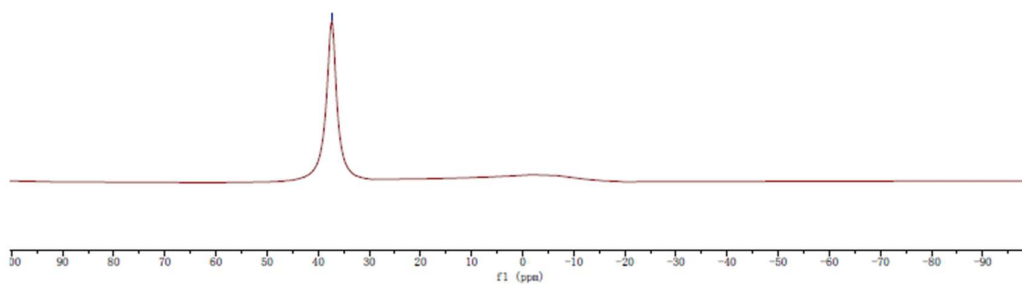


Parameter	Value
1 Solvent	cdcl3
2 Temperature	25.0
3 Relaxation Delay	1.0000
4 Acquisition Date	2022-06-22T14:02:24
5 Spectrometer Frequency	125.71
6 Nucleus	13C



Parameter	Value
1 Solvent	cdcl3
2 Temperature	25.0
3 Relaxation Delay	0.0100
4 Acquisition Date	2022-06-22T13:55:25
5 Spectrometer Frequency	160.38
6 Nucleus	11B

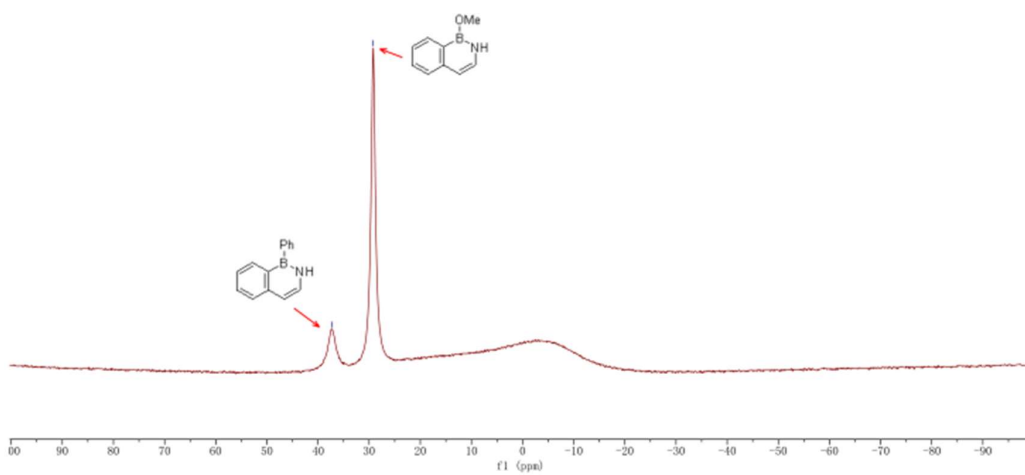
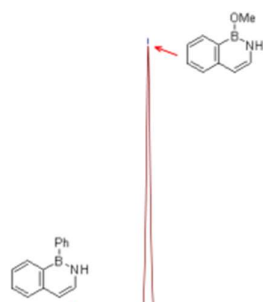
11B



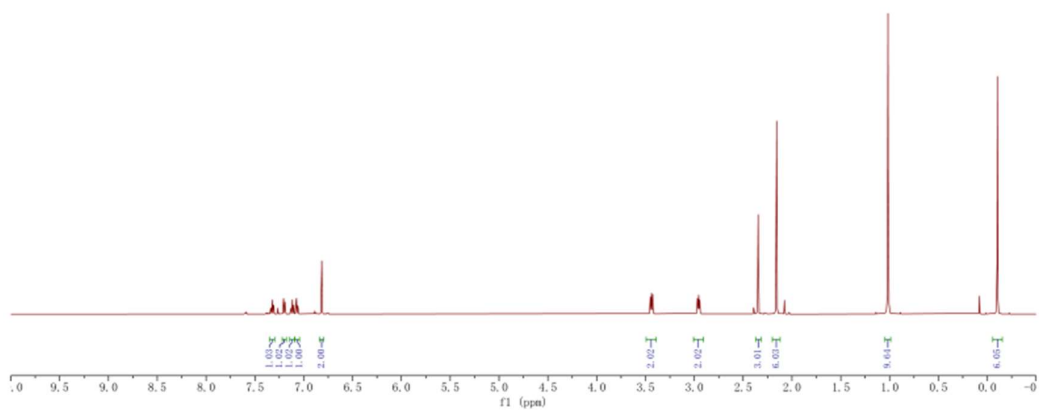
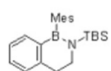
Parameter	Value
1 Solvent	cdcl3
2 Temperature	25.0
3 Relaxation Delay	0.0100
4 Acquisition Date	2022-06-25T14:04:20
5 Spectrometer Frequency	160.38
6 Nucleus	11B

11B

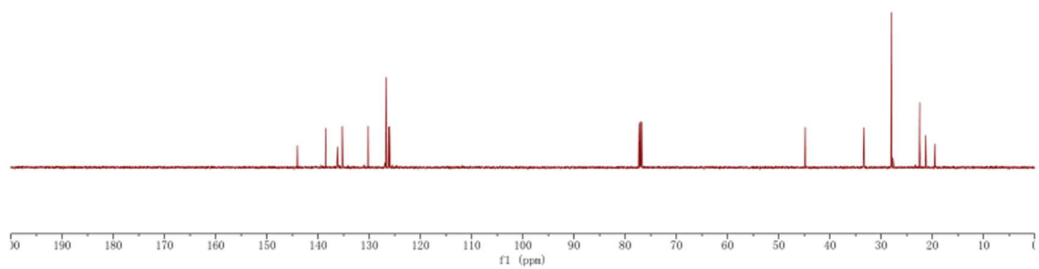
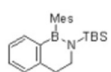
33



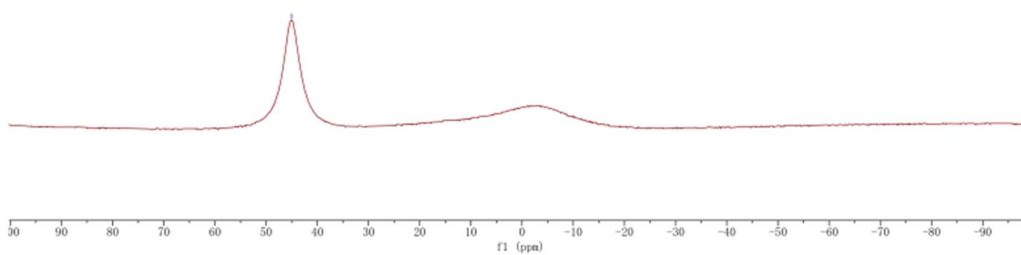
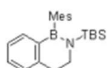
Parameter	Value
1 Solvent	cdcl3
2 Temperature	25.0
3 Relaxation Delay	10.0000
4 Acquisition Date	2022-04-17T23:05:20
5 Spectrometer Frequency	499.88
6 Nucleus	¹ H



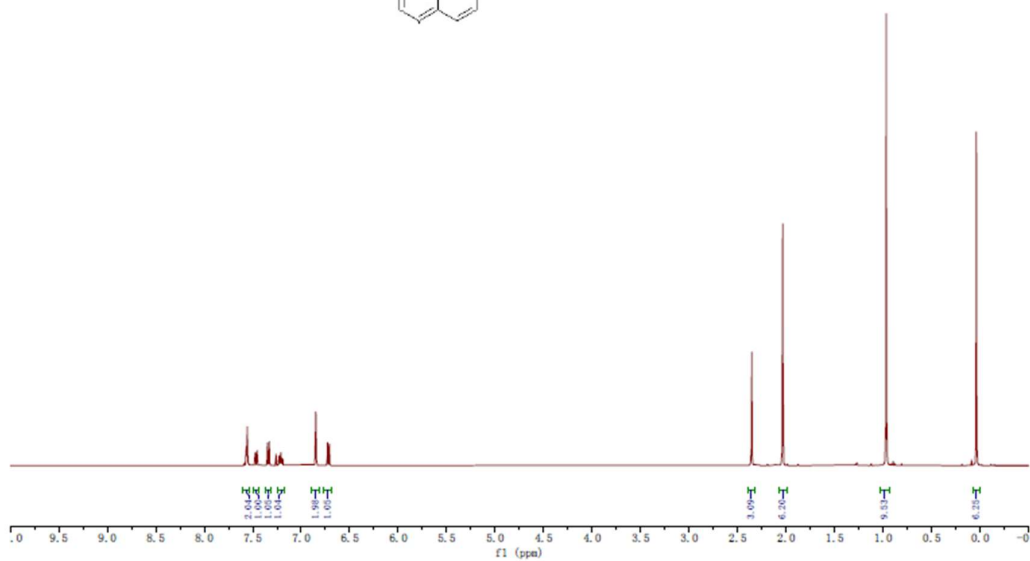
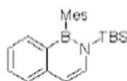
Parameter	Value
1 Solvent	cdcl3
2 Temperature	25.0
3 Relaxation Delay	1.0000
4 Acquisition Date	2022-04-17T23:06:57
5 Spectrometer Frequency	125.71
6 Nucleus	¹³ C



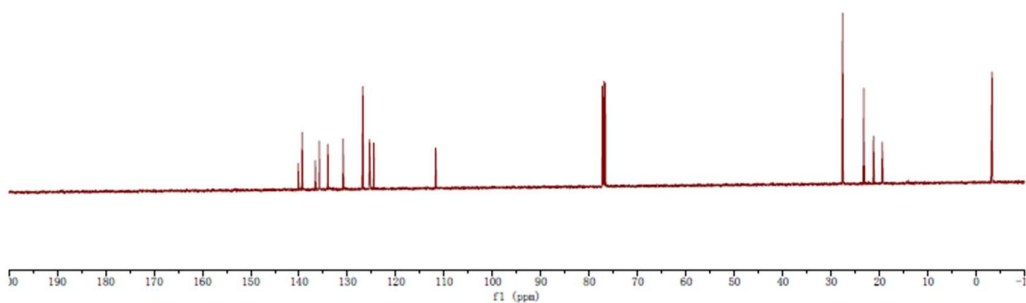
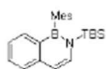
Parameter	Value
1 Solvent	cdcl3
2 Temperature	25.0
3 Relaxation Delay	0.0100
4 Acquisition Date	2022-04-17T23:13:25
5 Spectrometer Frequency	160.38
6 Nucleus	11B



Parameter	Value
1 Solvent	CDCl3
2 Temperature	298.2
3 Relaxation Delay	1.0000
4 Acquisition Date	2023-01-30T16:11:43
5 Spectrometer Frequency	399.98
6 Nucleus	1H

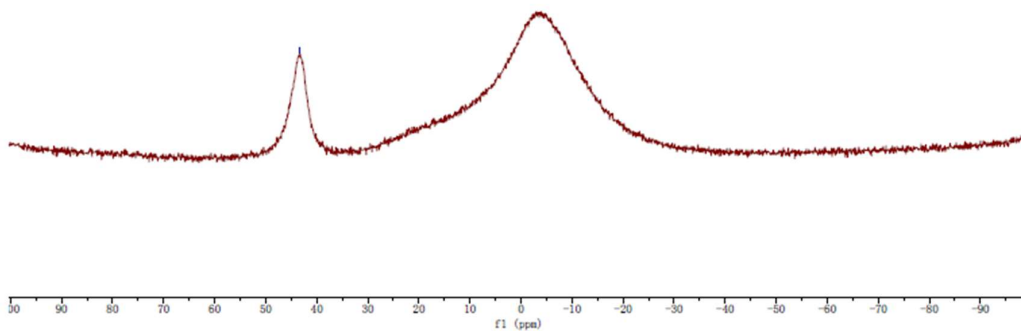
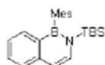


Parameter	Value
1 Solvent	CDCl3
2 Temperature	298.1
3 Relaxation Delay	2.0000
4 Acquisition Date	2023-01-30T16:35:17
5 Spectrometer Frequency	100.59
6 Nucleus	13C

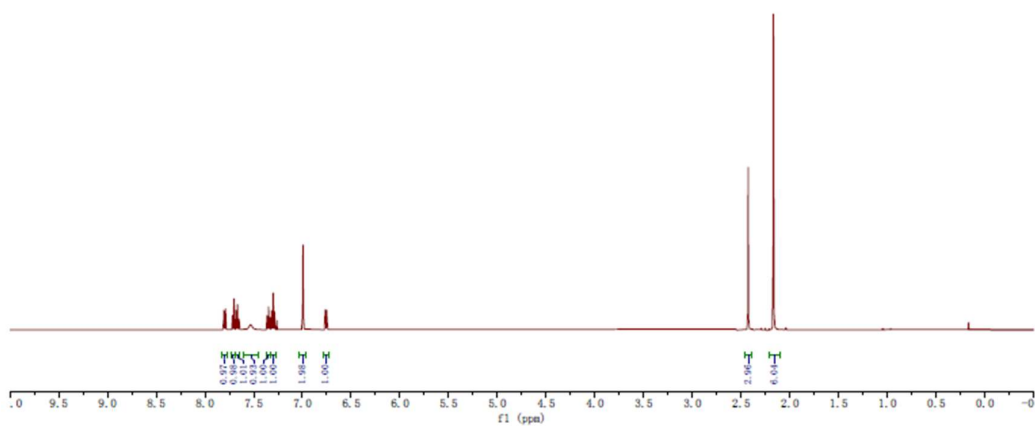


Parameter	Value
1 Solvent	cdcl3
2 Temperature	25.0
3 Acquisition Date	2022-04-08T18:27:07
4 Spectrometer Frequency	160.38
5 Nucleus	11B

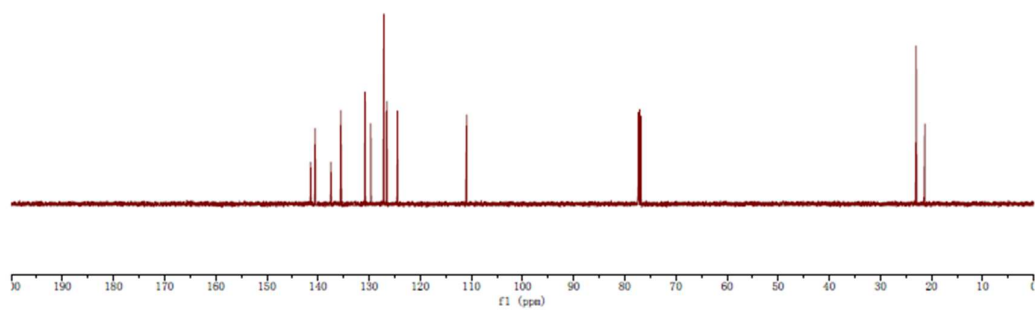
0.00



Parameter	Value
1 Solvent	cdcl3
2 Temperature	25.0
3 Relaxation Delay	10.0000
4 Acquisition Date	2022-04-19T22:28:04
5 Spectrometer Frequency	499.88
6 Nucleus	1H

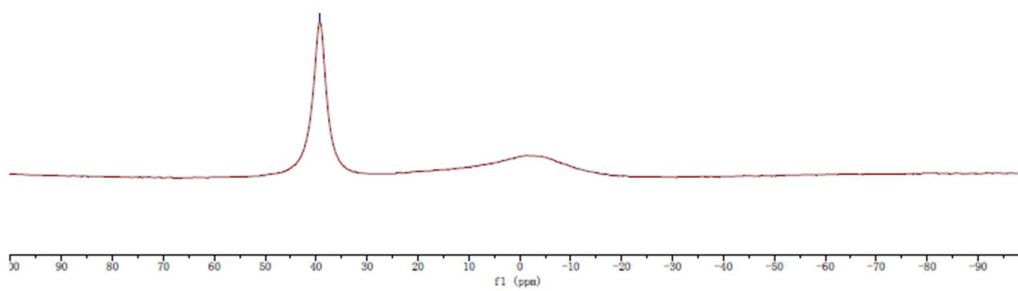


Parameter	Value
1 Solvent	cdcl3
2 Temperature	25.0
3 Relaxation Delay	1.0000
4 Acquisition Date	2022-04-19T22:28:56
5 Spectrometer Frequency	125.71
6 Nucleus	13C

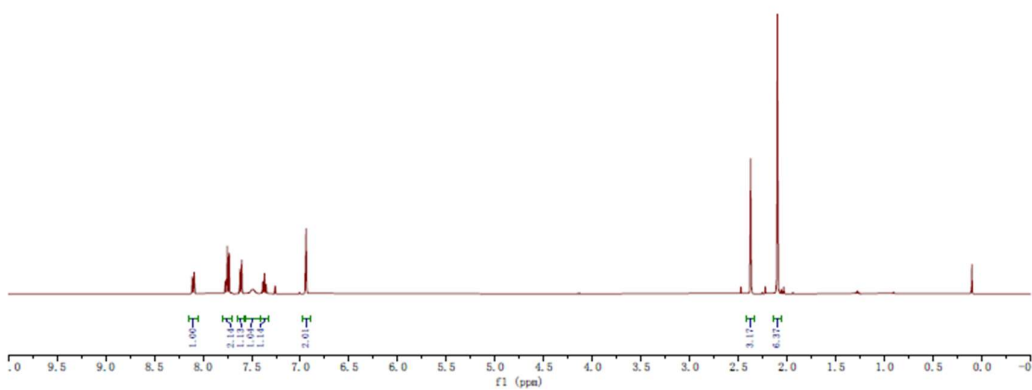


Parameter	Value
1 Solvent	cdcl3
2 Temperature	25.0
3 Relaxation Delay	0.0100
4 Acquisition Date	2022-04-19T22:23:47
5 Spectrometer Frequency	160.38
6 Nucleus	11B

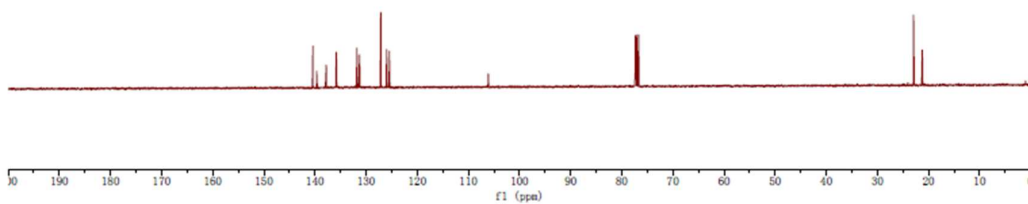
160.38



Parameter	Value
1 Solvent	CDCl3
2 Temperature	298.1
3 Relaxation Delay	1.0000
4 Modification Date	2023-01-31T16:03:08
5 Spectrometer Frequency	399.98
6 Nucleus	1H

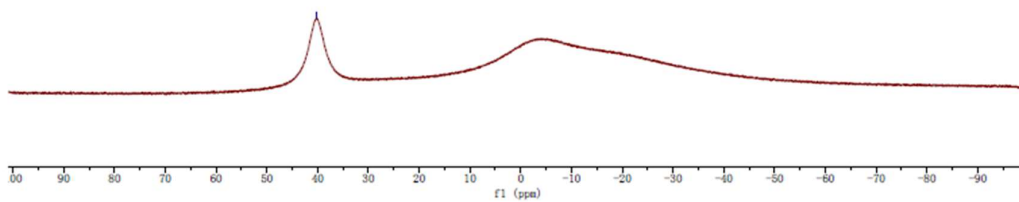


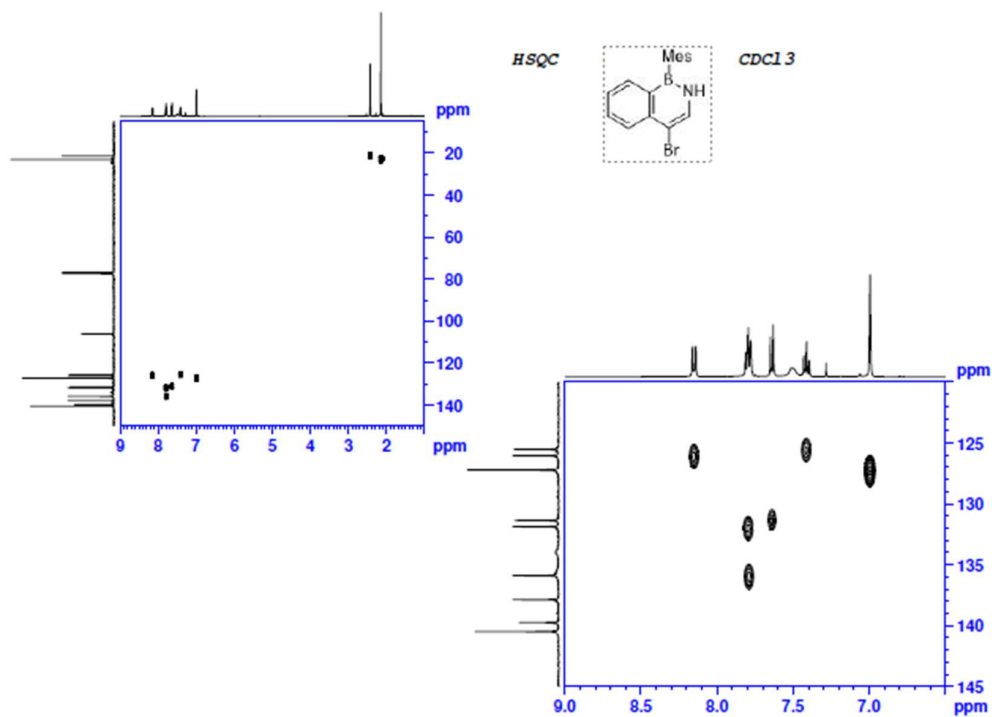
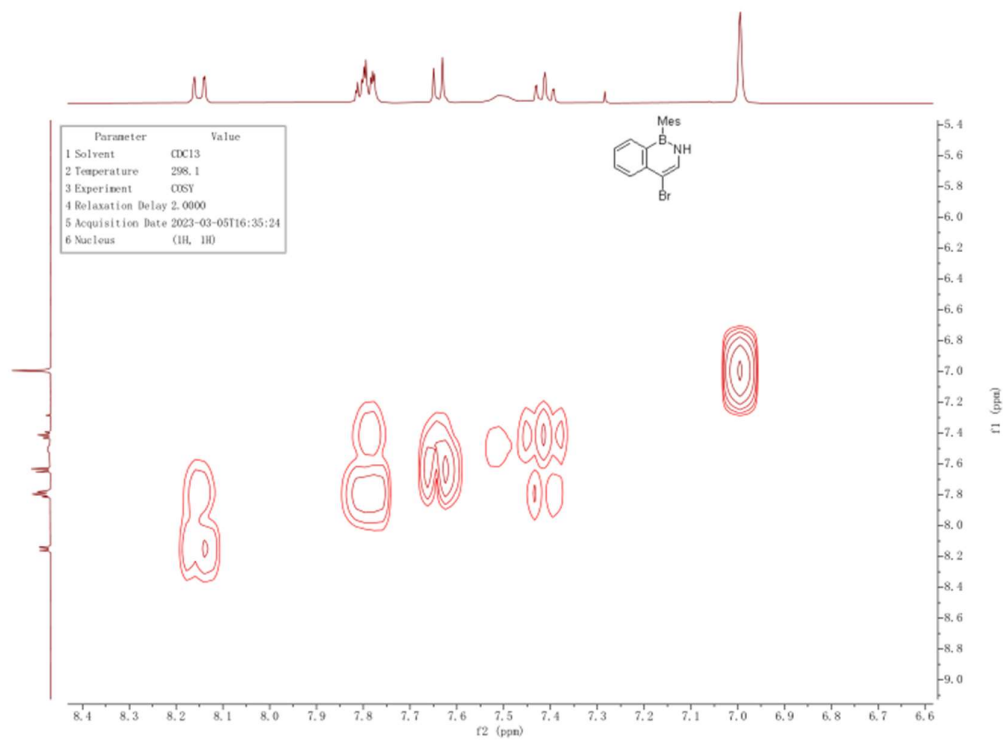
Parameter	Value
1 Solvent	CDCl3
2 Temperature	298.1
3 Relaxation Delay	2.0000
4 Acquisition Date	2023-01-31T17:27:10
5 Spectrometer Frequency	100.59
6 Nucleus	13C

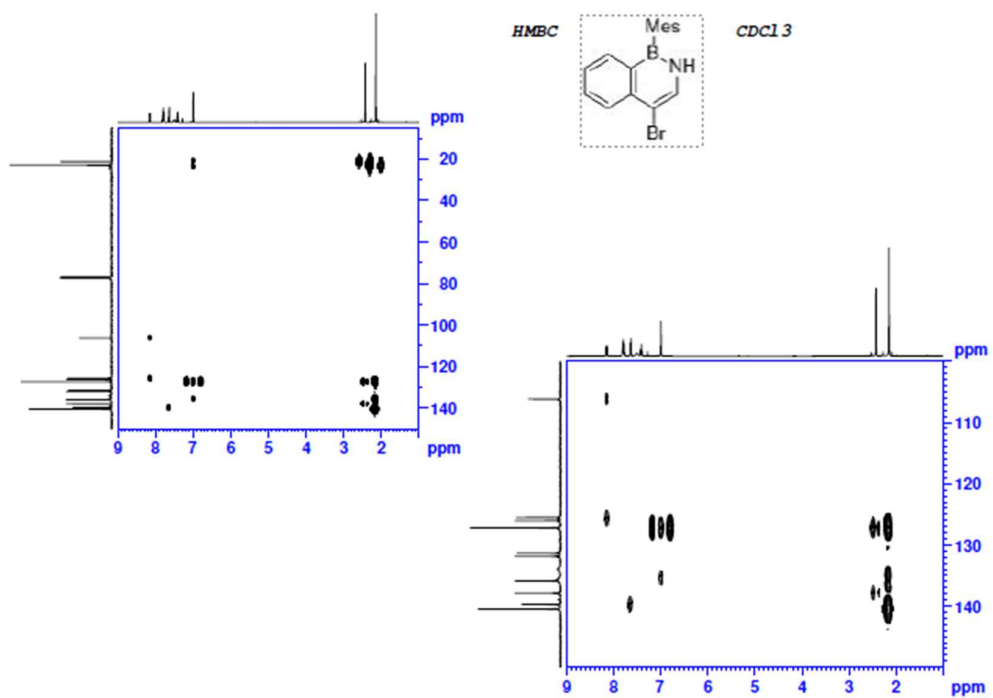


Parameter	Value
1 Solvent	CDCl3
2 Temperature	298.2
3 Relaxation Delay	1.0000
4 Modification Date	2023-01-31T16:09:32
5 Spectrometer Frequency	128.33
6 Nucleus	11B

9.19







Reference

- [1] (a) Bosdet, M. J. D.; Piers, W. E. *Can. J. Chem.* **2009**, *87*, 8–29. (b) Campbell, P. G.; Marwitz, A. J. V.; Liu S.-Y. *Angew. Chem. Int. Ed.* **2012**, *51*, 6074–6092. (c) Giustra, Z. X.; Liu S.-Y. *J. Am. Chem. Soc.* **2018**, *140*, 1184–1194. (d) Liu, Z.; Marder, T. B. *Angew. Chem. Int. Ed.* **2008**, *47*, 242–244.
- [2] Chrostowska, A.; Xu, S.; Lamm, A. N.; Mazière, A.; Weber, C. D.; Dargelos, A.; Baylère, P.; Graciaa, A.; Liu, S.-Y. *J. Am. Chem. Soc.* **2012**, *134*, 10279–10285.
- [3] (a) Kranz, M.; Clark, T. *J. Org. Chem.* **1992**, *57*, 5492–5500. (b) Matus, M. H.; Liu, S.-Y.; Dixon, D. A. *J. Phys. Chem. A.* **2010**, *114*, 2644–2654; (c) Baranac-Stojanovic, M. *Chem. Eur. J.* **2014**, *20*, 16558–16565.
- [4] Dewar, M. J. S.; Kubba, V. P.; Pettit, R. *J. Chem. Soc.* **1958**, 3073–3076.
- [5] Dewar, M. J. S.; Marr, P. A. *J. Am. Chem. Soc.* **1962**, *84*, 3782–3782.
- [6] White, D. G. *J. Am. Chem. Soc.* **1963**, *85*, 3634–3636.
- [7] (a) Ashe, A. J.; Fang, X. *Org. Lett.* **2000**, *2*, 2089–2091. (b) Ashe, A. J.; Fang, X.; Kampf, J. W. *Organometallics.* **2001**, *20*, 5413–5418.
- [8] Braunschweig, H.; Damme, A.; Jimenez-Halla, J. O. C.; Pfaffinger, B.; Radacki, K.; Wolf, J. *Angew. Chem.* **2012**, *124*, 10177–10180.
- [9] (a) Marwitz, A. J. V.; Matus, M. H.; Zakharov, L. N.; Dixon, D. A.; Liu, S.-Y. *Angew. Chem. Int. Ed.* **2009**, *48*, 973–977. (b) Rudebusch, G. E.; Zakharov, L. N.; Liu, S.-Y. *Angew. Chem. Int. Ed.* **2013**, *52*, 9316–9319. (c) Baggett, A. W.; Guo, F.; Li, B.; Liu, S.-Y.; Jäkle, F. *Angew. Chem. Int. Ed.* **2015**, *54*, 11191–11195. (d) Edel, K.; Yang, X.; Ishibashi, J. S. A.; Lamm, A. N.; Maichle-Mössmer, C.; Giustra, Z. X.; Liu, S.-Y.; Bettinger, H. F. *Angew. Chem. Int. Ed.* **2018**, *57*, 5296–5300.
- [10] Xu, S.; Zakharov, L. N.; Liu, S.-Y. *J. Am. Chem. Soc.* **2011**, *133*, 20152–20155. (b) Liu, X.; Zhang, Y.; Li, B.; Zakharov, L. N.; Vasiliu, M.; Dixon, D. A.; Liu, S.-Y. *Angew. Chem. Int. Ed.* **2016**, *55*, 8333–8337.
- [11] (a) Tanjaroorn, C.; Daly, A.; Marwitz, A. J. V.; Liu, S.-Y.; Kukolich, S. G. *J. Chem. Phys.* **2009**, *131*, 224312. (b) Xu, S.; Mikulas, T. C.; Zakharov, L. N.; Dixon, D.

- A.; Liu, S.-Y. *Angew. Chem. Int. Ed.* **2013**, *52*, 7527–7531.
- [12] (a) Lee, H.; Fischer, M.; Shoichet, B. K.; Liu, S.-Y. *J. Am. Chem. Soc.* **2016**, *138*, 12021–12024. (b) Liu, Y.; Liu, S.-Y. *Org. Biomol. Chem.* **2019**, *17*, 7002–7006.
- [13] (a) Koezuka, H.; Tsumura, A.; Ando, T. *Synthetic Metals.* **1987**, *18*, 699–704. (b) Muccini, M. *Nat. Mater.* **2006**, *5*, 605–613. (c) Siringhaus, H. *Adv. Mater.* **2014**, *26*, 1319–1335.
- [14] (a) Tang, C.; VanSlyke, S. *Appl. Phys. Lett.* **1987**, *51*, 913–915. (b) Dias, F. B.; Bourdakos, K. N.; Jankus, V.; Moss, K. C.; Kamtekar, K. T.; Bhalla, V.; Santos, J.; Bryce, M. R.; Monkman, A. P. *Adv. Mater.* **2013**, *25*, 3707–3714. (c) Salehi, A.; Fu, X.; Shin, D.; So, F. *Adv. Funct. Mater.* **2019**, *29*, 1808803.
- [15] (a) Smith, M. B.; Michl, J. *Chem. Rev.* **2010**, *110*, 6891–6936. (b) Johnson, J.; Nozik, A.; Michl, J. *J. Am. Chem. Soc.* **2010**, *132*, 16302–16303. (c) Hetzer, C.; Basel, B. S.; Kopp, S. M.; Hampel, F.; White, F. J.; Clark, T.; Guldi, D. M.; Tykwinski, R. R. *Angew. Chem.* **2019**, *131*, 15407–15411.
- [16] (a) Wang, X.-Y.; Zhuang, F.-D.; Wang, R.-B.; Wang, X.-C.; Cao, X.-Y.; Wang, J.-Y.; Pei, J. *J. Am. Chem. Soc.* **2014**, *136*, 3764–3767. (b) Wang, X.-Y.; Lin, H.-R.; Lei, T.; Yang, D.-C.; Zhuang, F.-D.; Wang, J.-Y.; Yuan, S.-C.; Pei, J. *Angew. Chem. Int. Ed.* **2013**, *52*, 3117–3120. (c) Wang, X.-Y.; Zhuang, F.-D.; Wang, J.-Y.; Pei, J. *Chem. Commun.* **2015**, *51*, 17532–17535. (d) Zhuang, F.; Sun, Z.; Yao, Z.; Chen, Q.; Huang, Z.; Yang, J.; Wang, J.; Pei, J. *Angew. Chem. Int. Ed.* **2019**, *58*, 10708–10712.
- [17] Zhao, K.; Yao, Z.-F.; Wang, Z.-Y.; Zeng, J.-C.; Ding, L.; Xiong, M.; Wang, J.-Y.; Pei, J. *J. Am. Chem. Soc.* **2022**, *144*, 3091–3098.
- [18] Li, W.; Du, C.; Chen, X.; Fu, L.; Gao, R.; Yao, Z.; Wang, J.; Hu, W.; Pei, J.; Wang, X. *Angew. Chem. Int. Ed.* **2022**, *134*, 1–6.
- [19] Lepeltier, M.; Lukyanova, O.; Jacobson, A.; Jeeva, S.; Perepichka, D. F. *Chem. Commun.* **2010**, *46*, 7007.
- [20] Wang, X.; Zhang, F.; Liu, J.; Tang, R.; Fu, Y.; Wu, D.; Xu, Q.; Zhuang, X.; He, G.; Feng, X. *Org. Lett.* **2013**, *15*, 5714–5717.
- [21] Li, G.; Xiong, W.-W.; Gu, P.-Y.; Cao, J.; Zhu, J.; Ganguly, R.; Li, Y.; Grimsdale,

- A. C.; Zhang, Q. *Org. Lett.* **2015**, *17*, 560–563.
- [22] Hashimoto, S.; Ikuta, T.; Shiren, K.; Nakatsuka, S.; Ni, J.; Nakamura, M.; Hatakeyama, T. *Chem. Mater.* **2014**, *26*, 6265–6271.
- [23] Li, G.; Zhao, Y.; Li, J.; Cao, J.; Zhu, J.; Sun, X. W.; Zhang, Q. *J. Org. Chem.* **2015**, *80*, 196–203.
- [24] Wang, R.; Lee, C.-S.; Lu, Z. *J. Organomet. Chem.* **2023**, *984*, 122564.
- [25] Hatakeyama, T.; Shiren, K.; Nakajima, K.; Nomura, S.; Nakatsuka, S.; Kinoshita, K.; Ni, J.; Ono, Y.; Ikuta, T. *Adv. Mater.* **2016**, *28*, 2777–2781.
- [26] Kondo, Y.; Yoshiura, K.; Kitera, S.; Nishi, H.; Oda, S.; Gotoh, H.; Sasada, Y.; Yanai, M.; Hatakeyama, T. *Nat. Photonics* **2019**, *13*, 678–682.
- [27] Zhang, Y.; Zhang, D.; Wei, J.; Liu, Z.; Lu, Y.; Duan, L. *Angew. Chem. Int. Ed.* **2019**, *58*, 16912–16917.
- [28] Cai, X.; Xu, Y.; Pan, Y.; Li, L.; Pu, Y.; Zhuang, X.; Li, C.; Wang, Y. *Angew. Chem. Int. Ed.* **2023**, *62*.
- [29] Akdag, A.; Havlas, Z.; Michl, J. *J. Am. Chem. Soc.* **2012**, *134*, 14624–14631.
- [30] Zeng, T.; Møllerup, S. K.; Yang, D.; Wang, X.; Wang, S.; Stamplecoskie, K. *J. Phys. Chem. Lett.* **2018**, *9*, 2919–2927.
- [31] Dewar, M. J. S.; Dietz, R. *J. Chem. Soc.* **1959**, 2728–2730.
- [32] (a) Ishibashi, J. S. A.; Marshall, J. L.; Mazière, A.; Lovinger, G. J.; Li, B.; Zakharov, L. N.; Dargelos, A.; Graciaa, A.; Chrostowska, A.; Liu, S.-Y. *J. Am. Chem. Soc.* **2014**, *136*, 15414–15421. (b) Zhang, C.; Zhang, L.; Sun, C.; Sun, W.; Liu, X. *Org. Lett.* **2019**, *21*, 3476–3480. (c) Abengózar, A.; García-García, P.; Sucunza, D.; Sampedro, D.; Pérez-Redondo, A.; Vaquero, J. *J. Org. Lett.* **2019**, *21*, 2550–2554. (d) Li, E.; Jin, M.; Jiang, R.; Zhang, L.; Zhang, Y.; Liu, M.; Wu, X.; Liu, X. *Org. Lett.* **2022**, *24*, 5503–5508. (e) Ishibashi, J. S. A.; Dargelos, A.; Darrigan, C.; Chrostowska, A.; Liu, S.-Y. *Organometallics* **2017**, *36*, 2494–2497. (f) Wang, X.; Zhang, F.; Gao, J.; Fu, Y.; Zhao, W.; Tang, R.; Zhang, W.; Zhuang, X.; Feng, X. *J. Org. Chem.* **2015**, *80*, 10127–10133. (g) Zhang, W.; Zhang, F.; Tang, R.; Fu, Y.; Wang, X.; Zhuang, X.; He, G.; Feng, X. *Org. Lett.* **2016**, *18*, 3618–3621. (h) Jiang, Z.; Zhou, S.; Jin, W.; Zhao, C.; Liu, Z.; Yu, X. *Org. Lett.*

- 2022**, *24*, 1017–1021.
- [33] Wisniewski, S. R.; Guenther, C. L.; Argintaru, O. A.; Molander, G. A. *J. Org. Chem.* **2014**, *79*, 365–378.
- [34] (a) Abengózar, A.; García-García, P.; Sucunza, D.; Frutos, L. M.; Castaño, O.; Sampedro, D.; Pérez-Redondo, A.; Vaquero, J. J. *Org. Lett.* **2017**, *19*, 3458–3461.
(b) Abengózar, A.; García-García, P.; Sucunza, D.; Pérez-Redondo, A.; Vaquero, J. J. *Chem. Commun.* **2018**, *54*, 2467–2470. (c) Abengózar, A.; Valencia, I.; Otárola, G. G.; Sucunza, D.; García-García, P.; Pérez-Redondo, A.; Mendicuti, F.; Vaquero, J. J. *Chem. Commun.* **2020**, *56*, 3669–3672.
- [35] Tian, D.; Shi, G.; Fan, M.; Guo, X.; Yuan, Y.; Wu, S.; Liu, J.; Zhang, J.; Xing, S.; Zhu, B. *Org. Lett.* **2021**, *23*, 8163–8168.
- [36] Zhang, P.-F.; Zhuang, F.-D.; Sun, Z.-H.; Lu, Y.; Wang, J.-Y.; Pei, J. *J. Org. Chem.* **2020**, *85*, 241–247.
- [37] (a) Paetzold, P. I.; Stohr, G.; Maisch, H.; Lenz, H. *Chem. Ber.* **1968**, *101*, 2881.
(b) Paetzold, P.; Stanescu, C.; Stubenrauch, J. R.; Bienmuller, M.; Englert, U. *Z. Anorg. Allg. Chem.* **2004**, *630*, 2632.
- [38] Zhuang, F.-D.; Han, J.-M.; Tang, S.; Yang, J.-H.; Chen, Q.-R.; Wang, J.-Y.; Pei, J. *Organometallics* **2017**, *36*, 2479–2482.
- [39] Pati, P. B.; Jin, E.; Kim, Y.; Kim, Y.; Mun, J.; Kim, S. J.; Kang, S. J.; Choe, W.; Lee, G.; Shin, H.; Park, Y. S. *Angew. Chem. Int. Ed.* **2020**, *59*, 14891–14895.
- [40] Tsuchiya, S.; Saito, H.; Nogi, K.; Yorimitsu, H. *Org. Lett.* **2019**, *21*, 3855–3860.
- [41] Dewar, M. J. S.; Jones, R. *J. Am. Chem. Soc.* **1968**, *90*, 2137–2144.
- [42] Dewar, M. J. S.; Kaneko, C.; Bhattacharjee, M. K. *J. Am. Chem. Soc.* **1962**, *84*, 4884–4887.
- [43] Fang, X.; Yang, H.; Kampf, J. W.; Banaszak Holl, M. M.; Ashe, A. J. *Organometallics* **2006**, *25*, 513–518.
- [44] Rohr, A. D.; Kampf, J. W.; Ashe, A. J. *Organometallics* **2014**, *33*, 1318–1321.
- [45] Sun, F.; Lv, L.; Huang, M.; Zhou, Z.; Fang, X. *Org. Lett.* **2014**, *16*, 5024–5027.
- [46] Zhang, P.; Zeng, J.; Zhuang, F.; Zhao, K.; Sun, Z.; Yao, Z.; Lu, Y.; Wang, X.; Wang, J.; Pei, J. *Angew. Chem. Int. Ed.* **2021**, *60*, 23313–23319.

- [47] Liu, X.; Wu, P.; Li, J.; Cui, C. *J. Org. Chem.* **2015**, *80*, 3737–3744.
- [48] Dewar, M. J. S.; Kaneko, Chikara.; Bhattacharjee, M. K. *J. Am. Chem. Soc.* **1962**, *84*, 4884–4887.
- [49] Ishibashi, J. S. A.; Darrigan, C.; Chrostowska, A.; Li, B.; Liu, S.-Y. *Dalton Trans.* **2019**, *48*, 2807–2812.
- [50] Kaehler, T.; Bolte, M.; Lerner, H.; Wagner, M. *Angew. Chem. Int. Ed.* **2019**, *58*, 11379–11384.
- [51] Brown, A. N.; Li, B.; Liu, S.-Y. *J. Am. Chem. Soc.* **2015**, *137*, 8932–8935.
- [52] Valencia, I.; García-García, P.; Sucunza, D.; Mendicuti, F.; Vaquero, J. J. *J. Org. Chem.* **2021**, *86*, 16259–16267.
- [53] Appiarius, Y.; Stauch, T.; Lork, E.; Rusch, P.; Bigall, N. C.; Staubitz, A. *Org. Chem. Front.* **2021**, *8*, 10–17.
- [54] Liu, Z.; Ishibashi, J. S. A.; Darrigan, C.; Dargelos, A.; Chrostowska, A.; Li, B.; Vasiliu, M.; Dixon, D. A.; Liu, S.-Y. *J. Am. Chem. Soc.* **2017**, *139*, 6082–6085.
- [55] Bosdet, M. J. D.; Jaska, C. A.; Piers, W. E.; Sorensen, T. S.; Parvez, M. *Org. Lett.* **2007**, *9*, 1395–1398.
- [56] (a) Bosdet, M. J. D.; Piers, W. E.; Sorensen, T. S.; Parvez, M. *Angew. Chem. Int. Ed.* **2007**, *46*, 4940–4943. (b) Jaska, C. A.; Emslie, D. J. H.; Bosdet, M. J. D.; Piers, W. E.; Sorensen, T. S.; Parvez, M. *J. Am. Chem. Soc.* **2006**, *128*, 10885–10896. (c) Neue, B.; Araneda, J. F.; Piers, W. E.; Parvez, M. *Angew. Chem. Int. Ed.* **2013**, *52*, 9966–9969.
- [57] (a) Lu, J.-S.; Ko, S.-B.; Walters, N. R.; Kang, Y.; Sauriol, F.; Wang, S. *Angew. Chem.* **2013**, *125*, 4642–4646. (b) Wang, S.; Yang, D.-T.; Lu, J.; Shimogawa, H.; Gong, S.; Wang, X.; Møllerup, S. K.; Wakamiya, A.; Chang, Y.-L.; Yang, C.; Lu, Z.-H. *Angew. Chem. Int. Ed.* **2015**, *54*, 15074–15078.
- [58] Yang, D.-T.; Møllerup, S. K.; Wang, X.; Lu, J.-S.; Wang, S. *Angew. Chem. Int. Ed.* **2015**, *54*, 5498–5501.
- [59] Biswas, S.; Maichle-Mössmer, C.; Bettinger, H. F. *Chem. Commun.* **2012**, *48*, 4564.
- [60] Müller, M.; Maichle-Mössmer, C.; Bettinger, H. F. *Angew. Chem. Int. Ed.* **2014**,

53, 9380–9383.

- [61] Braunschweig, H.; Hörl, C.; Mailänder, L.; Radacki, K.; Wahler, J. *Chem. - Eur. J.* **2014**, *20*, 9858–9861.
- [62] Yruegas, S.; Martinez, J. J.; Martin, C. D. *Chem. Commun.* **2018**, *54*, 6808–6811.
- [63] Turner, D.; Baker, C.; Baker, A.; Brundle, C. *Molecular Photoelectron Spectroscopy.* **1970**.
- [64] Lemierre, V.; Chrostowska, A.; Dargelos, A.; Chermette, H. *J. Phys. Chem. A* **2005**, *109*, 8348–8355.
- [65] Chrostowska, A.; Xu, S.; Maziere, A.; Boknevitiz, K.; Li, B.; Abbey, E.; Dargelos, A.; Graciaa, A.; Liu, S-Y. *J. Am. Chem. Soc.* **2014**, *136*, 11813–11820.
- [66] Olmsted, J. *J. Phys. Chem.* **1979**, *83*, 2581–2584.
- [67] Wang, X.; Narita, A.; Feng, X.; Müllen, K. *J. Am. Chem. Soc.* **2015**, *137*, 7668–7671.
- [68] Gaussian 09, Revision D.01, Frisch, M. J.; Trucks, G. W.; Schlegel, H. B.; Scuseria, G. E.; Robb, M. A.; Cheeseman, J. R.; Scalmani, G.; Barone, V.; Mennucci, B.; Petersson, G. A.; Nakatsuji, H.; Caricato, M.; Li, X.; Hratchian, H. P.; Izmaylov, A. F.; Bloino, J.; Zheng, G.; Sonnenberg, J. L.; Hada, M.; Ehara, M.; Toyota, K.; Fukuda, R.; Hasegawa, J.; Ishida, M.; Nakajima, T.; Honda, Y.; Kitao, O.; Nakai, H.; Vreven, T.; Montgomery, J. A., Jr.; Peralta, J. E.; Ogliaro, F.; Bearpark, M.; Heyd, J. J.; Brothers, E.; Kudin, K. N.; Staroverov, V. N.; Kobayashi, R.; Normand, J.; Raghavachari, K.; Rendell, A.; Burant, J. C.; Iyengar, S. S.; Tomasi, J.; Cossi, M.; Rega, N.; Millam, J. M.; Klene, M.; Knox, J. E.; Cross, J. B.; Bakken, V.; Adamo, C.; Jaramillo, J.; Gomperts, R.; Stratmann, R. E.; Yazyev, O.; Austin, A. J.; Cammi, R.; Pomelli, C.; Ochterski, J. W.; Martin, R. L.; Morokuma, K.; Zakrzewski, V. G.; Voth, G. A.; Salvador, P.; Dannenberg, J. J.; Dapprich, S.; Daniels, A. D.; Farkas, Ö.; Foresman, J. B.; Ortiz, J. V.; Cioslowski, J.; Fox, D. J. Gaussian, Inc., Wallingford CT, 2009.

Chapter 2. Electronic Structure Calculations of BN-doped Phenanthrene Isomers

2.1 Introduction

The preceding chapter elucidated the use of BN/CC isosterism as a technique to modify the electronic structure of polycyclic aromatic hydrocarbons (PAHs) while preserving their geometries. Additionally, the first chapter discussed selected synthetic methods for creating BN-doped PAHs. However, there are still knowledge gaps in understanding of the effects of BN/CC isosterism on the properties and structures of PAHs. To discern the origins of these distinctions, a direct comparison between BN-doped molecules and their all-carbon counterparts is necessary. For instance, Dewar synthesized the first BN-doped compound, BN-9,10-phenanthrene, and contrasted its photophysical properties with all-carbon phenanthrene via UV spectroscopy in 1958.¹ The results showed a slight blue shift (25 nm) in the maximum absorption wavelength of BN-9,10-phenanthrene when compared to its all-carbon analogue. Piers demonstrated a direct comparison between BN-4a,4b-phenanthrene, BN-9,10-phenanthrene and all-carbon phenanthrene using fluorescent emission spectroscopy to reveal the BN doping effects on photophysical properties.² As shown in Figure 2.1a, these isosteres exhibited markedly different fluorescent emission properties. Specifically, the maximum fluorescence emission wavelengths of phenanthrene, BN-9,10-phenanthrene, and BN-4a,4b-phenanthrene were 347 nm, 327 nm, and 450 nm, respectively. BN-4a,4b-phenanthrene displayed a large red shift (103 nm) relative to all-carbon phenanthrene, whereas BN-9,10-phenanthrene exhibited a small blue shift (20 nm) relative to all-carbon phenanthrene. From the shape of the spectra, it is seen that BN-9,10-phenanthrene and phenanthrene display high similarity in their emission spectra. On the other hand, the spectrum of BN-4a,4b-phenanthrene is characterized by the absence of two transition peaks with respect to pure phenanthrene. Furthermore, Liu demonstrated a direct comparison between BN-1,2-phenanthrene, BN-4,3-phenanthrene and all-carbon phenanthrene by characterization of fluorescent emission spectroscopy.³ As shown in Figure 2.1b, BN-4,3-phenanthrene displayed a small red

shift (6 nm), whereas BN-1,2-phenanthrene had a nearly identical emission spectrum with all-carbon phenanthrene. These four phenanthrene isomers displayed distinct photophysical properties because of the positions of the BN bond.

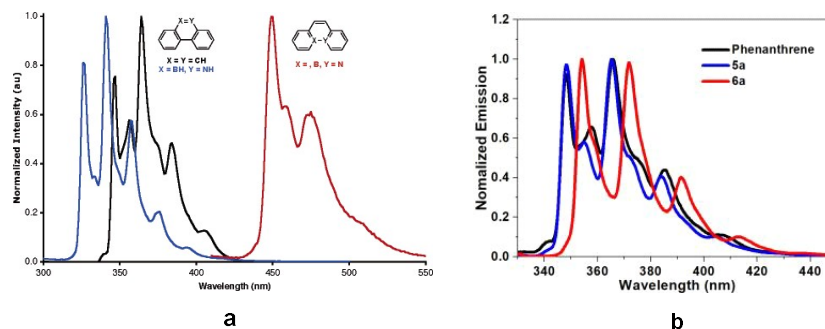


Figure 2.1. (a) Normalized fluorescence emission spectra of phenanthrene (black line), BN-4a,4b-phenanthrene (red line), and BN-9,10-phenanthrene (blue line) in cyclohexane. (b) Normalized fluorescence emission spectra of phenanthrene (black line), BN-1,2-phenanthrene (5a, blue line), and BN-4,3-phenanthrene (6a, red line) in cyclohexane.

Property differences resulting from BN/CC isosterism are not limited to phenanthrene but are also commonly observed in other PAHs. For instance, Liu conducted an experimental investigation of BN-naphthalene isosteres and found that BN-1,9-naphthalene and BN-9,1-naphthalene displayed significant red-shifted emissions, while BN-1,2-naphthalene and BN-9,10-naphthalene exhibited slight blue-shifted emissions.⁴

Understanding the influence of BN bond positioning on the properties and structure of PAHs is critical. However, to the best of our knowledge, the simplest structures of PAHs, such as naphthalene, phenanthrene and anthracene, have less than half of their BN isosteres identified experimentally.⁵ Experimental exploration of the impact of BN positioning is difficult owing to the challenge of synthesizing and characterizing a full series of BN-doped PAHs. Therefore, using theoretical computations is strongly recommended to overcome this challenge.

The relationship between the position of the BN bond and the molecular properties of PAHs has not been well studied in recent years. Our group explored theoretically the

relationship between the positioning of a BN bond in acene scaffolds (naphthalene, anthracene and tetracene) and the energy of the molecular frontier orbitals (HOMO and LUMO) in 2017.⁶ We provided an empirical guideline to predict frontier orbital energetics based on the position of the BN bond and a carbonaceous reference, which could be useful in the further targeted syntheses of BN acenes for potential applications. Stojanović^a and Baranac-Stojanović⁷ reported a systematic study of all mono-boron- and mono-nitrogen-doped naphthalene isosteres using theoretical calculations to comprehend the effect of the position of the boron atom and nitrogen atom in a molecule on relative stability, aromaticity, and frontier orbital energies. The results displayed an evident relationship between the position of the BN unit and molecular stability, aromaticity, and frontier orbital energies of the doped system.

In this chapter, we conducted a comprehensive analysis of the impact of BN doping on the structure-property correlations of PAHs using appropriate theoretical calculations that take into account bond length, bond order, aromaticity, dipole moment, frontier orbitals and excited states. Our focus was solely on BN/CC bond replacement, and we did not explore isomers with separated boron and nitrogen atoms in their structure. Among all the small-sized PAH candidates, we chose phenanthrene, the simplest structural unit of the [n]phenacene series (Figure 2.2 a). The latter molecule has been used as a representative molecular scaffold to investigate the effects of single BN bond doping as a function of the doping site and orientations of the BN bond. The main objective of this study was to identify the fundamental trends in the BN-doped phenanthrene series and extend them to other arenes and multi-BN doped systems. The molecular structures of all sixteen BN phenanthrene isosteres, are depicted in Figure 2.2 c. We adopted the IUPAC nomenclature of phenanthrene (Figure 2.2 b) to name the sixteen BN phenanthrene isosteres.

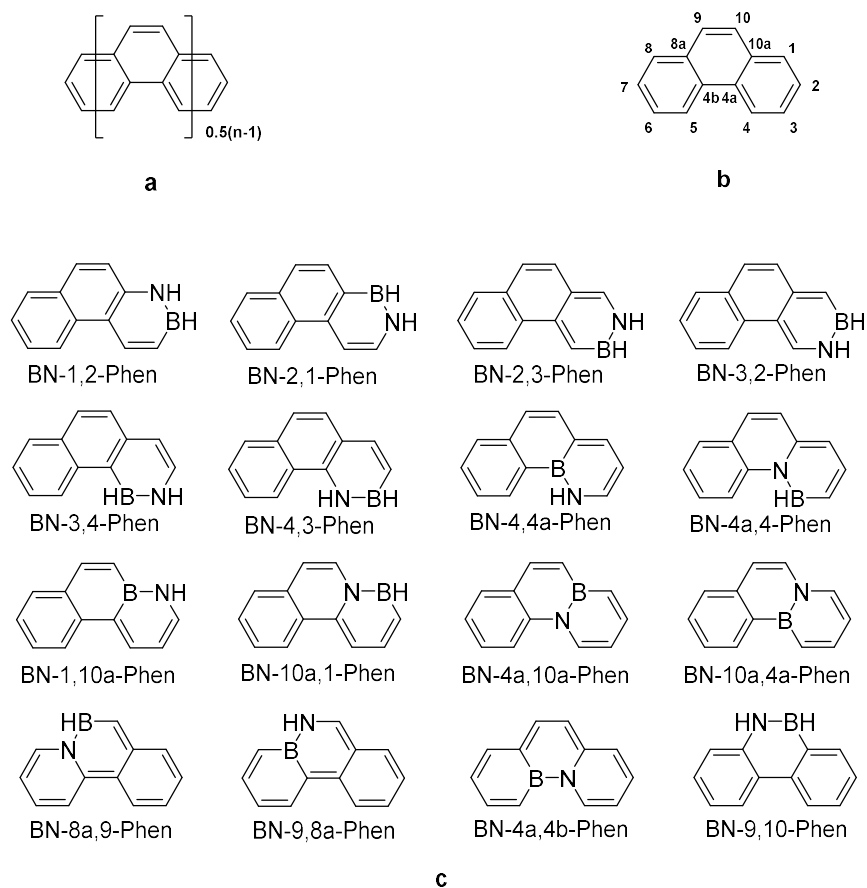


Figure 2.2. (a) Molecular structure of $[n]$ phenacene. (b) The numbering of positions according to IUPAC nomenclature. (c) The nomenclature of sixteen BN phenanthrene isosteres.

2.2 Computational details

The methods used in this chapter comprise conventional functional theory (DFT), time-dependent density functional theory (TD-DFT) methods, the coupled-cluster singles doubles (CCSD) method⁸, and the equation-of-motion coupled-cluster (EOM-CCSD) theory.⁹ These computations have been carried out with the Gaussian 16 (C.01)¹⁰ suite of programs. We also performed complete active space self-consistent field (CASSCF)¹¹ calculations to examine the robustness were of the obtained trends. These computation have been performed with the Molpro (2019.2)¹² package.

The ground state geometries of phenanthrene and its sixteen BN analogues were optimized in the gas phases with seven different methods involving B3LYP¹³, PBE0¹⁴,

CAM-B3LYP¹⁵, wB97XD¹⁶, M06-2X¹⁷, CCSD, and CASSCF. The 6-311G(d,p)¹⁸ basis set was used for the five hybrid functional methods. The correlation consistent cc-pVDZ¹⁹ basis set was used for the CCSD method, while CASSCF computations have been performed with the def2-SVPD²⁰ basis set. To ensure that the structures were the real minima, vibrational frequencies in DFT and CCSD calculations have been carried in each case apart from computation at the CCSD EOM-CCSD and CASSCF levels of theory due to the high cost of computational resources required. For the CASSCF calculations we included in the active space all occupied π orbitals (CASSCF(14,14)). The optimized geometries were used as starting points for other calculations. The vertical excitation energies from the ground state (S_0) to the first singlet excited state (S_1) and the first triplet excited state (T_1) were calculated with TD-DFT, EOM-CCSD or CASSCF methods on the optimized ground state geometries obtained at the same level of theory. The adiabatic excitation energies from S_0 to S_1 and T_1 were calculated by optimizing the geometries of S_1 and T_1 excited states within the TD-DFT, EOM-CCSD and CASSCF approximations. The aromaticity was determined by nucleus-independent chemical shift (NICS)²¹ calculations at the approximate centre of the six-member rings and at 1 Å above the ring on the axis perpendicular to the ring and passing through the approximate centre of the ring. The Mayer bond orders²², electron localization function (ELF)²³ analysis of π molecular orbitals were carried out using the Multiwfn 3.8 (dev)²⁴ program based on the DFT or TD-DFT calculated output files.

2.3 Results and discussion

2.3.1 Bond lengths

The substitution of BN/CC in PAHs leads to slight changes in molecular bond lengths. These changes between PAHs and their BN analogues are mostly manifested in the C-N-B-C fragments, while for the rest of fragments they have proven negligible. Our calculation indicated that the effect of BN doping on the phenanthrene skeleton depends on the location of the BN bond within the structure of the final isostere. Herein, we performed the calculated bond lengths of phenanthrene and its sixteen BN analogues

using three different theoretical methods, including DFT (B3LYP/6-311G(d,p), Table 2.1), coupled-cluster (CCSD/cc-pVDZ, Table 2.2), and MCSCF (CASSCF(14,14)/def2-svpd, Table 2.3). Among the three methods, the CCSD method has been used as a criterion. From Table 2.2, all BN bonds, ranging from 1.414 Å to 1.492 Å, are longer than the corresponding CC bonds. BN-9,10-phenanthrene has the shortest BN bond and BN-4a,4b-phenanthrene has the longest BN bond. We analyze the similarities between phenanthrene and its BN analogues on bond lengths using a pattern recognition technique based on the Euclidean distances between vectors, the components of which are the bond lengths of each molecule.²⁵ From Table 2.4, we find that the similarity of geometries optimized by the three different methods is slightly different, but the trend remains the same. Except for BN-8a,9-Phen, BN-9,8a-Phen, and BN-4a,4b-Phen isomers, which are less similar to phenanthrene, the similarity of the rest of the isomers is close, ranging from 50% to 70%.

Table 2.1 Bond lengths (Å) of phenanthrene and BN-phenanthrene isosteres have been calculated at B3LYP/6-311G(d,p) level.

	1-2	2-3	3-4	4-4a	4a-10a	4a-4b	4b-5	5-6	6-7	7-8	8-8a	4b-8a	8a-9	9-10	10-10a	1-10a
Phen	1.378	1.405	1.380	1.413	1.425	1.457	1.413	1.380	1.405	1.378	1.413	1.425	1.434	1.356	1.434	1.413
BN-12	1.425	1.517	1.366	1.437	1.407	1.448	1.417	1.378	1.408	1.375	1.415	1.428	1.425	1.362	1.423	1.379
BN-21	1.423	1.374	1.358	1.437	1.415	1.450	1.417	1.377	1.408	1.375	1.416	1.429	1.426	1.363	1.427	1.525
BN-23	1.351	1.442	1.497	1.391	1.449	1.473	1.408	1.384	1.401	1.381	1.409	1.422	1.442	1.350	1.440	1.382
BN-32	1.495	1.443	1.354	1.382	1.450	1.467	1.409	1.384	1.401	1.381	1.408	1.420	1.442	1.351	1.446	1.392
BN-34	1.355	1.375	1.425	1.529	1.414	1.446	1.418	1.377	1.409	1.376	1.415	1.428	1.427	1.362	1.430	1.437
BN-43	1.364	1.518	1.427	1.377	1.406	1.442	1.417	1.377	1.408	1.375	1.416	1.428	1.426	1.362	1.427	1.436
BN-44a	1.412	1.374	1.360	1.441	1.524	1.542	1.407	1.386	1.401	1.384	1.410	1.427	1.452	1.359	1.440	1.387
BN-4a4	1.402	1.378	1.495	1.467	1.401	1.430	1.404	1.386	1.398	1.380	1.408	1.417	1.436	1.347	1.436	1.387
BN-4a10a	1.365	1.424	1.361	1.382	1.473	1.419	1.407	1.385	1.398	1.380	1.410	1.422	1.443	1.352	1.525	1.518
BN-10a4a	1.360	1.426	1.369	1.517	1.468	1.543	1.409	1.385	1.403	1.383	1.410	1.421	1.443	1.349	1.395	1.379
BN-8a9	1.367	1.416	1.371	1.425	1.441	1.432	1.421	1.368	1.414	1.359	1.380	1.394	1.483	1.465	1.408	1.430
BN-98a	1.367	1.419	1.371	1.426	1.443	1.429	1.422	1.377	1.426	1.374	1.511	1.520	1.460	1.332	1.403	1.426
BN-110a	1.357	1.373	1.413	1.387	1.527	1.462	1.409	1.384	1.400	1.383	1.409	1.427	1.454	1.357	1.526	1.443
BN-10a1	1.491	1.380	1.406	1.386	1.398	1.466	1.409	1.383	1.401	1.381	1.407	1.417	1.438	1.343	1.396	1.464
BN-4a4b	1.365	1.418	1.360	1.378	1.394	1.491	1.513	1.377	1.427	1.373	1.422	1.516	1.405	1.382	1.408	1.423
BN-910	1.384	1.400	1.385	1.410	1.421	1.472	1.409	1.384	1.398	1.383	1.404	1.418	1.393	1.409	1.534	1.408

Table 2.2 Bond lengths (Å) of phenanthrene and BN-phenanthrene isosteres have been calculated at CCSD/cc-pVDZ level.

	1-2	2-3	3-4	4-4a	4a-10a	4a-4b	4b-5	5-6	6-7	7-8	8-8a	4b-8a	8a-9	9-10	10-10a	1-10a
Phen	1.389	1.419	1.391	1.426	1.424	1.470	1.426	1.391	1.419	1.389	1.425	1.424	1.451	1.366	1.451	1.425
BN-12	1.428	1.538	1.375	1.454	1.407	1.459	1.432	1.388	1.423	1.385	1.429	1.428	1.440	1.372	1.438	1.388
BN-21	1.426	1.385	1.367	1.454	1.414	1.461	1.431	1.387	1.423	1.385	1.430	1.428	1.442	1.373	1.443	1.544
BN-23	1.364	1.443	1.519	1.396	1.456	1.489	1.419	1.396	1.413	1.394	1.419	1.423	1.462	1.359	1.460	1.387
BN-32	1.517	1.444	1.366	1.387	1.456	1.482	1.420	1.396	1.413	1.394	1.418	1.421	1.462	1.360	1.466	1.396
BN-34	1.365	1.385	1.428	1.548	1.414	1.459	1.432	1.387	1.424	1.386	1.428	1.427	1.442	1.372	1.445	1.452
BN-43	1.374	1.539	1.430	1.388	1.406	1.454	1.431	1.387	1.423	1.385	1.429	1.428	1.441	1.372	1.441	1.452
BN-44a	1.432	1.380	1.373	1.440	1.535	1.561	1.418	1.398	1.412	1.397	1.419	1.428	1.474	1.366	1.461	1.390
BN-4a4	1.422	1.385	1.517	1.468	1.404	1.441	1.416	1.397	1.410	1.393	1.417	1.418	1.456	1.355	1.458	1.390
BN-4a10a	1.374	1.443	1.369	1.395	1.467	1.427	1.420	1.396	1.410	1.392	1.420	1.424	1.460	1.362	1.546	1.538
BN-10a4a	1.368	1.444	1.377	1.538	1.462	1.558	1.421	1.396	1.416	1.394	1.420	1.423	1.460	1.359	1.406	1.390
BN-8a9	1.375	1.436	1.377	1.444	1.442	1.435	1.443	1.374	1.433	1.367	1.394	1.389	1.490	1.482	1.416	1.448
BN-98a	1.374	1.439	1.377	1.447	1.445	1.430	1.444	1.382	1.448	1.381	1.533	1.525	1.464	1.341	1.410	1.444
BN-110a	1.370	1.379	1.432	1.392	1.538	1.480	1.419	1.397	1.412	1.395	1.419	1.427	1.474	1.366	1.550	1.442
BN-10a1	1.514	1.386	1.425	1.390	1.401	1.484	1.420	1.396	1.413	1.394	1.417	1.418	1.457	1.352	1.411	1.463
BN-4a4b	1.371	1.438	1.367	1.394	1.389	1.492	1.536	1.383	1.448	1.379	1.442	1.521	1.411	1.398	1.414	1.414
BN-910	1.395	1.413	1.396	1.421	1.424	1.485	1.420	1.396	1.411	1.394	1.415	1.421	1.402	1.414	1.553	1.420

Table 2.3 Bond lengths (Å) of phenanthrene and BN-phenanthrene isosteres have been calculated at CASSCF(14,14)/def2-SVP level.

	1-2	2-3	3-4	4-4a	4a-10a	4a-4b	4b-5	5-6	6-7	7-8	8-8a	4b-8a	8a-9	9-10	10-10a	1-10a
Phen	1.379	1.413	1.381	1.421	1.413	1.453	1.421	1.381	1.413	1.379	1.420	1.413	1.438	1.360	1.438	1.420
BN-12	1.412	1.541	1.365	1.454	1.396	1.453	1.427	1.380	1.417	1.377	1.424	1.421	1.432	1.366	1.429	1.388
BN-21	1.410	1.384	1.355	1.455	1.404	1.453	1.428	1.380	1.417	1.378	1.425	1.421	1.433	1.368	1.434	1.549
BN-23	1.369	1.418	1.529	1.382	1.456	1.487	1.413	1.392	1.404	1.390	1.412	1.416	1.459	1.350	1.459	1.371
BN-32	1.525	1.420	1.369	1.373	1.456	1.482	1.414	1.391	1.404	1.389	1.412	1.414	1.459	1.351	1.462	1.383
BN-34	1.353	1.383	1.413	1.555	1.403	1.452	1.427	1.381	1.417	1.379	1.424	1.421	1.433	1.366	1.436	1.452
BN-43	1.363	1.542	1.414	1.388	1.395	1.445	1.427	1.380	1.417	1.378	1.424	1.421	1.433	1.366	1.434	1.452
BN-44a	1.435	1.363	1.377	1.420	1.542	1.569	1.411	1.394	1.404	1.393	1.412	1.421	1.472	1.357	1.460	1.376
BN-4a4	1.432	1.359	1.534	1.430	1.408	1.449	1.410	1.400	1.401	1.395	1.412	1.413	1.455	1.343	1.463	1.365
BN-4a10a	1.364	1.440	1.358	1.392	1.446	1.420	1.413	1.391	1.402	1.387	1.414	1.417	1.455	1.354	1.547	1.543
BN-10a4a	1.358	1.441	1.367	1.543	1.441	1.562	1.416	1.391	1.408	1.389	1.414	1.415	1.455	1.350	1.400	1.386
BN-8a9	1.364	1.434	1.367	1.446	1.435	1.422	1.442	1.364	1.432	1.356	1.392	1.381	1.462	1.487	1.403	1.447
BN-98a	1.362	1.439	1.366	1.449	1.443	1.414	1.443	1.375	1.446	1.371	1.544	1.530	1.431	1.350	1.392	1.447
BN-110a	1.372	1.363	1.435	1.378	1.545	1.479	1.412	1.392	1.403	1.392	1.411	1.421	1.473	1.357	1.553	1.423
BN-10a1	1.523	1.369	1.428	1.374	1.400	1.483	1.413	1.393	1.404	1.391	1.410	1.411	1.455	1.342	1.409	1.435
BN-4a4b	1.361	1.437	1.356	1.392	1.382	1.466	1.545	1.372	1.447	1.369	1.441	1.524	1.398	1.397	1.399	1.443
BN-910	1.389	1.404	1.390	1.415	1.416	1.482	1.415	1.390	1.403	1.388	1.407	1.412	1.398	1.400	1.554	1.413

Table 2.4 The similarities between phenanthrene and BN-phenanthrene isosteres in bond lengths.

	B3LYP	CCSD	CASSCF
BN-12	58.1%	62.5%	68.5%
BN-21	58.4%	62.3%	68.6%
BN-23	55.5%	57.7%	56.1%
BN-32	55.8%	57.7%	56.2%
BN-34	58.5%	62.3%	67.5%
BN-43	57.2%	62.0%	68.5%
BN-44a	46.1%	49.0%	44.8%
BN-4a4	52.1%	56.0%	49.8%
BN-4a10a	46.7%	51.8%	55.2%
BN-10a4a	47.5%	53.0%	54.7%
BN-8a9	31.3%	35.6%	45.8%
BN-98a	36.8%	37.1%	41.9%
BN-110a	47.0%	49.6%	45.7%
BN-10a1	54.4%	56.4%	55.1%
BN-4a4b	30.3%	31.9%	36.0%
BN-910	53.7%	57.3%	58.8%

To further understand the partial changes caused by BN doping, a statistical analysis of the differences between the corresponding bond lengths was performed in Table 2.5. A threshold of 0.015 Å was set to indicate a significant difference, and the bond lengths with absolute differences greater than the threshold were marked in red (Table 2.5) and bolded (Figure 2.3). It should be noted that the choice of threshold is arbitrary and intended to highlight partial changes. Furthermore, Clar's aromatic π -sextet rule²⁶, which is widely accepted in theoretical and experimental chemistry, was applied to represent the structure of phenanthrene. According to this representation, CC bonds of phenanthrene can be divided into single, double and multicenter bonds (aromatic rings). From Figure 2.3, twelve BN-phenanthrene analogues which BN bonds located in the aromatic rings exhibit significant differences, three BN-phenanthrene analogues (BN-4a,4b-phenanthrene, BN-8a,9-phenanthrene and BN-9,8a-

phenanthrene) which BN bonds located at single bond positions show visible alterations throughout the skeleton. Only one BN-phenanthrene analogue (BN-9,10-phenanthrene) which BN bond located at the double bond position has almost no effect on the two aromatic rings. This classification of BN phenanthrene isomers based on the three different bond positions is useful to distinguish the effects of BN doping on the geometry of PAHs.

Table 2.5 Bond lengths differences (Å) between phenanthrene and BN-phenanthrene isosteres have been calculated at CCSD/cc-pVDZ level. Differences with an absolute value greater than 0.015 are marked in red.

	1-2	2-3	3-4	4-4a	4a-10a	4a-4b	4b-5	5-6	6-7	7-8	8-8a	4b-8a	8a-9	9-10	10-10a	1-10a
Phen	1.389	1.419	1.391	1.426	1.424	1.470	1.426	1.391	1.419	1.389	1.425	1.424	1.451	1.366	1.451	1.425
BN-12	0.039	0.119	-0.016	0.028	-0.017	-0.011	0.006	-0.003	0.004	-0.004	0.004	0.004	-0.011	0.006	-0.013	-0.037
BN-21	0.037	-0.034	-0.024	0.028	-0.010	-0.009	0.005	-0.004	0.004	-0.004	0.005	0.004	-0.009	0.007	-0.008	0.119
BN-23	-0.025	0.024	0.128	-0.030	0.032	0.019	-0.007	0.005	-0.006	0.005	-0.006	-0.001	0.011	-0.007	0.009	-0.038
BN-32	0.128	0.025	-0.025	-0.039	0.032	0.012	-0.006	0.005	-0.006	0.005	-0.007	-0.003	0.011	-0.006	0.015	-0.029
BN-34	-0.024	-0.034	0.037	0.122	-0.010	-0.011	0.006	-0.004	0.005	-0.003	0.003	0.003	-0.009	0.006	-0.006	0.027
BN-43	-0.015	0.120	0.039	-0.038	-0.018	-0.016	0.005	-0.004	0.004	-0.004	0.004	0.004	-0.010	0.006	-0.010	0.027
BN-44a	0.043	-0.039	-0.018	0.014	0.111	0.091	-0.008	0.007	-0.007	0.008	-0.006	0.004	0.023	0.000	0.010	-0.035
BN-4a4	0.033	-0.034	0.126	0.042	-0.020	-0.029	-0.010	0.006	-0.009	0.004	-0.008	-0.006	0.005	-0.011	0.007	-0.035
BN-4a10a	-0.015	0.024	-0.022	-0.031	0.043	-0.043	-0.006	0.005	-0.009	0.003	-0.005	0.000	0.009	-0.004	0.095	0.113
BN-10a4a	-0.021	0.025	-0.014	0.112	0.038	0.088	-0.005	0.005	-0.003	0.005	-0.005	-0.001	0.009	-0.007	-0.045	-0.035
BN-8a9	-0.014	0.017	-0.014	0.018	0.018	-0.035	0.017	-0.017	0.014	-0.022	-0.031	-0.035	0.039	0.116	-0.035	0.023
BN-98a	-0.015	0.020	-0.014	0.021	0.021	-0.040	0.018	-0.009	0.029	-0.008	0.108	0.101	0.013	-0.025	-0.041	0.019
BN-110a	-0.019	-0.040	0.041	-0.034	0.114	0.010	-0.007	0.006	-0.007	0.006	-0.006	0.003	0.023	0.000	0.099	0.017
BN-10a1	0.125	-0.033	0.034	-0.036	-0.023	0.014	-0.006	0.005	-0.006	0.005	-0.008	-0.006	0.006	-0.014	-0.040	0.038
BN-4a4b	-0.018	0.019	-0.024	-0.032	-0.035	0.022	0.110	-0.008	0.029	-0.010	0.017	0.097	-0.040	0.032	-0.037	-0.011
BN-910	0.006	-0.006	0.005	-0.005	0.000	0.015	-0.006	0.005	-0.008	0.005	-0.010	-0.003	-0.049	0.048	0.102	-0.005

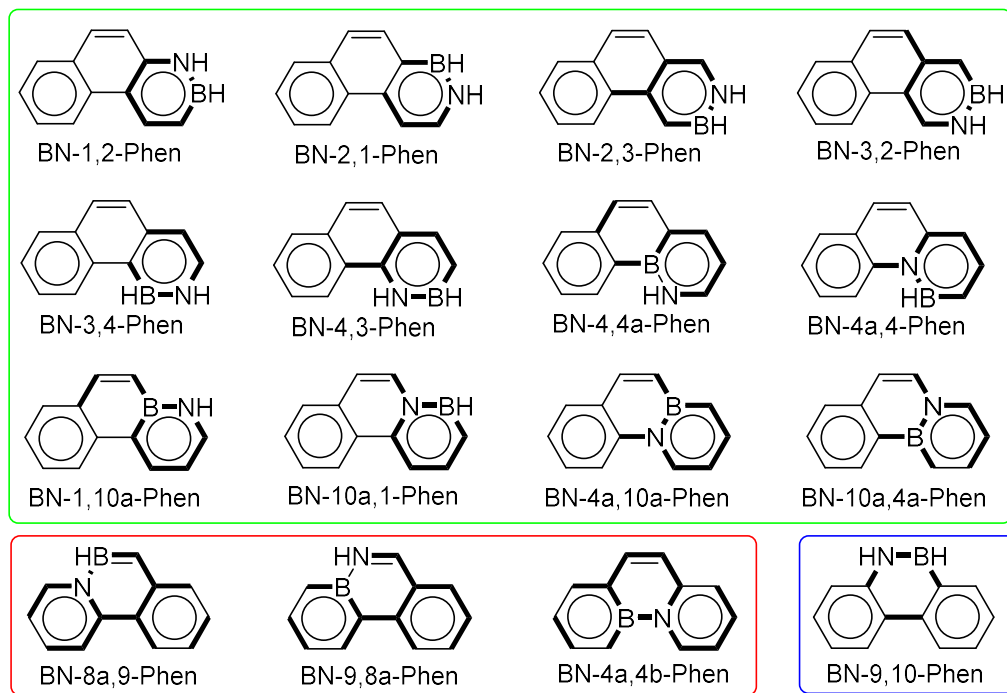
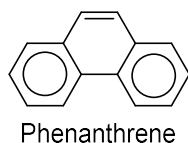


Figure 2.3. Molecular structures of phenanthrene and sixteen BN phenanthrene isosteres are represented in Clar's structure. The bond lengths which have significant differences are marked in bold type.

Although we claimed that the replacement of a CC single bond with a BN bond will cause significant changes in the entire skeleton of phenanthrene, these changes are likely to be less pronounced in larger aromatic hydrocarbons. To investigate further, we calculated the bond lengths of picene and BN-4a,4b-picene (Table 2.6). Through the same comparative analysis, we observed that, even if the threshold of the significant difference is set to 0.005, the part containing the BN-phenanthrene shows important changes while the distant naphthalene part is barely affected (Figure 2.5). The decrease in bond length variation between picene and BN-4a,4b-picene compared to the difference between BN-4a,4b-phenanthrene and all-carbon phenanthrene may be a

result of the bond lengths tending to average out as the conjugation system increases. This suggests that the changes resulting from the incorporation of BN bonds are limited to six-membered rings associated with boron and/or nitrogen, up to four rings in a large π -conjugated structure like graphene, and the BN doping influence on bond length becomes weaker in larger conjugated systems.

Table 2.6 Bond lengths (Å) of picene and BN-4a,4b-picene have been calculated at B3LYP/6-311G(d,p) level. Differences in bond lengths with an absolute value greater than 0.005 are marked in red.

	1-2	2-3	3-4	4-4a	4a-14a	4a-4b	4b-12b
Picene	1.376	1.407	1.379	1.415	1.424	1.453	1.417
BN-4a4b	1.364	1.420	1.359	1.380	1.394	1.487	1.511
diff.	-0.012	0.013	-0.020	-0.035	-0.030	0.034	0.094

	4b-5	5-6	6-6a	6a-12a	6a-6b	6b-10a	6b-7
Picene	1.420	1.366	1.420	1.417	1.453	1.424	1.415
BN-4a4b	1.515	1.365	1.442	1.418	1.452	1.428	1.419
diff.	0.095	-0.001	0.022	0.001	-0.001	0.004	0.004

	7-8	8-9	9-10	10-10a	10a-11	11-12	12-12a
Picene	1.379	1.407	1.376	1.414	1.427	1.360	1.433
BN-4a4b	1.378	1.408	1.375	1.415	1.423	1.361	1.429
diff.	-0.001	0.001	-0.001	0.001	-0.003	0.002	-0.003

	12a-12b	12b-13	13-14	14-14a
Picene	1.446	1.433	1.360	1.427
BN-4a4b	1.452	1.404	1.386	1.402
diff.	0.006	-0.029	0.026	-0.025

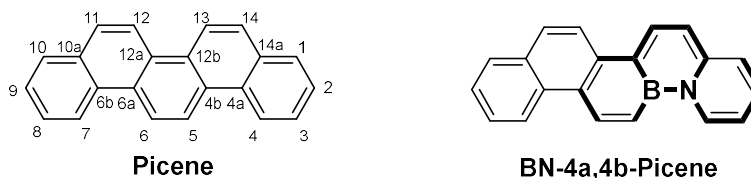


Figure 2.4. Molecular structure of picene and BN-4a,4b-picene. The bond lengths which have significant differences are marked in bold type.

2.3.2 Mayer bond orders

To obtain more insights about the role of the BN bond in PAHs, we calculated the Mayer bond orders of phenanthrene and its BN analogues. To obtain some reference to be used in our analysis as, we also calculated the bond orders for representative simple molecules and their BN isosteres, including ethane, ethene, ethyne, benzene, ammonia borane, aminoborane, iminoborane, 1,2-azaborine, and boron nitride (Figure 2.5). Ideally, the single, double and triple carbon-carbon bonds should exhibit 1.0, 2.0 and 3.0 Mayer bond-orders, respectively. For benzene, a system with highly delocalized electrons, we can consider that each C-C bond is the sum of a σ bond and half a π bond, so the value of Mayer bond order should close to 1.5.

The above analysis has been carried out on molecular geometries optimized at B3LYP/6-311G(d,p) level. The obtained Mayer bond orders of the reference molecules as references were found consistent with our chemical intuition. Compared with all-carbon molecules, the BN isosteres have irregular bond orders due to the symmetry breaking occurring after the incorporation of the BN bond and also due to the polarity of BN bond. The bond-order of ammonia borane is 0.64, less than 1.0, which is consistent with the coordinate-covalent bond character. The bond order of aminoborane is 1.47, which can be roughly divided into two parts. The dominant part (1.00) is related to the formation of a localized BN sigma bond, while the rest (0.47) comes from a “delocalized” electron that could be attributed to lone pair electrons of nitrogen to form a BN pi bond. This means the lone pair electrons of nitrogen only share a maximum of one electron to the empty orbital of boron because four substituted hydrogen atoms have low electronegativity. Therefore, BN single bond has a partial pi-bond character. Furthermore, when a BN bond is incorporated in a benzene ring, the bond order of the BN bond reduces to 1.19 indicating a much weaker BN π bond character most likely because the lone pair electrons of nitrogen could delocalize to the carbon fragment via mesomeric effect. Finally, it is useful to stress that in boron nitride the bond orders of the BN bond are larger than in 1,2-azaborine.

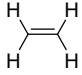
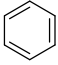
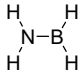
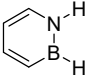
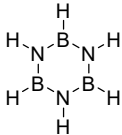
	$\text{H}_3\text{C}-\text{CH}_3$		$\text{H}-\text{C}\equiv\text{C}-\text{H}$		
	ethane	ethene	ethyne	benzene	
Mayer bond orders (C-C bond)	1.01	1.98	2.78	1.44	
	$\text{H}_3\text{N}-\text{BH}_3$		$\text{H}-\text{N}=\text{B}-\text{H}$		
	ammonia borane	aminoborane	iminoborane	1,2-azaborine	boron nitride
Mayer bond orders (B-N bond)	0.64	1.47	2.43	1.19	1.23

Figure 2.5. Mayer bond orders of C-C bond of ethane, ethene, ethyne, benzene and their BN analogues have been calculated at B3LYP/6-311G(d,p) level.

The bond orders between the heavy atoms of phenanthrene and its BN analogues are listed in Table 2.7. In all cases the obtained bond types of phenanthrene are found consistent with Clar's representation. The same goes for the bond lengths. Specifically, the bond orders of C4a-C4b, C8a-C9 and C10-C10a are 1.21, 1.20, and 1.20, respectively, which have more single bond characteristics. The bond order of C9-C10 amounts to 1.63, thus, it is of strong double character. The rest of the C-C bonds are located at aromatic rings, the bond orders are distributed between 1.32-1.51. This implies that these bonds should have some multi-center bond characteristics. Unlike to the fully delocalized π electrons of benzene, the Kekulé sextet of phenanthrene shows partial delocalized π electrons. In brief, C1-C2, C3-C4, C5-C6 and C7-C8 bonds should have partial double bond characteristics. On the other hand, C1-C10a, C2-C3, C4-C4a, C4a-C10a, C4b-C5, C6-C7, C4b-C8a and C8-C8a bonds should carry partial single bond characteristics. Of course, it wouldn't be safe to regard a bond order of 1.63 as a double bond and a bond order of 1.20 as a single bond, nevertheless, we decided to adopt these simplifications to simplify our analysis.

All BN bond orders of sixteen BN phenanthrene isosteres are distributed between 0.95-1.28 (in red color), which have more single bond characteristics, especially BN-

4a,4b-phenanthrene, BN-8a,9-phenanthrene and BN-9,8a-phenanthrene which BN bond orders extremely close to 1.00 indicating that limited π electrons delocalize from nitrogen to boron. Interestingly, we find that all BN bond orders are positively correlated with the corresponding CC bond orders, in other words, a BN bond which is located at a double bond position has a larger bond order, and a BN bond which is located at a single bond position has a smaller bond order. It is also worthwhile to investigate how the integration of BN bonds affects the bond order of other bonds. We discover that the bond order within the azaborine ring will alter whether the replacement of BN/CC occurs at the double bond or in the Kekulé ring. For BN/CC single bond replacement, all the bond orders alter, especially in the central ring.

Table 2.7 The Mayer bond orders of phenanthrene and BN-phenanthrene isosteres have been calculated at B3LYP/6-311G(d,p) level.

	1-2	2-3	3-4	4-4a	4a-10a	4a-4b	4b-5	5-6	6-7	7-8	8-8a	4b-8a	8a-9	9-10	10-10a	1-10a
Phen	1.51	1.34	1.51	1.35	1.35	1.21	1.35	1.51	1.34	1.51	1.32	1.35	1.20	1.63	1.20	1.32
BN-12	1.23	1.14	1.65	1.24	1.36	1.24	1.33	1.53	1.33	1.53	1.30	1.34	1.24	1.61	1.22	1.14
BN-21	1.23	1.17	1.66	1.24	1.41	1.21	1.33	1.53	1.32	1.53	1.30	1.33	1.23	1.58	1.24	1.11
BN-23	1.26	1.14	1.24	1.52	1.24	1.13	1.37	1.48	1.36	1.49	1.34	1.36	1.17	1.68	1.16	1.48
BN-32	1.24	1.15	1.26	1.50	1.24	1.16	1.37	1.49	1.37	1.49	1.34	1.37	1.16	1.67	1.16	1.49
BN-34	1.66	1.16	1.23	1.11	1.40	1.22	1.33	1.53	1.32	1.53	1.31	1.32	1.23	1.61	1.21	1.22
BN-43	1.65	1.14	1.23	1.17	1.35	1.19	1.29	1.54	1.33	1.53	1.31	1.36	1.23	1.60	1.24	1.22
BN-44a	1.34	1.54	1.26	1.12	1.03	0.98	1.37	1.48	1.38	1.48	1.34	1.36	1.17	1.69	1.18	1.47
BN-4a4	1.34	1.53	1.23	1.11	1.13	1.01	1.38	1.49	1.37	1.48	1.36	1.31	1.14	1.64	1.16	1.45
BN-4a10a	1.63	1.24	1.64	1.18	1.05	1.06	1.33	1.50	1.37	1.49	1.35	1.34	1.17	1.70	1.04	1.10
BN-10a4a	1.63	1.25	1.64	1.10	1.04	0.99	1.37	1.49	1.37	1.49	1.33	1.36	1.18	1.72	1.10	1.17
BN-8a9	1.58	1.28	1.57	1.30	1.27	1.28	1.27	1.56	1.25	1.58	1.18	1.12	1.01	1.36	1.36	1.25
BN-98a	1.58	1.27	1.57	1.27	1.28	1.31	1.29	1.57	1.28	1.62	1.12	1.06	1.01	1.38	1.35	1.25
BN-110a	1.27	1.54	1.34	1.49	1.03	1.17	1.36	1.48	1.37	1.48	1.36	1.36	1.17	1.73	1.04	1.10
BN-10a1	1.24	1.53	1.34	1.48	1.08	1.10	1.38	1.49	1.36	1.48	1.34	1.34	1.13	1.69	1.09	1.10
BN-4a4b	1.57	1.24	1.59	1.18	1.15	0.95	1.11	1.62	1.28	1.58	1.27	1.06	1.35	1.48	1.33	1.24
BN-910	1.47	1.37	1.48	1.36	1.36	1.15	1.38	1.48	1.38	1.49	1.35	1.32	1.08	1.28	1.06	1.35

2.3.3 Electron Localization Function (ELF) π -orbitals

In addition to information about the single and double bond characters in molecules, bond lengths and bond orders can inform us about the distribution of π -orbitals based on fact that a double bond should have π -bonding characteristics and a single bond π -antibonding characteristic. Although phenanthrene and its BN analogues have seven π -bonding orbitals, it would be complicate to examine them independently. Actually, the seven-in-one π -bonding orbitals can be analyzed by the electron localization function (ELF) which is a three-dimensional function that can be used to retrieve insights related electron localization and delocalization. Herein, the images of the π -orbitals distribution of phenanthrene and its BN analogues have been obtained with the Multiwfn program (3.8 dev version) (Figure 2.6). The initial wave function involving information of molecular orbitals is calculated at B3LYP/6-311G(d,p) level. All the π -orbitals of phenanthrene and its BN isomers are shown with an isovalue of 0.7. Additional π -orbitals of phenanthrene have been visualized using an isovalue of 0.9. The Clar's structure can be clearly distinguished by the visualized π -orbitals (isovalue = 0.7) of phenanthrene. The local orbital characteristics of the Kekulé sextet can be displayed by tuning the isosurface value. From the π -orbitals diagram (isovalue = 0.9) of phenanthrene, the π -electrons of these two Kekulé sextets are not highly delocalized like benzene. C1-C2, C3-C4, C5-C6 and C7-C8 bonds have partial π -bonding characteristics. According to the prior bond length and bond order analysis, C4a-C10a, C4b-C8a bonds exhibit partial single-bond characteristics similar to C2-C3. However, when viewed from the perspective of π -orbitals, C4a-C10a, C4b-C8a still exhibit some partial π -bonding characteristics, albeit less obviously than C1-C2. This is most likely because the two ring-junction carbons have lower electron populations.

The π -orbitals distribution of phenanthrene is crucial for the analysis of the results of this thesis chapter. Based on the Clar's structure and ELF- π analysis, four categories of bonds in phenanthrene can be identified. These are, a double bond (C9-C10), six partial double bonds (C1-C2, C3-C4, C5-C6, C7-C8, C4a-C10a and C4b-C8a), three

single bonds (C4a-C4b, C8a-C9 and C10-C10a) as well as partial single bonds (C1-C10a, C2-C3, C4-C4a, C4b-C5, C6-C7 and C8-C8a). In addition, the BN bond doping does not significantly alter the distribution of π orbitals in phenanthrene, as indicated by the presented ELF- π orbitals.

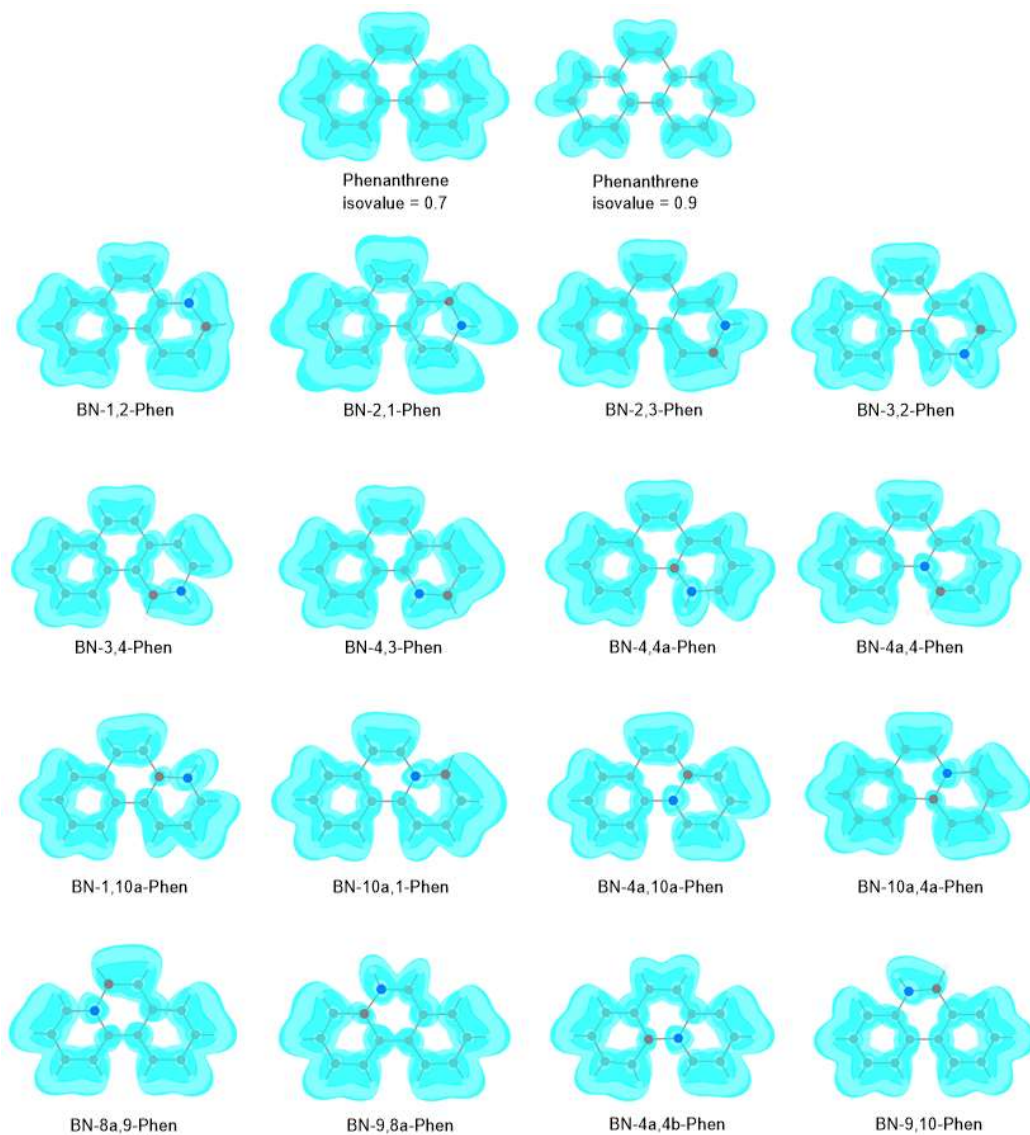


Figure 2.6. π -Orbitals of phenanthrene and 16 BN analogues (isosurface value = 0.7) have been calculated at B3LYP/6-311G(d,p) level.

2.3.4 Nucleus-Independent Chemical Shift (NICS)

We carried out nucleus-independent chemical shift (NICS) calculations to understand the impact of the position and orientation of the BN bond on the aromaticity of BN-phenanthrene at CAM-B3LYP/6-311G(d,p) level. The NICS were calculated at the approximate centre of the six-member rings (NICS(0)) and at 1 Å above the ring on the axis perpendicular to the ring and passing through the approximate centre of the ring (NICS(1)zz (Table 2.8). Note that strongly negative NICS values correspond to high degrees of aromaticity. The obtained results indicate consistency between NICS(0) and NICS(1)zz. In phenanthrene, the middle ring should be less aromatic than the external rings. Overall, BN doping reduces the aromaticity of phenanthrene. The BN phenanthrene isomers with opposite orientations of BN bonds have similar aromaticity. Depending on the position of the BN bond, the BN doping has different effects on the aromaticity of BN phenanthrene isomers. Specifically, the degree of aromaticity of the BN ring is found to reach a minimum value when the BN bond is placed in the position of a double bond or a partial double bond, whereas the aromaticity of the central ring is reduced when the BN bond is located in a position of a partial single bond. Conversely, the highest degree of aromaticity of the central ring is observed when the BN bond is situated in the position of a single bond.

Table 2.8 NICS(0) and NICS(1)zz values of phenanthrene and BN analogues have been calculated at CAM-B3LYP/6-311G(d,p) level.

	NICS(0)			NICS(1)zz		
	left	middle	right	left	middle	right
Phen	-11.5	-8.9	-11.5	-29.3	-20.0	-29.3
BN-12	-11.4	-10.1	-6.8	-28.9	-23.5	-16.9
BN-21	-11.6	-10.3	-6.4	-29.3	-24.5	-16.0
BN-23	-11.1	-5.5	-8.6	-28.1	-10.0	-23.0
BN-32	-11.0	-5.6	-8.8	-27.7	-10.1	-23.4
BN-34	-11.5	-10.1	-6.4	-29.2	-24.2	-16.2
BN-43	-11.4	-10.2	-6.7	-28.8	-23.9	-16.6
BN-44a	-11.4	-4.9	-8.4	-29.4	-10.3	-22.6
BN-4a4	-10.9	-4.1	-8.5	-27.2	-7.1	-22.3
BN-4a10a	-11.4	-5.9	-7.2	-28.7	-12.9	-18.6
BN-10a4a	-11.6	-5.6	-7.5	-29.8	-12.6	-19.3
BN-8a9	-8.1	-9.8	-9.4	-20.1	-25.1	-22.8
BN-98a	-9.1	-10.0	-9.5	-24.4	-26.1	-23.2
BN-110a	-11.1	-5.0	-8.4	-28.1	-10.4	-22.4
BN-10a1	-10.8	-4.2	-8.5	-27.1	-7.6	-22.5
BN-4a4b	-8.7	-9.6	-7.3	-23.1	-24.9	-17.9
BN-910	-11.3	-4.3	-10.8	-28.7	-8.2	-27.1

2.3.5 Electric dipole moment

The incorporation of a BN bond results in the conversion of phenanthrene from a nonpolar to a polar molecule. The electric dipole moments of BN phenanthrene isomers have been calculated at B3LYP/6-311+G(d,p) level. The results indicate that the dipole moments of BN-phenanthrene isomers vary from the positions of the BN bond. The direction of the molecular dipole moment of each BN-phenanthrene is determined by the orientation of the BN bond, always pointing from the boron atom to the nitrogen atom (Figure 2.7). The magnitude of the dipole moments is related to the position of

the BN bond (Figure 2.8). The BN phenanthrene isomers with opposite orientations of BN bonds have a similar dipole moment. The BN phenanthrene isomer with the BN bond located in the double bond position displays the lowest dipole moment, whereas higher dipole moments are observed in the BN phenanthrene isomers with the BN bond located in the partial double bond position. For BN phenanthrene isomers where the BN bond is located in the partial single bond position, the dipole moment is larger than that of BN/CC partial double bond substituted isomers. The BN phenanthrene isomer with the largest dipole moment is observed when the BN bond is located in the single bond position.

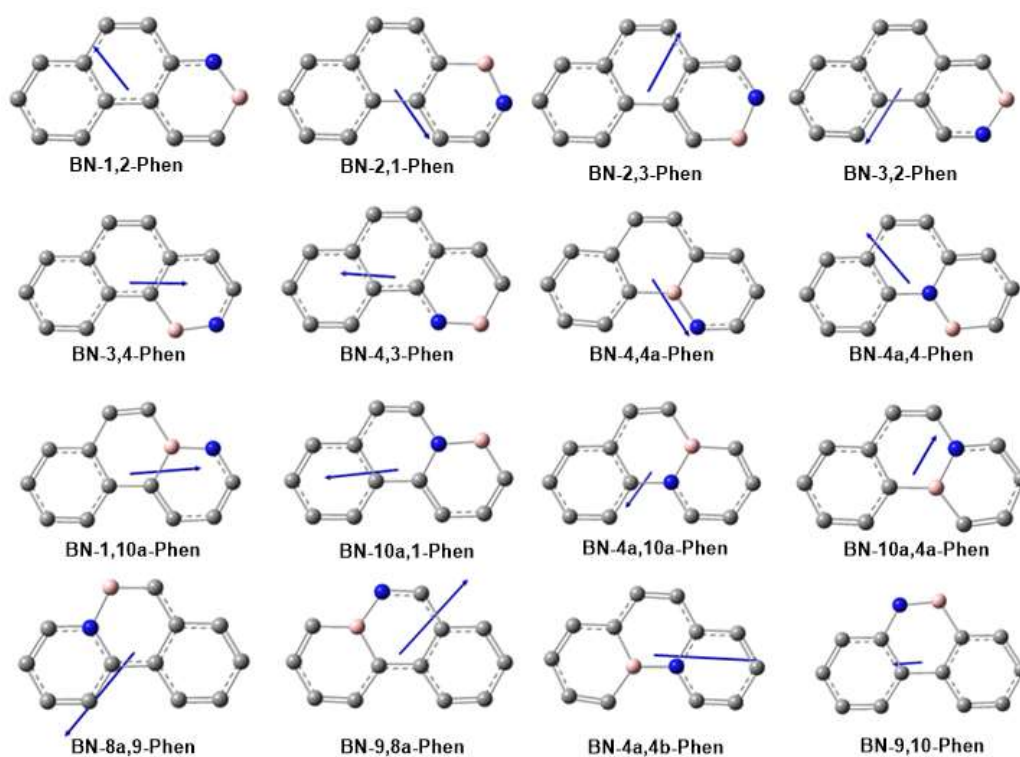


Figure 2.7 Electric dipole moment vectors of 16 BN phenanthrene isomers have been calculated at B3LYP/6-311+G(d,p) level.

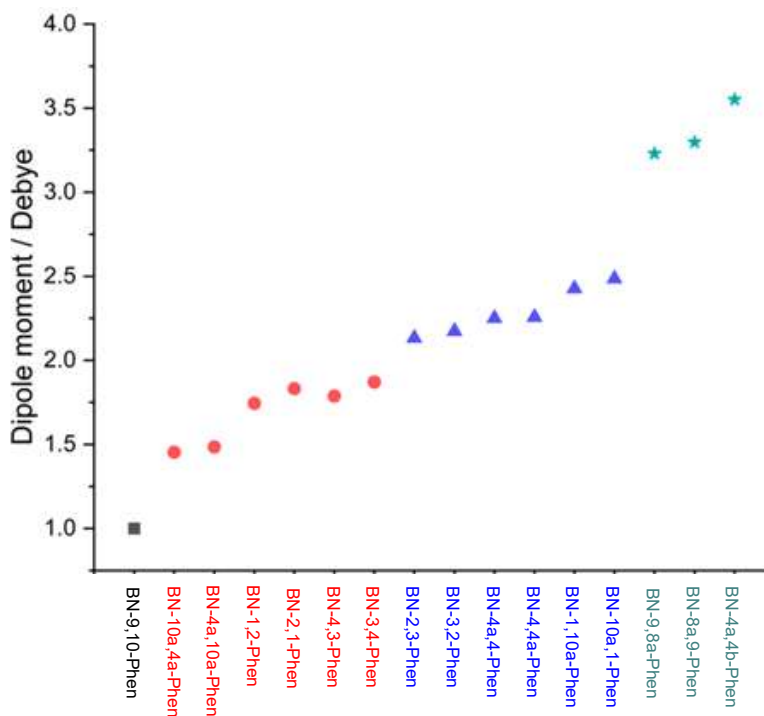


Figure 2.8 Magnitude distributions of dipole moments of 16 BN phenanthrene isomers.

2.3.6 Electrostatic Potential Map

The electrostatic potential (ESP) maps of phenanthrene and sixteen BN analogues were investigated at the B3LYP/6-311G(d,p) level (Figure 2.9), providing a three-dimensional representation of the charge distribution of the molecules. The ESP surfaces are depicted in the hemisphere to simulate molecular charge distributions, where the red color indicates the most negative charges and the blue color represents the most positive charges. The non-polar phenanthrene displays the most positive charge on the carbon skeleton. The charge distribution of BN analogues is influenced by the position and orientation of the BN bond. In general, the most positive charge is located at the nitrogen atom side, while the most negative charge is found at the carbon atoms and boron atom side. Separation of positive and negative charges is observed when the NC5 six-membered ring is present in the molecules. BN-8a,9-phenanthrene

and BN-4a,4b-phenanthrene exhibit clearly separated charges, while BN-4a,4-phenanthrene and BN-10a,1-phenanthrene display less distinct separation.

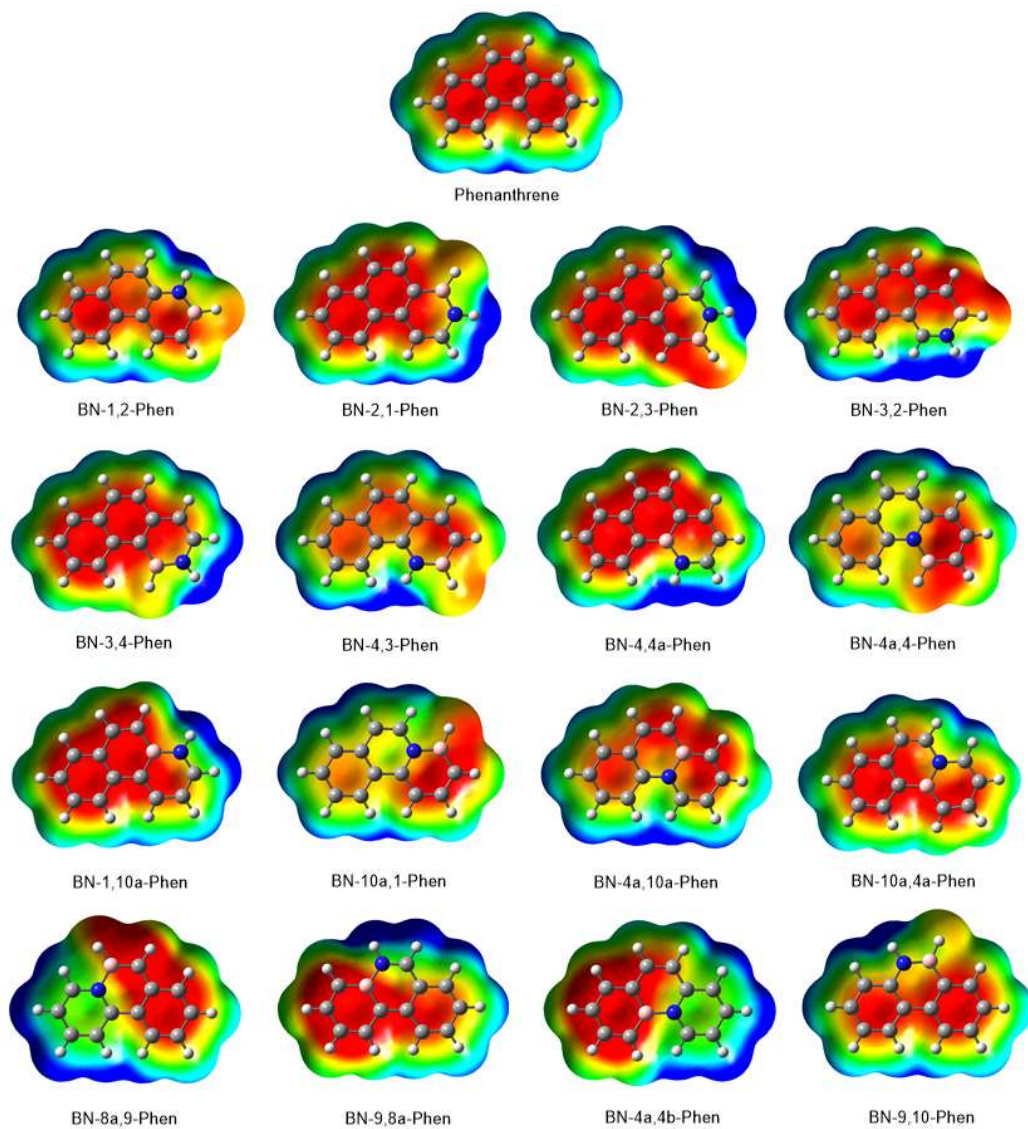


Figure 2.9 Electrostatic potential maps (B3LYP/6-311G(d,p)) for phenanthrene and BN phenanthrene analogues at a 0.0004 electron au isocontour level (+12.55 to -12.55 kcal/mol). Red is the most electron-rich, and blue is the most electron deficient.

2.3.7 Frontier molecular orbitals

In this subsection we will report some practical and empirical guiding principles concerning the frontier molecular orbital (FMO) energies of BN compounds as a function of the position of the BN unit. We calculated the highest occupied molecular orbital (HOMO) and the lowest unoccupied molecular orbital (LUMO) of phenanthrene and its sixteen BN analogues at the B3LYP/6-311G(d,p) level (Figure 2.10). Depending on the position of the BN bond, the FMO energies of BN phenanthrene isosteres may differ significantly from those of the all-carbon analogue. The discrepancies in HOMO, LUMO, and their energy gaps between phenanthrene and the BN analogues can be interpreted using our partitioning of double bond position, partial double bond position, single bond position, and partial single bond position.

Analysis of the FMO reveals that isomers with BN bonds in the same position but opposite orientations have similar HOMO-LUMO energy gaps. BN-9,10-phenanthrene, with the BN bond located at the double bond position, exhibits a slightly larger HOMO-LUMO gap (4.81 eV), with a higher-lying LUMO and a lower-lying HOMO, compared to phenanthrene (4.72 eV). Isomers with the BN bond located at the partial double bond position have a similar or slightly smaller HOMO-LUMO gap (4.30 to 4.68 eV) than all-carbon phenanthrene. Specifically, BN-4a,12a-phenanthrene and BN-12a,4a-phenanthrene have lower-lying LUMOs and higher-lying HOMOs, as well as an extremely similar HOMO-LUMO gap with phenanthrene, BN-1,2-phenanthrene, BN-2,1-phenanthrene, BN-3,4-phenanthrene and BN-4,3-phenanthrene have lower HOMO-LUMO gaps. Six isomers with the BN bond located at the partial single bond position exhibit a significantly lower HOMO-LUMO gap (3.83 to 4.12 eV), with lower-lying LUMOs and higher-lying HOMOs. Three isomers with the BN bond located at the single bond positions have the lowest HOMO-LUMO gap (3.33 to 3.52 eV), with the lowest-lying LUMO and the highest-lying HOMO.

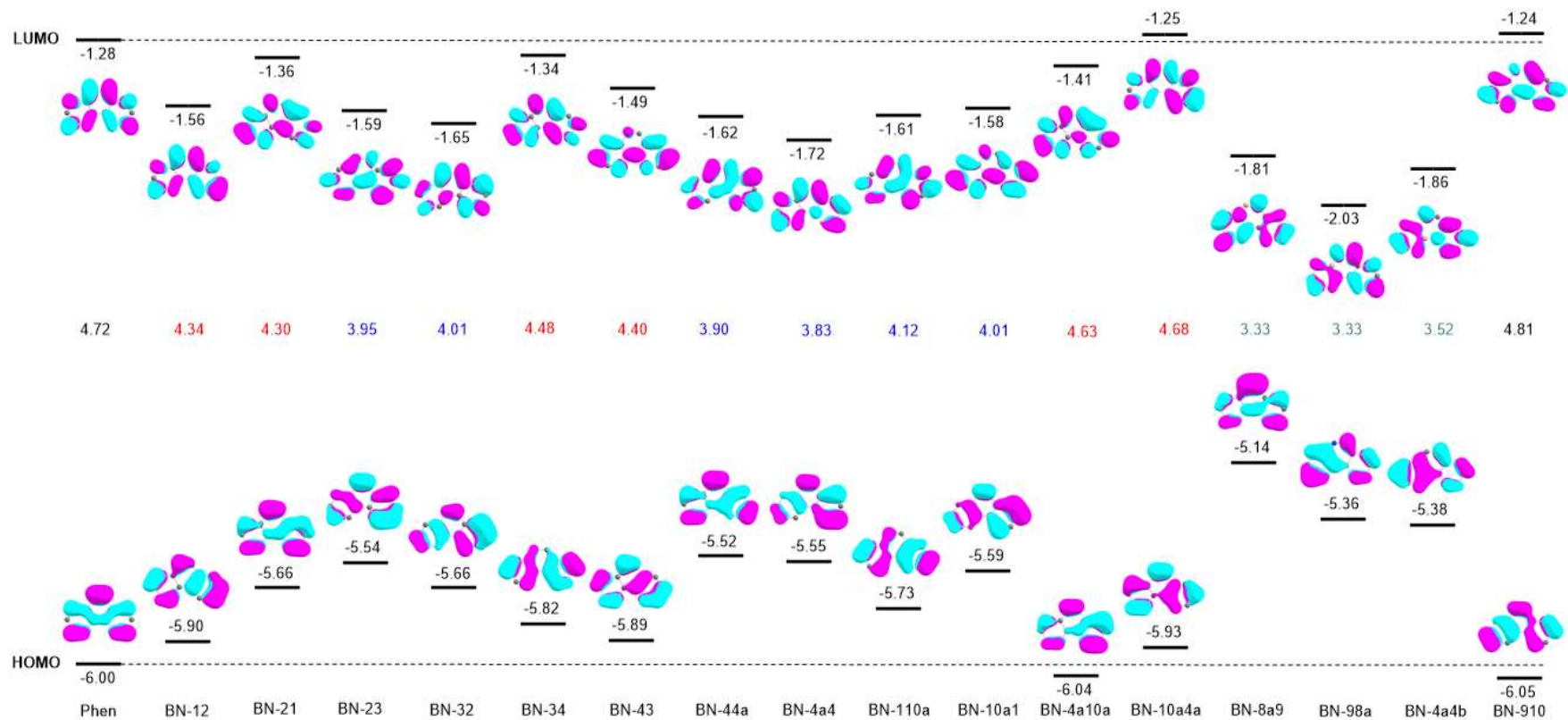


Figure 2.10. Molecular frontier orbital isosurfaces (isovalue = 0.03) and energies (eV) have been calculated at B3LYP/6-311G(d,p) level.

2.3.8 Vertical Excitation

The vertical excitation of the first singlet excited state of phenanthrene and BN phenanthrene analogues has been investigated by TD-DFT calculations at PBE0/6-311G(d,p) level (Table 2.9). Key information on phenanthrene with respect to the first vertical excitation energy, optical gap, oscillator strength, transition electric dipole moment and major transition orbitals is revealed (Table 2.8). Compared to phenanthrene, the transition electric dipole moments increase significantly with the doping of BN bonds, which indicates a possible absorption peak could be observed during the excitation from the ground state to the first excited state. The first excitation of phenanthrene can be approximately described by the transition from HOMO to LUMO+1 (contribution is 59%) and the transition from HOMO-1 to LUMO (contribution is 39%). Among all BN phenanthrene isomers, except that the excitation of BN-8a,9-phenanthrene is approximately described by the transition from HOMO to LUMO+1 (contribution is 91%), the excitation of all the BN analogues can be majorly described by the transition from HOMO to LUMO. The excitation energy of BN phenanthrene analogues can be also discussed in our four categories, which is similar with the HOMO-LUMO gaps. The only distinction with the HOMO-LUMO gaps is that the excitation energy of BN-4a,10a-phenanthrene and BN-10a,4a-phenanthrene are slightly higher than in all-carbon phenanthrene.

Table 2.9 Comparisons of excitation energies (E_{S_1}), absorption wavelengths (λ_{S_1}), oscillator strengths (f), transition electric dipole moments (D) major molecular orbital transitions with contribution between phenanthrene and BN analogues have been calculated at TD-PBE0/6-311G(d,p) level.

	E_{S_1}	λ_{S_1}	f	Transition dipole moment	Major transition
Phen	4.11 eV	302 nm	0.0015	0.0148	HOMO->LUMO+1 (59%)
BN-12	4.02 eV	308 nm	0.1436	1.4568	HOMO->LUMO (85%)
BN-21	3.95 eV	314 nm	0.0990	1.0226	HOMO->LUMO (84%)
BN-23	3.67 eV	338 nm	0.0753	0.8386	HOMO->LUMO (92%)
BN-32	3.75 eV	331 nm	0.1002	1.0899	HOMO->LUMO (93%)
BN-34	4.04 eV	307 nm	0.0517	0.5222	HOMO->LUMO (68%)
BN-43	4.00 eV	310 nm	0.0704	0.7180	HOMO->LUMO (72%)
BN-44a	3.70 eV	335 nm	0.2680	2.9584	HOMO->LUMO (93%)
BN-4a4	3.58 eV	346 nm	0.2478	2.8219	HOMO->LUMO (95%)
BN-110a	3.83 eV	323 nm	0.1740	1.8524	HOMO->LUMO (63%)
BN-10a1	3.72 eV	333 nm	0.2408	2.6392	HOMO->LUMO (79%)
BN-4a10a	4.17 eV	298 nm	0.0299	0.2930	HOMO->LUMO (83%)
BN-10a4a	4.22 eV	294 nm	0.0469	0.4536	HOMO->LUMO (70%)
BN-8a9	3.17 eV	391 nm	0.0309	0.3975	HOMO->LUMO+1 (91%)
BN-98a	3.22 eV	385 nm	0.2222	2.8187	HOMO->LUMO (95%)
BN-4a4b	3.29 eV	377 nm	0.1949	2.4162	HOMO->LUMO (88%)
BN-910	4.33 eV	287 nm	0.1296	1.2231	HOMO->LUMO (74%)

2.3.9 Adiabatic Excitation Energy

In addition to the first vertical excitation energy of phenanthrene and its BN analogues, we have also investigated the adiabatic energy of S_1 and T_1 states (Table 2.10), which may be used for predicting the fluorescence and phosphorescence emission wavelengths. Herein, we calculated the energy of S_1 and T_1 using seven different theory levels. Overall, the results from seven methods exhibit same trend which isomer of BN located at single bond or partial single bond positions have lower energy than isomer of BN located at double bond or partial partial bond positions.

Table 2.10 Adiabatic excitation energies of the first singlet excited state (S1) and the first triple excited state (T1) of phenanthrene and 16 BN analogues have been investigated by different methods involving B3LYP, PBE0, CAM-B3LYP, wB97XD, M06-2X, CCSD and CASSCF.

Molecule	B3LYP		PBE0		CAM-B3LYP		wB97XD		M06-2X		CCSD		CASSCF (14,14)	
	S ₁	T ₁	S ₁	T ₁	S ₁	T ₁	S ₁	T ₁	S ₁	T ₁	S ₁	T ₁	S ₁	T ₁
Phen	3.86	2.77	3.97	2.76	4.18	2.84	4.19	2.89	4.20	3.08	4.00	2.87	4.24	2.93
BN-12	3.75	2.59	3.86	2.60	4.06	2.67	4.07	2.71	4.07	2.85	4.02	2.73	3.92	2.57
BN-21	3.66	2.57	3.76	2.58	3.99	2.66	3.99	2.70	3.99	2.84	3.98	2.72	3.88	2.56
BN-23	3.40	2.24	3.49	2.22	3.70	2.29	3.71	2.33	3.69	2.43	3.76	2.36	3.85	2.25
BN-32	3.45	2.25	3.54	2.23	3.75	2.29	3.76	2.33	3.75	2.42	3.84	2.36	3.91	2.23
BN-34	3.77	2.80	3.88	2.81	4.10	2.92	4.10	2.97	4.10	3.12	4.01	2.99	3.85	2.71
BN-43	3.72	2.73	3.83	2.74	4.06	2.85	4.06	2.90	4.06	3.04	3.99	2.93	3.84	2.68
BN-44a	3.37	2.16	3.48	2.15	3.69	2.17	3.70	2.21	3.70	2.37	3.82	2.25	4.01	2.14
BN-4a4	3.25	2.16	3.35	2.14	3.60	2.16	3.61	2.21	3.59	2.34	3.65	⁻³	3.72	2.06
BN-110a	3.46	2.46	3.62	2.46	3.87	2.48	3.87	2.53	3.88	2.67	3.87	2.56	3.81	2.40
BN-10a1	3.35	2.45	3.49	2.44	3.77	2.48	3.78	2.52	3.76	2.64	3.73	2.53	3.77	2.41
BN-8a9	2.73	1.82	2.86	1.80	3.17	1.74	3.17	1.78	3.17	1.91	3.12	1.80	3.08	1.70
BN-98a	2.92	1.79	3.02	1.76	3.20	1.70	3.21	1.73	3.23	1.89	3.23	1.76	3.10	1.62
BN-4a10a	3.82	2.77	3.96	2.73	4.25	2.91	4.27	2.95	4.24	3.08	4.31	2.93	4.30	2.91
BN-10a4a	3.88	2.84	4.01	3.14	4.30	2.94	4.30	2.99	4.29	3.14	4.29	R	4.26	2.96
BN-4a4b	2.95	2.10	3.07	2.10	3.29	2.07	3.29	2.12	3.31	2.25	3.19	2.08	3.18	1.88
BN-910	4.06	3.07	4.17	3.09	4.36	3.19	4.37	3.25	4.38	3.38	4.25	3.19	4.29	2.91

³ The corresponding computation did not converge at the CCSD level

2.4 BN Doping Effects in PAHs

We have so far investigated systematically the influence of the BN incorporation on the structures and properties of phenanthrene from the aspects of bond length, bond order, dipole moment, aromaticity, molecular orbitals, excited states etc., and have provided empirical principles of these effects. To verify and improve these empirical criteria as well as to extend them to other PAH molecules, we have also calculated the frontier molecular orbitals and the optical gaps of some other typical PAHs including naphthalene, anthracene, tetracene, pyrene, triphenylene, picene, coronene and their BN analogues. According to the knowledge obtained from the study of phenanthrene, the positioning effects of BN bond are closely related to the distribution of pi electrons in polycyclic aromatic hydrocarbons. Specifically, isomers with the BN bond located at the double bond position of its parental all carbon counterpart have a slightly higher HOMO-LUMO and optical gaps than pristine phenanthrene. Isomers with the BN bond located at the partial double bond position have a slightly lower HOMO-LUMO gap and optical gap. On the other hand, isomers with the BN bond replacing a former partial single bond position have a significantly lower HOMO-LUMO and optical gaps than all-carbon phenanthrene. Finally, isomers with the BN bond located at the single bond position have the lowest HOMO-LUMO and optical gaps.

In this section, we have used both Clar's representations and ELF-pi orbitals of naphthalene, anthracene, tetracene, pyrene, triphenylene, perylene and coronene to distinguish four different positions involving single bond, partial single bond, double bond and partial double bond. All geometry optimizations and molecular orbital energies are calculated at B3LYP/6-311G(d,p) level. The optical gap is the vertical excitation energy of first singlet excited state calculated by TD-DFT at the same theory level. The oscillator strengths are checked for exclusion of dark states. ELF-pi orbitals are performed by Multiwfn program. The isovalues of HOMO, LUMO and ELF-pi orbitals isosurfaces are 0.03 and 0.7 respectively.

The optical gap differences between naphthalene, phenanthrene, anthracene, tetracene, pyrene, triphenylene, perylene, coronene and their BN analogues have been plotted into four groups (Figure 2.11). The capability of mono-BN bond tuning on the optical gap ranges from -

1.6 eV to 0.3 eV. We suppose that the effect of BN bond doping on the optical gap of PAHs decreases as they grow larger due to more equal bond lengths, and the features of single and double bonds are minimized.

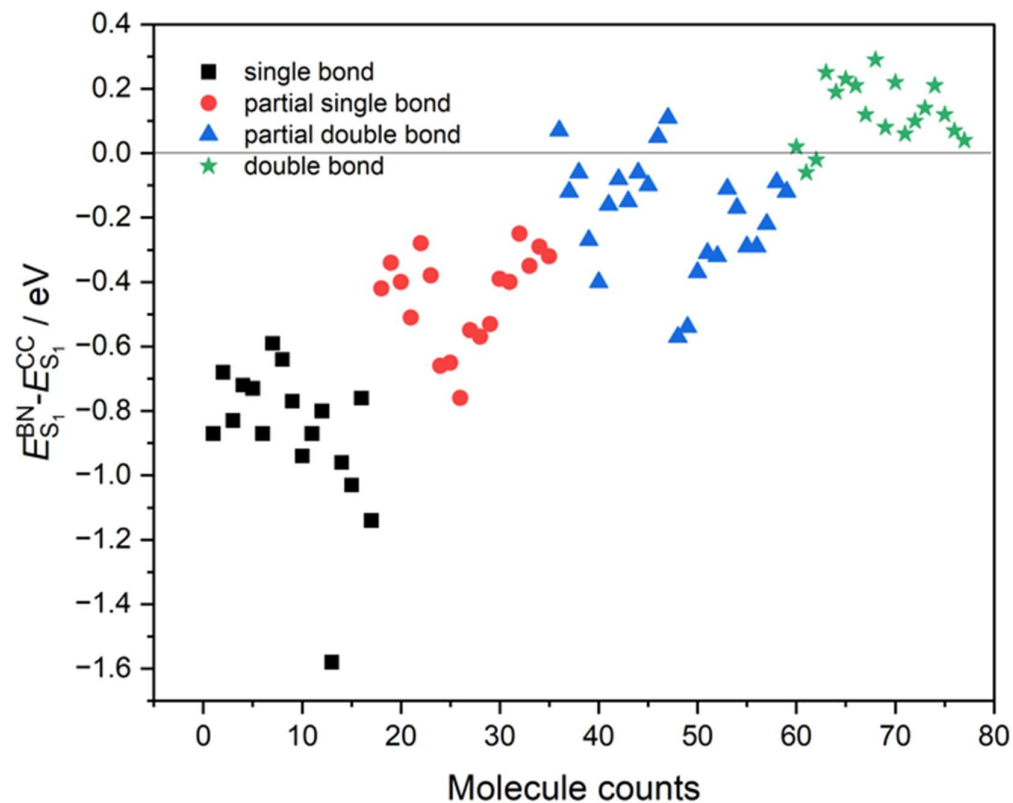


Figure 2.11 The energy difference distribution between PAHs and BN-doped PAHs. black squares represent BN/CC single bond replaced isosteres, green stars represent BN/CC double bond replaced isosteres, red spots represent BN/CC partial single bond replaced isosteres and blue triangles represent BN/CC partial double bond replaced isosteres. More information can be found in the Appendix.

The BN/CC double bond or partial double bond replaced analogues which BN bonds are in opposite orientations have very similar HOMO-LUMO gap and optical gap, BN/CC single bond or partial single bond replaced analogues which BN bonds are in opposite orientations indicate that the B-NH type of molecules always have higher energy of HOMO, LUMO, HOMO-LUMO gap and optical gap than N-BH type of molecules. The energy difference of optical gaps between B-NH type molecules and N-BH type molecules have been plotted. The

range of the energy difference is from 0.02 eV to 0.2 eV, showing in Figure 2.12.

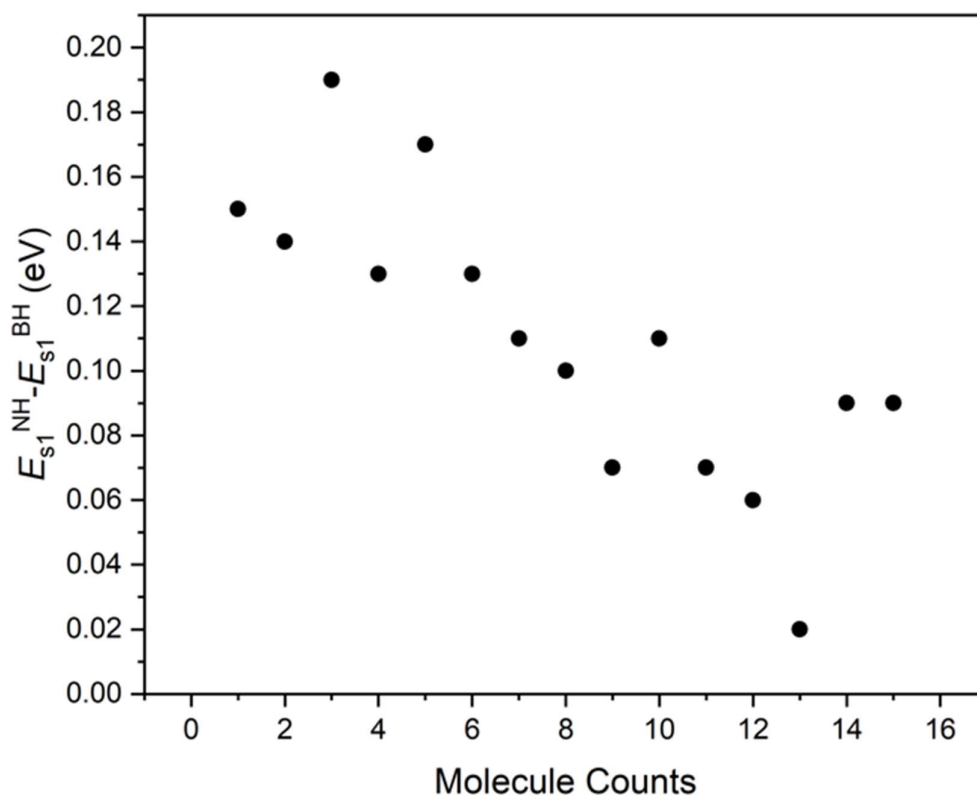


Figure 2.12 The energy difference distribution between B-NH and N-BH isomers.

To analyze the above results, we used Clar's theory of aromaticity to obtain the privileged Lewis structures and unfavorable Lewis structures of three examples comprising phenanthrene, triphenylene and coronene (Figure 2.13). To be consistent with ELF- π orbitals, the partial double bonds always preferentially locate at embedded positions in the Kekulé π -sextet to achieve maximum of six-electron six-member ring. For instance, the privileged Lewis structure of phenanthrene has three six-electron six-member rings, whereas the unfavorable Lewis structure has only two. On the other hand, the privileged Lewis structure of triphenylene has four six-electron six-member rings, whereas the unfavorable Lewis structure has only three. In the case of coronene the privileged Lewis structure of coronene has six six-electron six-member rings, whereas the unfavorable Lewis structure has only four. It is worth emphasizing that the privileged Lewis structure is not used to replace the Clar's structure but as its complement to predict the bonding and antibonding characteristics of the Kekulé π -sextet on the Clar's structure.

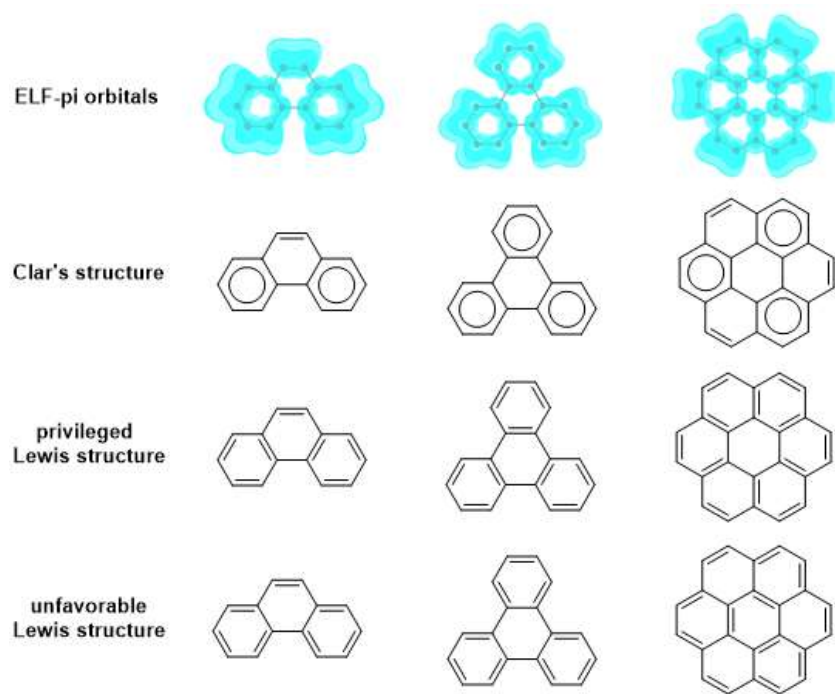


Figure 2.13 The privileged Lewis structure of phenanthrene, triphenylene and coronene.

2.5 Conclusion

In conclusion, comprehensive electronic structures and properties of phenanthrene and its sixteen BN analogues have been investigated in a systematic manner using reliable computational methods. The Mayer bond order analysis indicates that the BN bond plays more of an approximate single bond role in BN-doped polycyclic aromatic hydrocarbons (PAHs). A statistical method of significant difference, the Clar's structure model and pi-electron localized function (ELF-pi) orbitals are employed to reveal the structure-property correlation of BN/CC bond replacement. Large number of frontier molecular orbitals and optical gaps of a series of typical PAHs including naphthalene, anthracene, tetracene, pyrene, triphenylene, perylene, coronene and their BN analogues have been investigated to verify and improve the preliminary empirical principle. The widely applicable empirical principles have been proposed to reveal the influence of the BN bond positioning on HOMO-LUMO gaps and optical gaps. Specifically, The BN analogue which BN bond is located at CC single bond position of the arene scaffold has the smallest HOMO-LUMO gap and the smallest lower optical gap, the BN analogue which BN bond is located at CC double bond position of the arene scaffold has a slightly larger HOMO-LUMO gap and slightly higher optical gap, the BN analogue which BN bond is located at partial double bond position has a slightly smaller HOMO-LUMO gap and a slightly lower optical gap, the BN analogue which BN bond is located partial single bond position has a significantly smaller HOMO-LUMO gap and a significantly lower optical gap. The BN analogues which BN bonds are located at same position with opposite orientations have similar HOMO-LUMO gaps and optical gaps. Furthermore, BN doping can effectively tune the diradical character of acene. Based on our adscitious Clar's rule, it will be very easy to identify the four different positions in polycyclic aromatic hydrocarbons described in the empirical principle without any calculations, which should potentially contribute to further development of BN-doped polycyclic aromatic hydrocarbons for potential applications in material science.

En conclusion, les structures électroniques et les propriétés du phénanthrène et de ses seize analogues BN ont été étudiées de manière systématique à l'aide de différentes méthodes de calcul. L'analyse de l'ordre des liaisons de Mayer indique que la liaison BN joue davantage le rôle d'une liaison simple approximative dans les hydrocarbures aromatiques polycycliques (HAP) dopés au BN. Une méthode statistique de différence significative, le modèle de structure de Clar et les orbitales de fonction localisée pi-électron (ELF-pi) sont utilisés pour révéler la corrélation structure-propriété du remplacement de la liaison BN/CC. Un grand nombre d'orbitales moléculaires frontières et de lacunes optiques d'une série de HAP typiques, y compris le naphthalène, l'anthracène, le tétracène, le pyrène, le triphénylène, le pérylène, le coronène et leurs analogues BN ont été étudiés pour vérifier et améliorer le principe empirique préliminaire. Les principes empiriques largement applicables ont été proposés pour estimer l'influence de la position de la liaison BN sur les écarts HOMO-LUMO et les écarts optiques. Plus précisément, l'analogue du BN dont la liaison BN est située en position de liaison simple CC de l'échafaudage arène présente l'écart HOMO-LUMO le plus faible et l'écart optique le plus bas, l'analogue du BN dont la liaison BN est située en position de liaison double CC de arène, présente un écart HOMO-LUMO légèrement plus important et un écart optique légèrement plus élevé, l'analogue du BN dont la liaison BN est située en position de double liaison partielle présente un écart HOMO-LUMO légèrement plus faible et un écart optique légèrement plus faible, l'analogue du BN dont la liaison BN est située en position de simple liaison partielle présente un écart HOMO-LUMO nettement plus faible et un écart optique nettement plus faible. Les analogues du BN dont les liaisons BN sont situées à la même position avec des orientations opposées ont des écarts HOMO-LUMO et des écarts optiques similaires. En outre, le dopage au BN peut effectivement ajuster le caractère diradical de l'acène. Sur la base de notre règle de Clar, il sera très facile d'identifier les quatre positions différentes dans les hydrocarbures aromatiques polycycliques décrits dans le principe empirique sans aucun calcul, ce qui devrait potentiellement contribuer à la poursuite du développement d'hydrocarbures aromatiques polycycliques dopés au BN pour des applications potentielles en science des matériaux.

Appendix

Naphthalene (double bond). Unlike phenanthrene, the Clar's structure of naphthalene has a migrating π -sextet which is different to discern π orbitals distribution (Figure 2.15). However, the ELF-pi orbitals of naphthalene have a clear illustration that C1-C2, C3-C4, C5-C6, C7-C8 and C9-C10 have double bond character. BN-1,2-naphthalene and BN-2,1-naphthalene have a same HOMO-LUMO gap (4.99 eV) which are slightly higher than all-carbon naphthalene (4.80 eV).

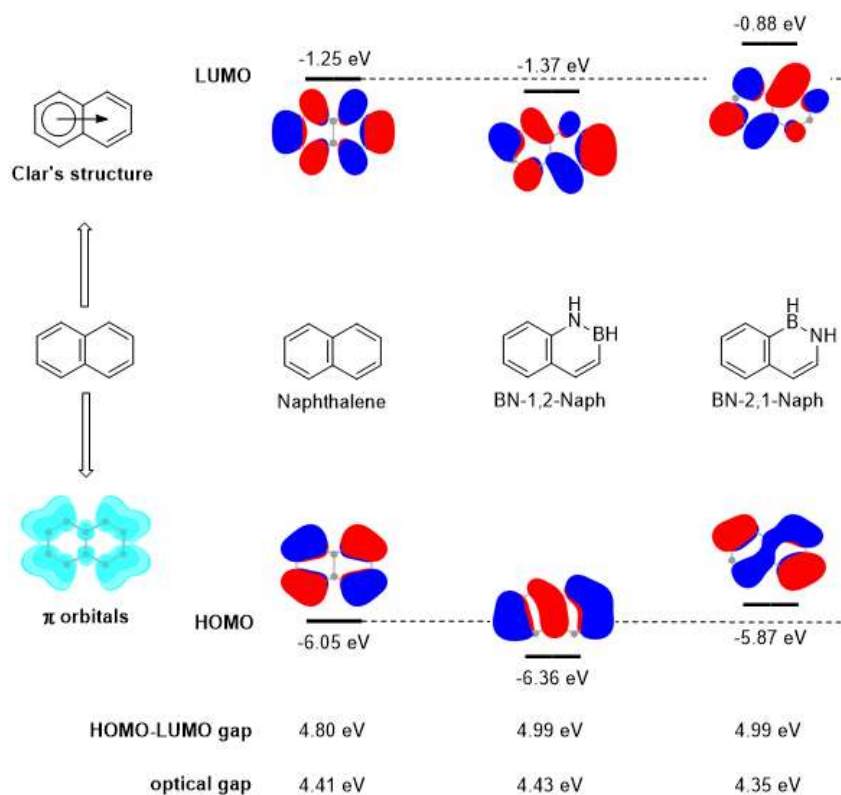


Figure 2.15. The Clar's structure and ELF-pi orbitals of naphthalene as well as HOMO LUMO isosurfaces, gap and optical gap of naphthalene, BN-1,2-naphthalene and BN-2,1-naphthalene. All calculations have been carried out at B3LYP/6-311(d,p) level.

Anthracene (double bond). The Clar's structures of anthracene and all other acenes have a migrating π -sextet. From the ELF-pi orbitals of anthracene (Figure 2.16), four localized pi-bonds are located in two external rings, the middle six-member ring has double three-center three-pi-electron systems which are different with the aromatic six-member ring of

phenanthrene. Anthracene also has two BN/CC replaced BN analogues of BN-1,2-anthracene and BN-2,1-anthracene. The HOMO-LUMO gap and optical gap of both two BN anthracene analogues are slightly higher than anthracene.

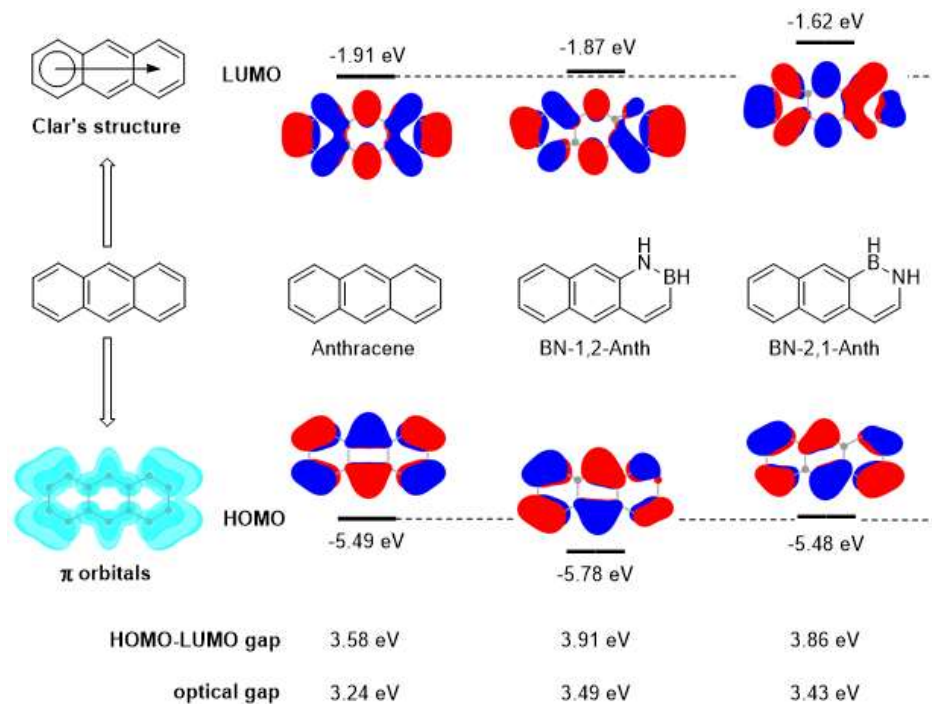


Figure 2.16. The Clar's structure and ELF- π orbitals of anthracene as well as HOMO LUMO isosurfaces, gap and optical gap of anthracene, BN-1,2-anthracene and BN-2,1-anthracene. All calculations have been carried out at B3LYP/6-311(d,p) level.

Tetracene (double bond). From the ELF- π orbitals of tetracene (Figure 2.17), there are also four localized π -bonds in two external rings, the middle two six-member rings have double zig-zag five-center five- π -electron systems. Apparently, with increasing ring number of acene, the chain of zig-zag multi-center multi- π -electron also grow. The HOMO-LUMO gap and the optical gap of both two BN tetracene analogues are slightly higher than all-carbon tetracene.

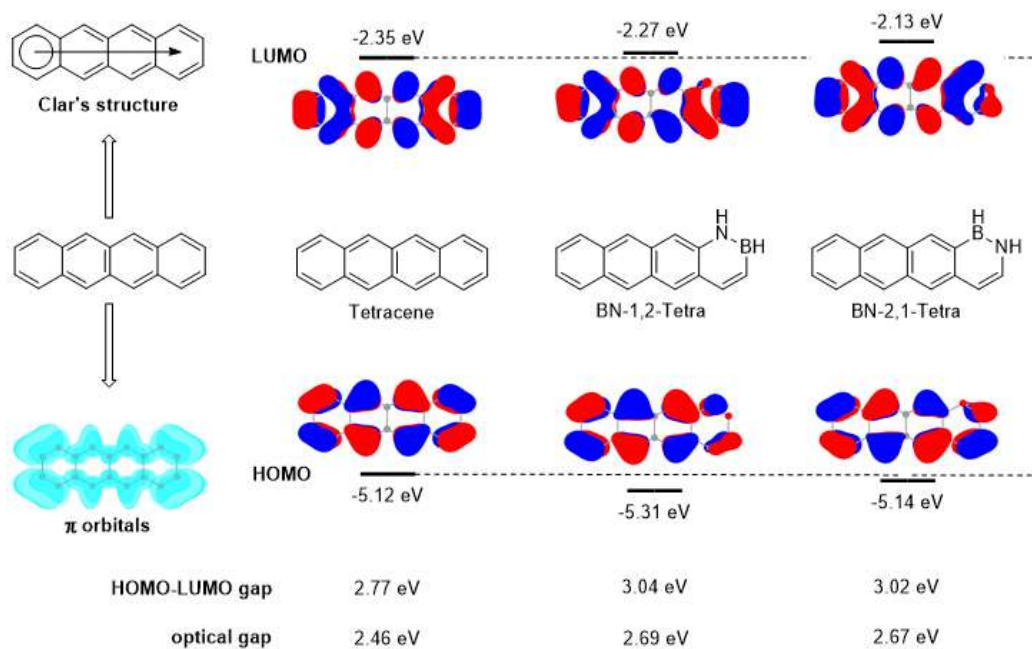


Figure 2.17. The Clar's structure and ELF- π orbitals of tetracene as well as HOMO LUMO isosurfaces, gap and optical gap of tetracene, BN-1,2-tetracene and BN-2,1- tetracene. All calculations have been carried out at B3LYP/6-311(d,p) level.

Pyrene (double bond). The Clar's structure of pyrene shows that the framework of pyrene consists of two single-bonded aromatic six-membered rings and two double-bond bridges (Figure 2.18). The ELF- π orbitals of pyrene also display similar π orbitals distribution. The only one BN/C=C replaced BN analogue of pyrene shows a slightly higher energy on HOMO-LUMO gap and optical gap.

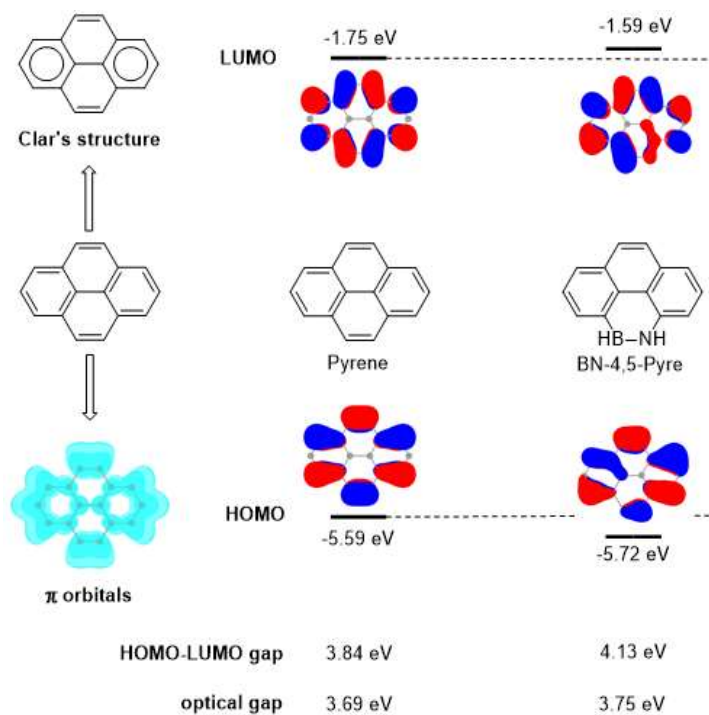


Figure 2.18. The Clar's structure and ELF- π orbitals of pyrene as well as HOMO LUMO isosurfaces, gap and optical gap of pyrene, BN-1,2-pyrene and BN-2,1-pyrene. All calculations have been carried out at B3LYP/6-311(d,p) level.

Perylene (double bond). From the Clar's structure and the ELF- π orbitals we see that perylene is composed of two parallel naphthalene connected by two single bonds (Figure 2.19). Therefore, the π orbitals distributions of these two parts are very similar to naphthalene. Perylene has four BN/CC double bond replaced BN analogues including BN-2,3-perylene, BN-3,2-perylene, BN-6,6a-perylene and BN-6a,6-perylene, while all these BN analogues have slightly higher energies than all-carbon perylene on HOMO-LUMO gap and optical gap. Furthermore, another two displayed isosteres BN-3a,3b-perylene and BN-3b,3a-perylene also have slightly higher energies in spite of less π -bonding character of C3a-C3b bond.

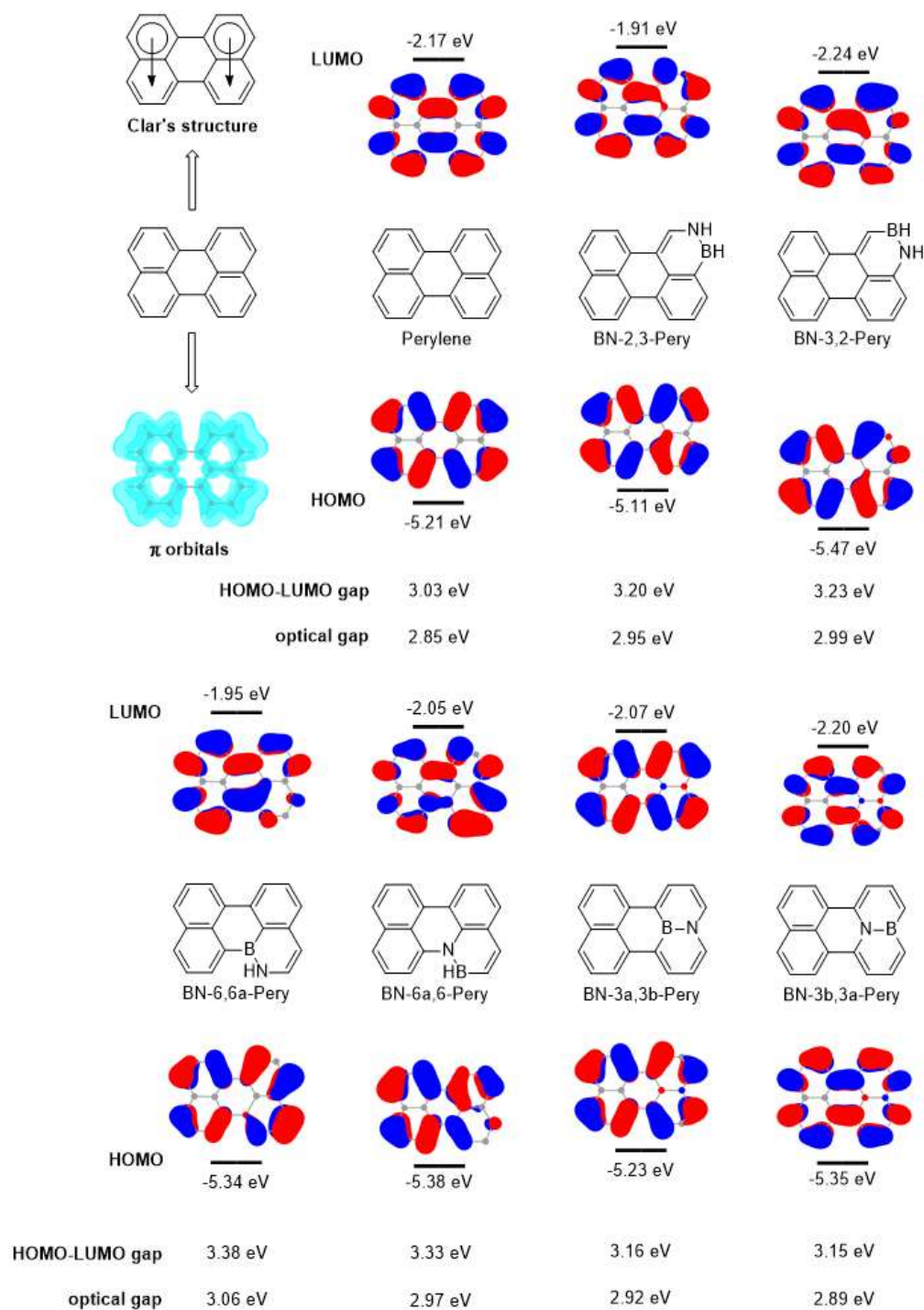


Figure 2.19. The Clar's structure and ELF- π orbitals of perylene as well as HOMO, LUMO isosurfaces, gap and optical gap of perylene, BN-1,2-perylene and BN-2,1-perylene. All calculations have been carried out at B3LYP/6-311(d,p) level.

Naphthalene (single bond). From the ELF- π orbitals of naphthalene (Figure 2.20), the single

bond position included C1-C9, C2-C3, C4-C10, C5-C10, C6-C7 and C8-C9 bonds. Naphthalene has three BN/CC single bond replaced BN analogues including BN-1,9-naphthalene, BN-9,1-naphthalene, which have much lower HOMO-LUMO gap and optical gap than all-carbon naphthalene. All calculations have been carried out at B3LYP/6-311(d,p) level.

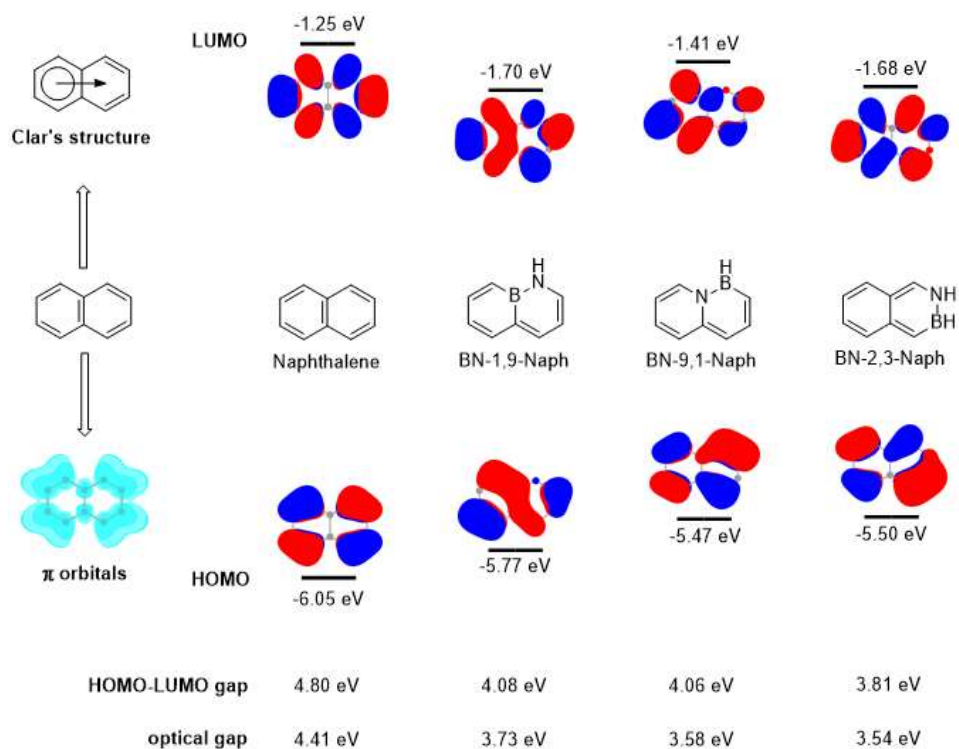


Figure 2.20. The Clar's structure and ELF- π orbitals of naphthalene as well as HOMO LUMO isosurfaces, gap and optical gap of naphthalene, BN-1,9-naphthalene, BN-9,1-naphthalene and BN-2,3-naphthalene. All calculations have been carried out at B3LYP/6-311G(d,p) level.

Anthracene (single bond). Anthracene also has three BN/CC single bond replaced BN analogues including BN-1,9a-anthracene, BN-9a,1-anthracene, BN-2,3-anthracene (Figure 2.21). Both the HOMO-LUMO gap and optical gap of these three BN anthracene isosteres are much lower than the all-carbon analogue.

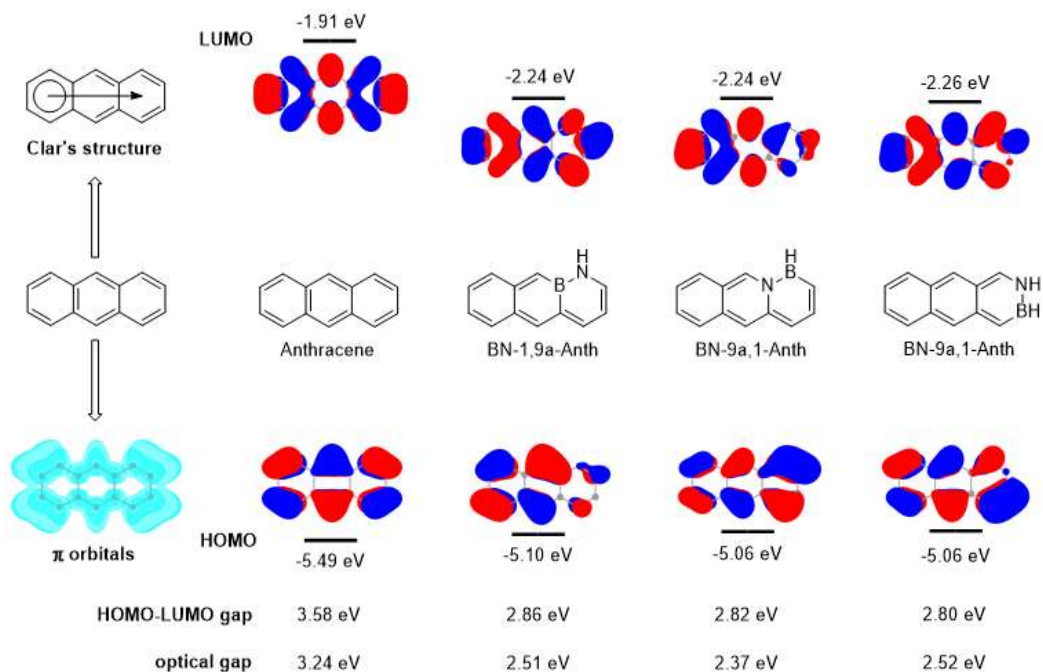


Figure 2.21 The Clar's structure and ELF- π orbitals of anthracene as well as HOMO, LUMO isosurfaces, gap and optical gap of anthracene, BN-1,9a-anthracene, BN-9a,1-anthracene and BN-2,3-anthracene. All calculations have been carried out at B3LYP/6-311(d,p) level.

Tetracene (single bond). Based on the ELF- π orbitals of naphthalene, anthracene and tetracene, the single bond positions of all acenes always located in the external rings, thus tetracene also has three BN/CC single bond replaced BN analogues including BN-1,12a-tetracene, BN-12a,1-tetracene, BN-2,3-tetracene (Figure 2.22), which HOMO-LUMO gap and optical gap are much lower than the all-carbon analogue. It is conceivable that, with increasing of the acene length, the BN/CC substitution effect will decrease.

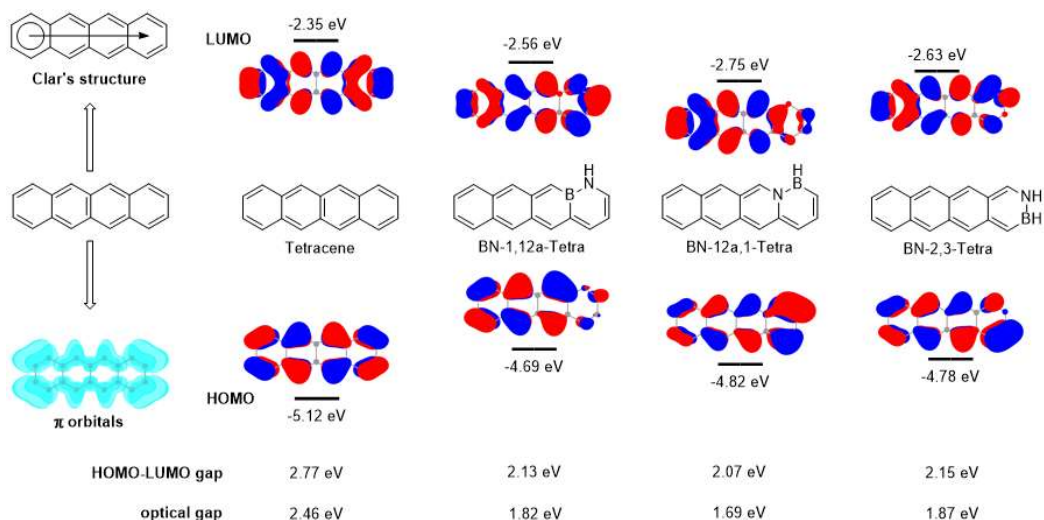


Figure 2.22. The Clar's structure and ELF- π orbitals of tetracene as well as HOMO LUMO isosurfaces, gap and optical gap of tetracene, BN-1,12a-tetracene, BN-12a,1-tetracene and BN-2,3-tetracene. All calculations have been carried out at B3LYP/6-311(d,p) level.

Pyrene (single bond). According to the Clar's structure of pyrene, there are five single bond positions in the molecular scaffold. Taking account to the symmetry, pyrene should have three BN/CC single bond replaced BN analogues including BN-5a,5-pyrene, BN-5,5a-pyrene and BN-3b,5b-pyrene (Figure 2.23). BN-5a,5-pyrene and BN-5,5a-pyrene exhibit dramatically reduced HOMO-LUMO gaps and optical gaps. However, the HOMO-LUMO gap of BN-3b,5b-pyrene is slightly lower than pyrene in spite of the significantly decreased optical gap. It is supposed to be that the position where BN is located in pyrene does not overlap with HOMO or LUMO, which is very similar with all-carbon pyrene. The reason why BN-3b,5b-pyrene has a significantly decreased optical gap is supposed to be that the excitation of BN-3b,5b-pyrene from ground state to the first excited state can be mainly described by multi-transition orbitals including HOMO-1 \rightarrow LUMO and HOMO \rightarrow LUMO+1.

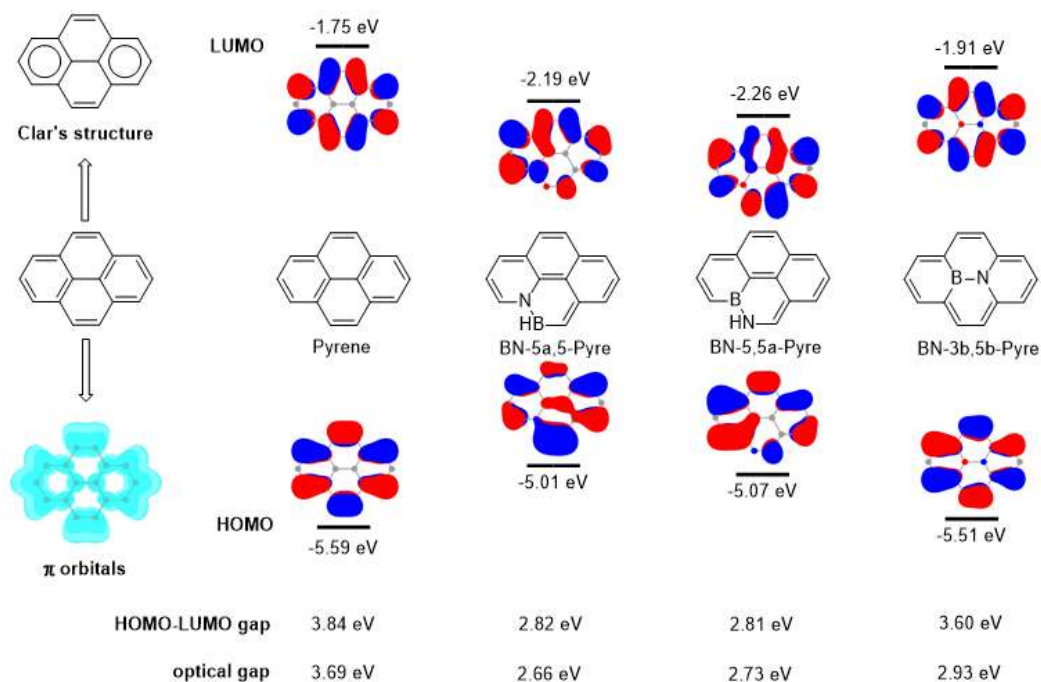


Figure 2.23 The Clar's structure and ELF- π orbitals of pyrene as well as HOMO LUMO isosurfaces, gap and optical gap of pyrene, BN-5a,5-pyrene, BN-5,5a-pyrene and BN-3b,5b-pyrene. All calculations have been carried out at B3LYP/6-311(d,p) level.

Triphenylene (single bond). Triphenylene is composed of three single-bonded benzene from the Clar's structure which is consistent with the ELF- π orbitals (Figure 2.24). The only one BN/CC single bond replaced BN analogue, namely BN-1a,12a-triphenylene, has a dramatically reduced HOMO-LUMO gap and optical gap.

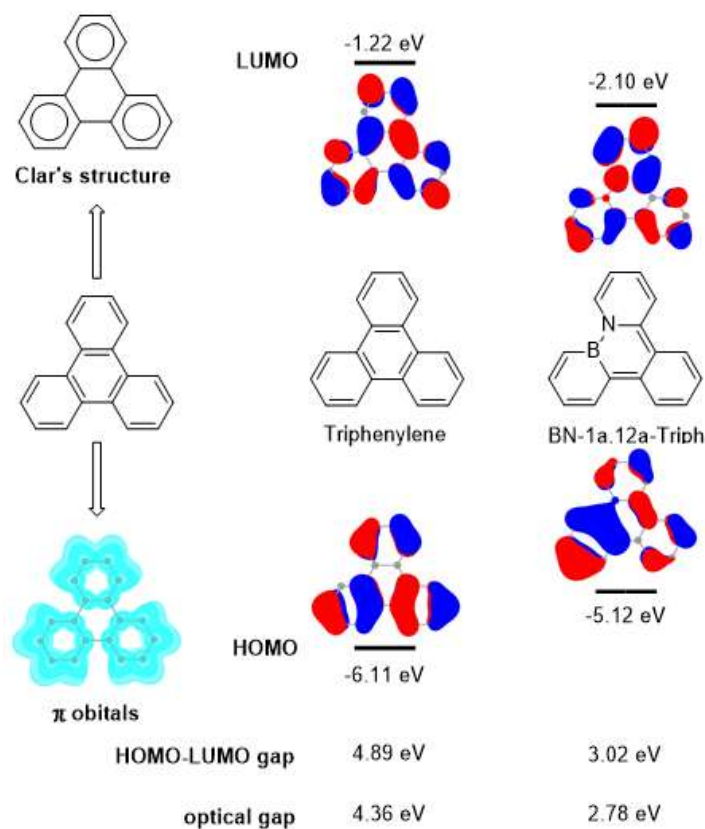


Figure 2.24. The Clar's structure and ELF- π orbitals of triphenylene as well as HOMO LUMO isosurfaces, gap and optical gap of triphenylene and BN-1a,12a-triphenylene. All calculations have been carried out at B3LYP/6-311(d,p) level.

Perylene (single bond and partial single bond). Perylene in total has seven BN/C-C replaced BN analogues including BN-6a,6b-perylene, BN-1,2-perylene, BN-2,1-perylene, BN-3,3a-perylene, BN-3a,3-perylene, BN-6,6a-perylene and BN-6a,6-perylene (Figure 2.25). Among all these BN analogues, only BN-6a,6b-perylene has a dramatically reduced HOMO-LUMO gap and optical gap, the rest isomers have only slight decrease on the energies of HOMO-LUMO gaps and optical gaps. We mentioned previously that the π orbitals distribution of perylene looks like two connected naphthalenes. From the ELF- π orbitals, perylene has two deformed naphthalene-like π orbitals distributions because of the mutual pi-orbital repulsion, which enable the original single-bond position of naphthalene to have partial π -bonding characters.

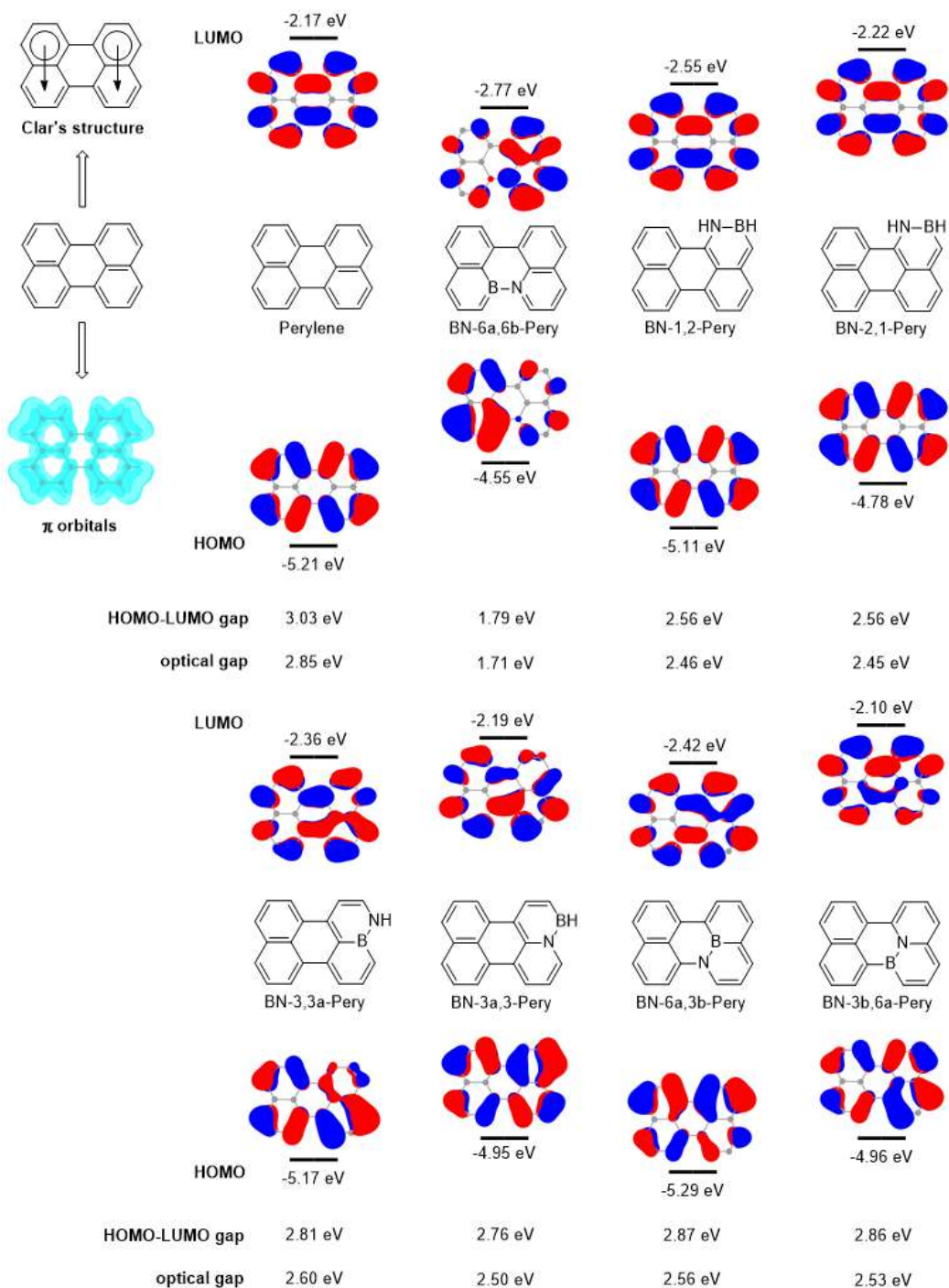


Figure 2.25. The Clar's structure and ELF- π orbitals of perylene as well as HOMO LUMO isosurfaces, gap and optical gap of perylene, BN-6a,6b-perylene, BN-1,2-perylen, BN-2,1-perylene, BN-3,3a-perylene, BN-3a,3-perylene, BN-6,6a-perylene and BN-6a,6-perylene. All calculations have been carried out at B3LYP/6-311(d,p) level.

Perylene (partial single bond and partial double bond). From the ELF- π orbitals of

triphenylene (Figure 2.26), BN-1,2-triphenylene, BN-2,1-triphenylene and BN-1a,4a-triphenylene which BN bond located at partial double bond positions have slightly lower energies than all-carbon triphenylene on HOMO-LUMO gap and optical gap, whereas BN-1,1a-triphenylene, BN-1a,1-triphenylene and BN-2,3-triphenylene which BN bond located at partial single bond positions have significantly lower energies than all-carbon triphenylene on HOMO-LUMO gap and optical gap.

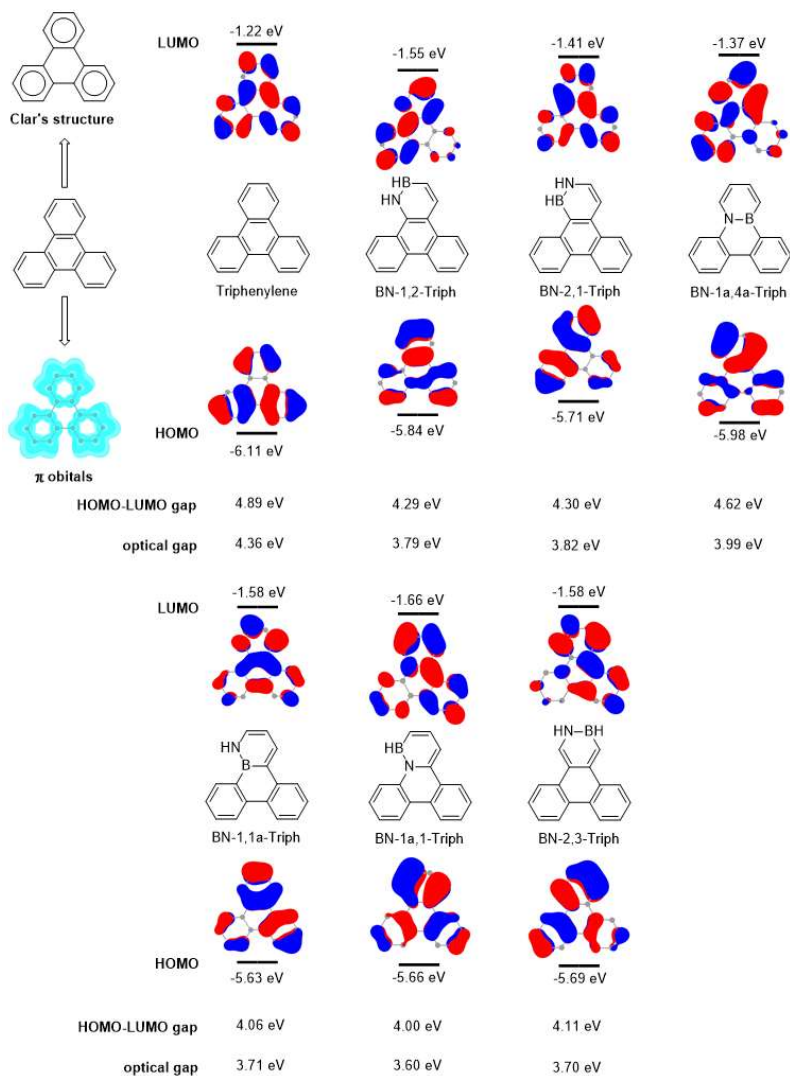


Figure 2.26 The Clar's structure and ELF- π orbitals of triphenylene as well as HOMO LUMO isosurfaces, gap and optical gap of triphenylene, BN-1,2-triphenylene, BN-2,1-triphenylene, BN-1a,4a-triphenylene, BN-1,1a-triphenylene, BN-1a,1-triphenylene and BN-2,3-triphenylene. All calculations have been carried out at B3LYP/6-311(d,p) level.

Pyrene (partial single bond and partial double bond). From the ELF- π orbitals of pyrene (Figure 2.27), three-center bond C1-C2-C3, C10a-C3b-C3a, C6-C7-C8 and C5a-C5b-C8a have partial double bond characteristic, and C1-C10a, C3-C3a, C5a-C6 and C8-C8a have partial single bond characteristic due to the symmetry of pyrene. BN-1,2-pyrene, BN-2,1-pyrene, BN-3a,3b-pyrene and BN-3b,3a-pyrene which BN bond located at partial double bond positions have slightly lower energies than all-carbon pyrene on HOMO-LUMO gap and optical gap. Interestingly, BN/CC partial single bond replaced isomers have higher HOMO-LUMO gap and lower optical gap. The possible reason is that the partial single bond positions are overlapped with π -bonding orbitals, which have same behavior with double bond, but the first excitation does not relate to the HOMO->LUMO transition.

Coronene (partial single bond and partial double bond). From the Clar's structure, coronene also has migrating π -sextets. The ELF- π orbitals show coronene is composed of six identical aromatic rings (Figure 2.28). BN-1,2- coronene, BN-2a,2b-coronene and BN-2b,2a-coronene which BN bond locate at partial double positions have slightly lower energies than all-carbon coronene on HOMO-LUMO gaps and optical gaps, BN-2,2a-coronene, BN-2a,2-coronene and BN-12b,2b-coronene which BN bond locate at partial single bond positions have significantly lower energies than all-carbon coronene on HOMO-LUMO gap and optical gap.

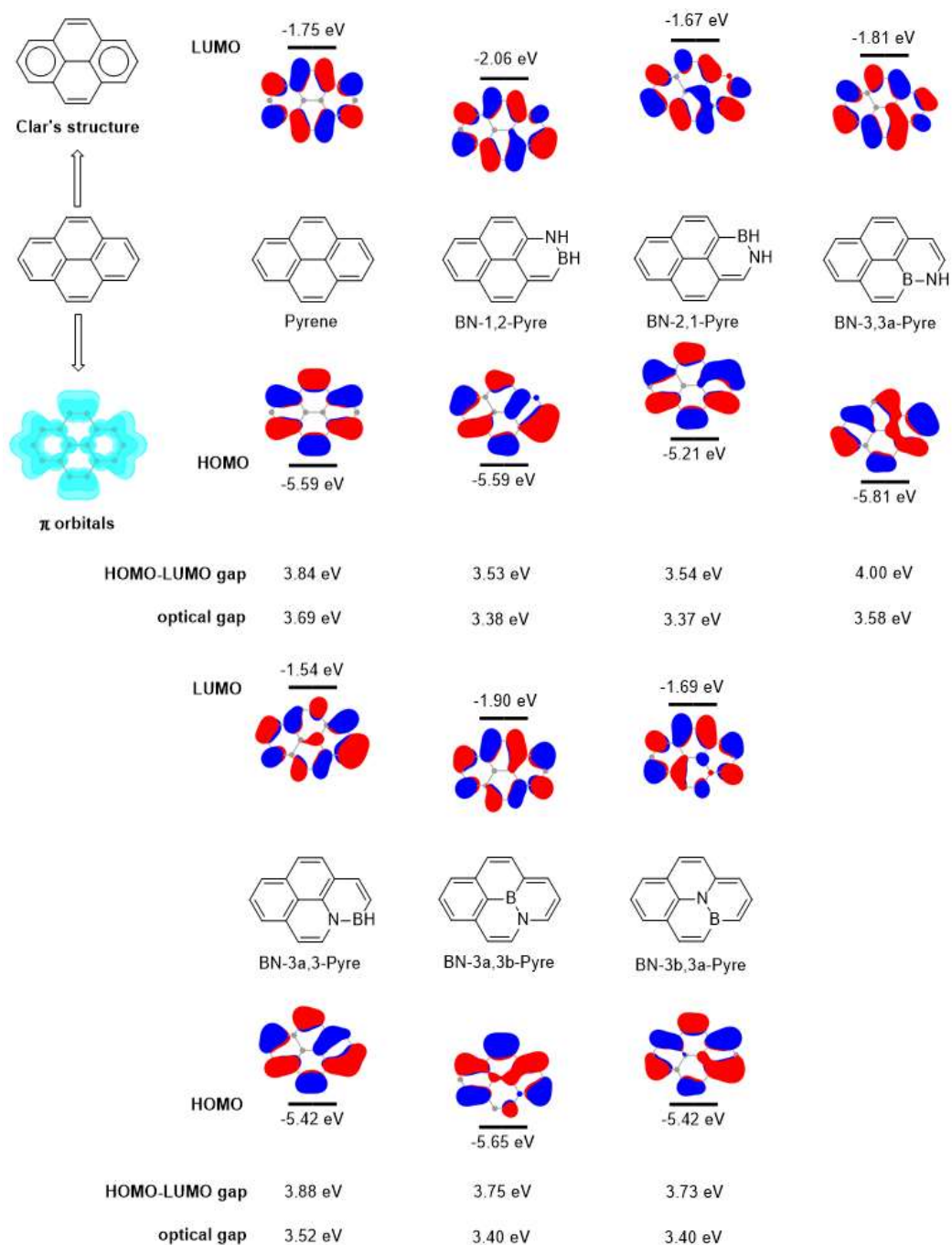


Figure 2.27 The Clar's structure and ELF- π orbitals of pyrene as well as HOMO LUMO isosurfaces, gap and optical gap of pyrene, BN-1,2-pyrene, BN-2,1-pyrene, BN-3,3a-pyrene, BN-3a,3-pyrene, BN-3a,3b-pyrene and BN-3b,3a-pyrene. All calculations have been carried out at B3LYP/6-311(d,p) level.

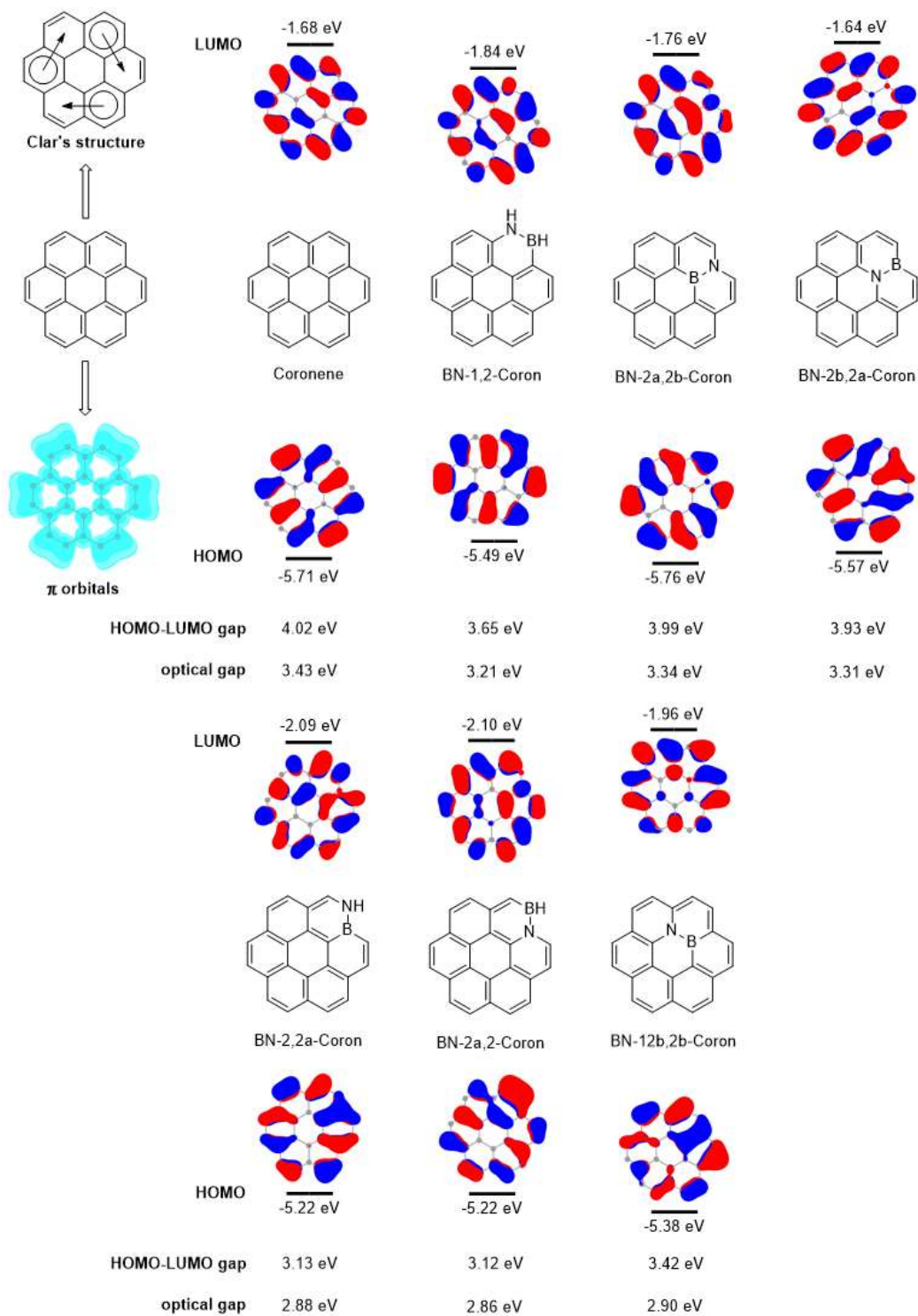


Figure 2.28 The Clar's structure and ELF- π orbitals of coronene as well as HOMO LUMO isosurfaces, gap and optical gap of coronene, BN-1,2-coronene, BN-2a,2b-coronene, BN-2b,2a-coronene, BN-2,2a-coronene, BN-2a,2-coronene and BN-12,2b-coronene.

Unlike non-linear arenes, acene displays an unusual behavior on BN doping effects. We notice that the first excitation of acene such as naphthalene, anthracene, tetracene and pentacene can be described by single HOMO > LUMO transition, which means the distribution of π -bonding orbital in HOMO will play a role in the energy changes of HOMO-LUMO gap and optical gap by doping a BN bond. From the ELF-pi orbitals of anthracene (Figure 2.29), C4-C4a, C10-C10a, C9-C8a and C9-C9a have partial single bond characteristic if we consider that C9 and C10 are independent radical. With the overlap of π -bonding orbitals, the energy of BN-9,9a-anthracene and BN-9a,9-anthracene have a relatively high energy of HOMO-LUMO gap and optical gap. Likewise, BN-10a,11-tetracene and BN-11,11a-tetracene have higher energy than all-carbon tetracene on HOMO-LUMO gap and optical gap (Figure 2.30). When the partial double bond position completely separated from HOMO is occupied by BN, the resulting BN isomer exhibits higher energy such as BN-9,10-naphthalene and BN-11a,5a-tetracene (Figure 2.31).

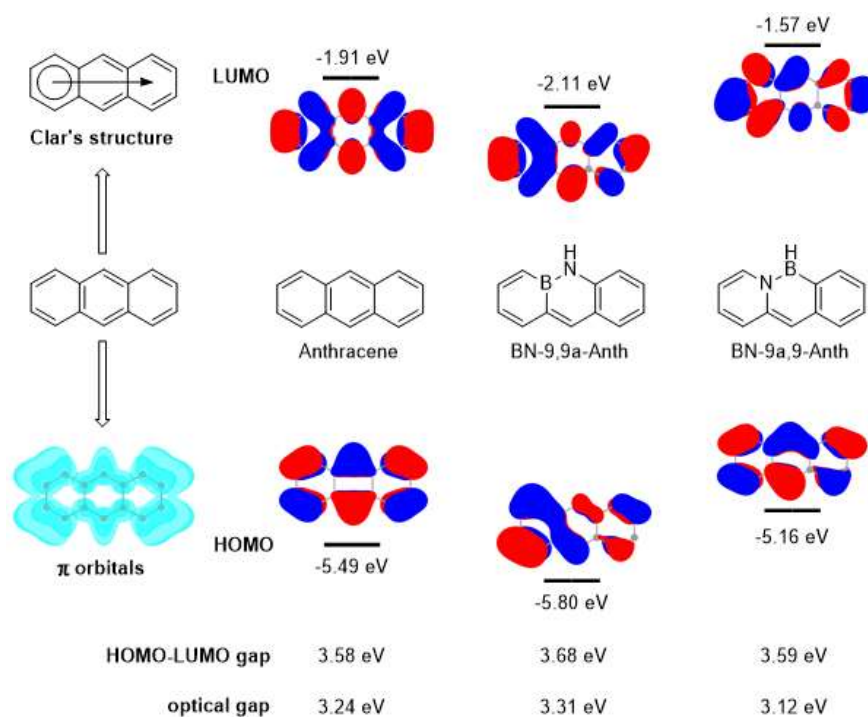


Figure 2.29. The Clar's structure and ELF-pi orbitals of anthracene as well as HOMO LUMO isosurfaces, gap and optical gap of anthracene, BN-9,9a-anthracene and BN-9a,9-anthracene. All calculations have been carried out at B3LYP/6-311(d,p) level.

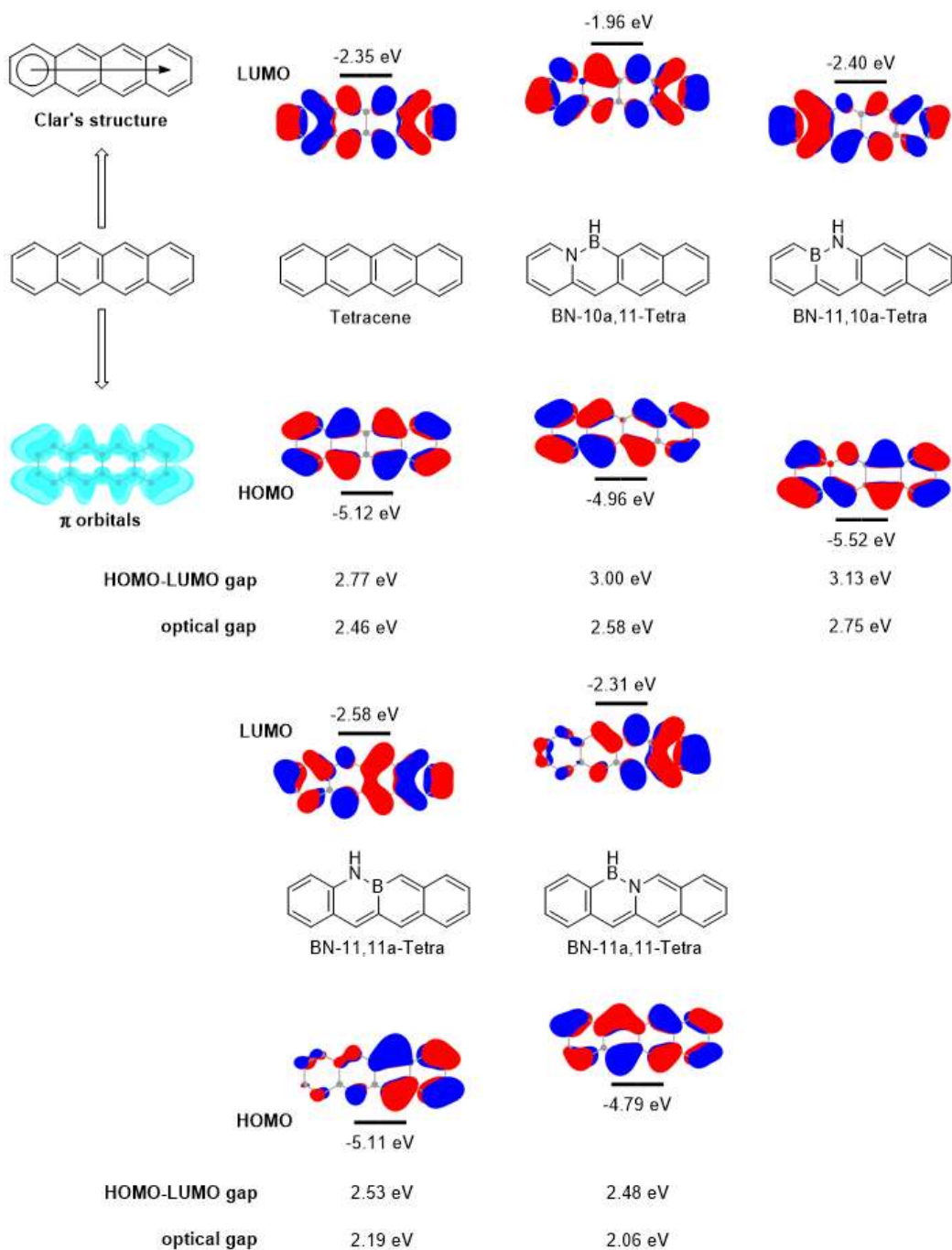


Figure 2.30. The Clar's structure and ELF- π orbitals of tetracene as well as HOMO LUMO isosurfaces, gap and optical gap of tetracene, BN-10a,11-tetracene, BN-11,10a-tetracene, BN-11,11a-tetracene and BN-11a,11-tetracene. All calculations have been carried out at B3LYP/6-311(d,p) level.

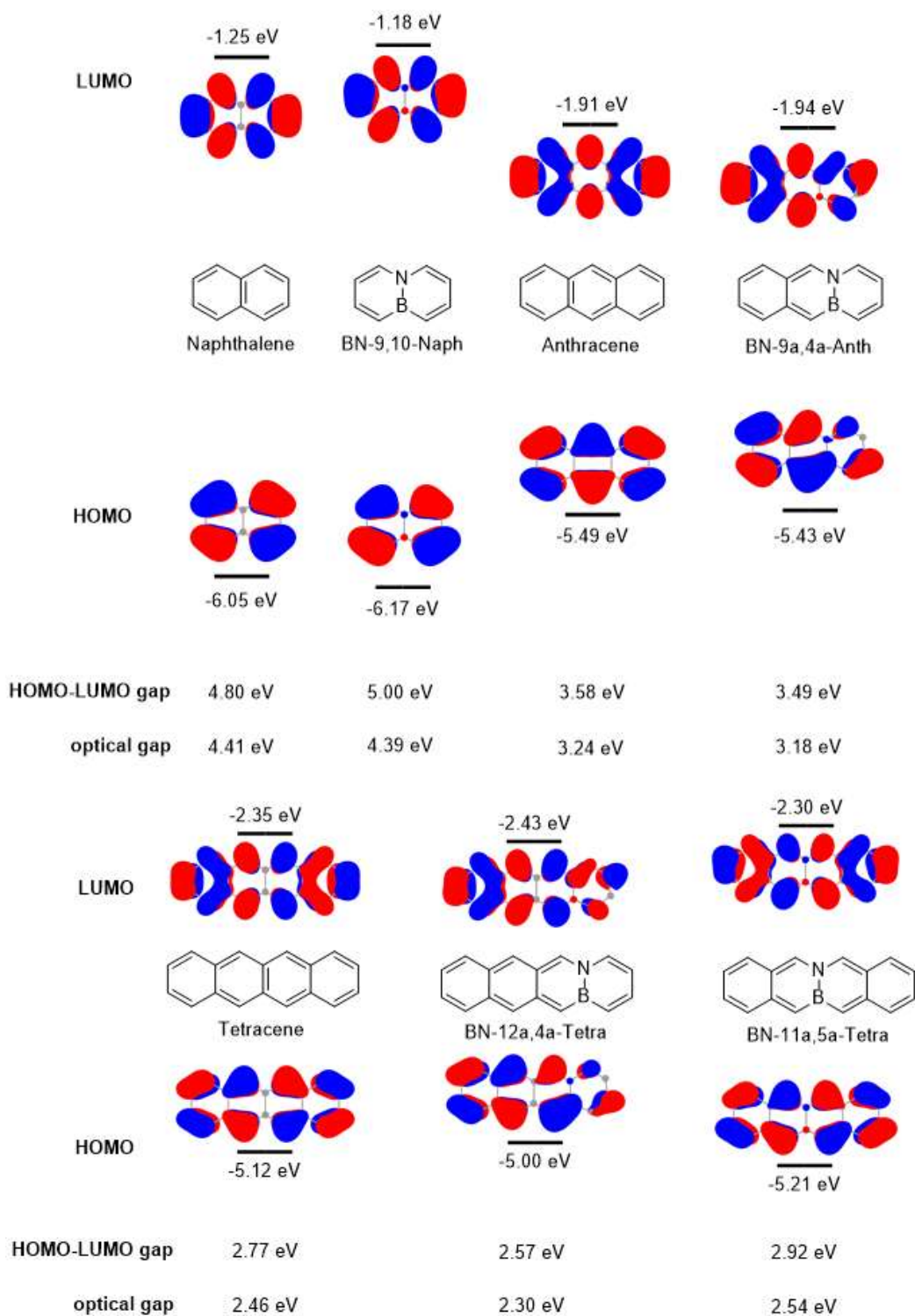


Figure 2.31 The HOMO LUMO isosurfaces, gap and optical gap of naphthalene, BN-9,10-naphthalene, anthracene, BN-9a,4a-anthracene, tetracene, BN-12a,4a-tetracene and BN-11a,5a-tetracene. All calculations have been carried out at B3LYP/6-311(d,p) level.

Table. 2.11 Optical gap differences between PAHs and their BN/CC double bond replaced, BN/CC single bond related analogues. All calculations have been carried out at B3LYP/6-311G(d,p) level.

Double bond	E_{opt} (eV)	E_{diff} (eV)	Single bond	E_{opt} (eV)	E_{diff} (eV)
BN-1,2-Naph	4.43	0.02	BN-2,3-Naph	3.54	-0.87
BN-2,1-Naph	4.35	-0.06	BN-1,9-Naph	3.73	-0.68
BN-9,10-Naph	4.39	-0.02	BN-9,1-Naph	3.58	-0.83
BN-1,2-Anth	3.49	0.25	BN-23-Anth	2.52	-0.72
BN-2,1-Anth	3.43	0.19	BN-19a-Anth	2.51	-0.73
BN-9,9a-Anth	3.31	0.07	BN-9a,1-Anth	2.37	-0.87
BN-9a,9-Anth	3.12	-0.12	BN-2,3-Tetra	1.87	-0.59
BN-9a,4a-Anth	3.18	-0.06	BN-11,2a-Tetra	1.82	-0.64
BN-1,2-Tetra	2.69	0.23	BN-12a,1-Tetra	1.69	-0.77
BN-2,1-Tetra	2.67	0.21	BN-8a,9-Phen	3.05	-0.94
BN-10a,11-Tetra	2.58	0.12	BN-9,8a-Phen	3.12	-0.87
BN-11,10a-Tetra	2.75	0.29	BN-4a,4b-Phen	3.19	-0.8
BN-11a,5a-Tetra	2.54	0.08	BN-1a,12a-Triph	2.78	-1.58
BN-9,10-Phen	4.21	0.22	BN-5,5a-Pyre	2.73	-0.96
BN-4,5-Pyre	3.75	0.06	BN-5a,5-Pyre	2.66	-1.03
BN-2,3-Pery	2.95	0.1	BN-3b,5b-Pyre	2.93	-0.76
BN-3,2-Pery	2.99	0.14	BN-6a,6b-Pery	1.71	-1.14
BN-6,6a-Pery	3.06	0.21			
BN-6a,6-Pery	2.97	0.12			
BN-3a,3b-Pery	2.92	0.07			
BN-3b,3a-Pery	2.89	0.04			

Table. 2.12 Optical gap differences between PAHs and their BN/CC partial double bond replaced, BN/CC partial single bond related analogues. All calculations have been carried out at B3LYP/6-311G(d,p) level.

Partial double bond	E _{opt} (eV)	E _{diff} (eV)	Partial single bond	E _{opt} (eV)	E _{diff} (eV)
BN-11,11a-Tetra	2.19	-0.27	BN-2,3-Phen	3.57	-0.42
BN-11a,11-Tetra	2.06	-0.4	BN-3,2-Phen	3.65	-0.34
BN-12a,4a-Tetra	2.3	-0.16	BN-4,4a-Phen	3.59	-0.4
BN-1,2-Phen	3.91	-0.08	BN-4a,4-Phen	3.48	-0.51
BN-2,1-Phen	3.84	-0.15	BN-1,10a-Phen	3.71	-0.28
BN-3,4-Phen	3.93	-0.06	BN-10a,1-Phen	3.61	-0.38
BN-4,3-Phen	3.89	-0.1	BN-2,3-Triph	3.7	-0.66
BN-4a,10a-Phen	4.04	0.05	BN-1,1a-Triph	3.71	-0.65
BN-10a,4a-Phen	4.1	0.11	BN-1a,1-Triph	3.6	-0.76
BN-1,2-Triph	3.79	-0.57	BN-2,2a-Coron	2.88	-0.55
BN-2,1-Triph	3.82	-0.54	BN-2a,2-Coron	2.86	-0.57
BN-1a,4a-Triph	3.99	-0.37	BN-12b,2b-Coron	2.9	-0.53
BN-1,2-Pyre	3.38	-0.31	BN-1,2-Pery	2.46	-0.39
BN-2,1-Pyre	3.37	-0.32	BN-2,1-Pery	2.45	-0.4
BN-3,3a-Pyre	3.58	-0.11	BN-3,3a-Pery	2.6	-0.25
BN-3a,3-Pyre	3.52	-0.17	BN-3a,3-Pery	2.5	-0.35
BN-3a,3b-Pyre	3.4	-0.29	BN-6a,3b-Pery	2.56	-0.29
BN-3b,3a-Pyre	3.4	-0.29	BN-3b,6a-Pery	2.53	-0.32
BN-1,2-Coron	3.21	-0.22			
BN-2a,2b-Coron	3.34	-0.09			
BN-2b,2a-Coron	3.31	-0.12			

We find that the homologous bis-BN substituted anthracenes have superimposed effects on HOMO-LUMO gaps and optical gaps. In the case of BN/CC double bond replaced anthracene, bis-BN-1,2,5,6-anthracene shows slightly higher energies than mono-substituted BN-1,2-anthracene on HOMO-LUMO gaps and optical gaps. In the case of BN/CC single bond

replaced anthracene (Figure 2.32), bis-BN-9a,1,5a,5-anthracene has significantly lower energies than mono-substituted BN-9a,1-anthracene on HOMO-LUMO gaps and optical gaps.

The synthesis of bis-BN-1,2,5,6-anthracene and BN-1,2-anthracene were reported by Liu group, they found that neither bis-BN-1,2,5,6-anthracene nor BN-1,2-anthracene had no [4 + 4] dimerization under UV light, on the contrary, anthracene yielded a “butterfly” dimer.^{5d} We consider that this dimerization reaction has relationship with the diradical character of anthracene and BN analogues. It is well known that diradical character of acene enhances with more rings. Based on the method of unrestricted Hartree-Fock (UHF) proposed by Yamaguchi, the diradical character can be defined by y value.²⁷

$$y = 1 - \frac{2T}{1 + T^2}$$

T is the half occupancy difference between HOMO and LUMO, specifically,

$$T = \frac{n_{HOMO} - n_{LUMO}}{2}$$

According to the calculations, bis-BN-1,2,5,6-anthracene has no diradical character while BN-1,2-anthracene has a lower diradical character than anthracene, which is consistent with the fact that these two BN analogues had no [4 + 4] dimerization under UV light. On the contrary, BN/CC single bond replaced bis-BN-9a,1,5a,5-anthracene and BN-9a,1-anthracene have higher diradical character than anthracene, which indicate a feasible [4 + 4] dimerization. As the result, the diradical character of acenes even arenes can be tuning by BN bond doping, which could be potentially applied to singlet fission materials.²⁸

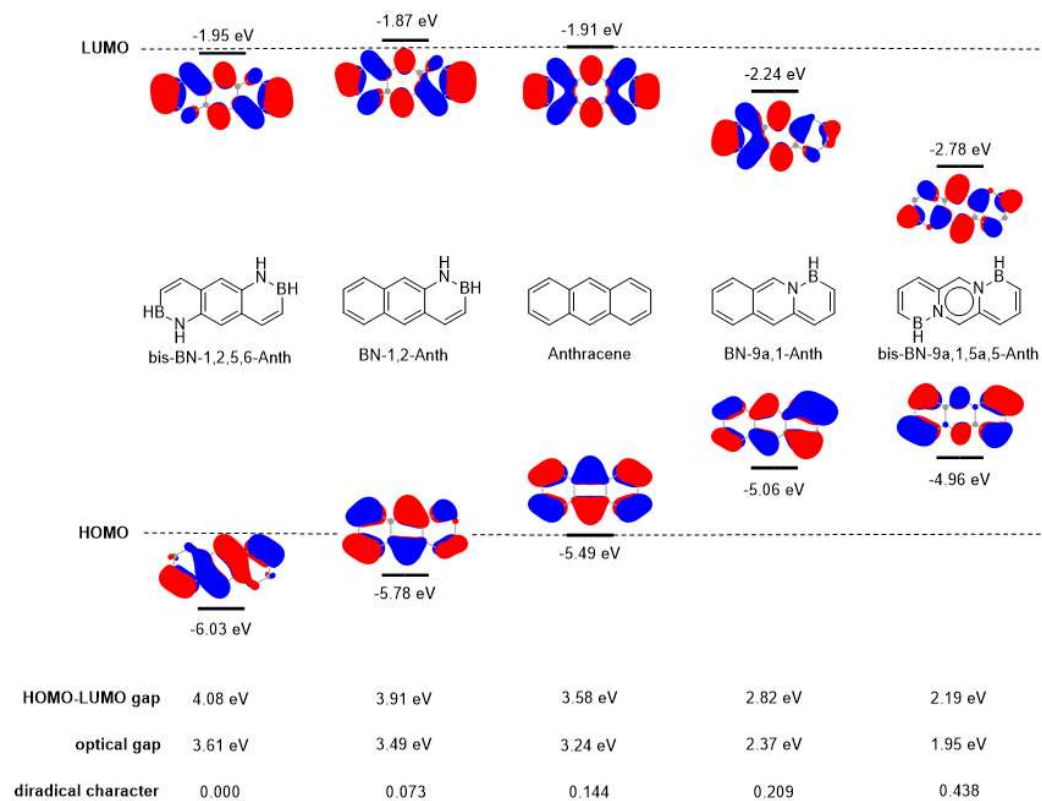


Figure 2.32 The HOMO-LUMO gap, optical gap and diradical character of bis-BN-1,2,5,6-anthracene, BN-1,2-anthracene, anthracene, BN-9a,1-anthracene and bis-BN-9a,1,5a,5-anthracene. All energies have been calculated at B3LYP/6-311G(d,p) level, the diradical characters have been calculated at UHF/6-31G(d,p) level.

Reference

- [1] Dewar, M. J. S.; Kubba, V. P.; Pettit, R. *J. Chem. Soc.* **1958**, 3073–3076.
- [2] Bosdet, M. J. D.; Jaska, C. A.; Piers, W. E.; Sorensen, T. S.; Parvez, M. *Org. Lett.* **2007**, *9*, 1395–1398.
- [3] Zhang, C.; Zhang, L.; Sun, C.; Sun, W.; Liu, X. *Org. Lett.* **2019**, *21*, 3476–3480.
- [4] Liu, Z.; Ishibashi, J. S. A.; Darrigan, C.; Dargelos, A.; Chrostowska, A.; Li, B.; Vasiliu, M.; Dixon, D. A.; Liu, S.-Y. *J. Am. Chem. Soc.* **2017**, *139*, 6082–6085.
- [5] (a) Dewar, M. J. S.; Dietz, R. *J. Chem. Soc.* **1959**, 2728–2730. (b) Dewar, M. J. S.; Jones, R. *J. Am. Chem. Soc.* **1968**, *90*, 2137–2144. (c) Brown, A. N.; Li, B.; Liu, S.-Y. *J. Am. Chem. Soc.* **2015**, *137*, 8932–8935. (d) Ishibashi, J. S. A.; Marshall, J. L.; Mazière, A.; Lovinger, G. J.; Li, B.; Zakharov, L. N.; Dargelos, A.; Graciaa, A.; Chrostowska, A.; Liu, S.-Y. *J. Am. Chem. Soc.* **2014**, *136*, 15414–15421. (e) Tian, D.; Shi, G.; Fan, M.; Guo, X.; Yuan, Y.; Wu, S.; Liu, J.; Zhang, J.; Xing, S.; Zhu, B. *Org. Lett.* **2021**, *23*, 8163–8168. (f) Ishibashi, J. S. A.; Darrigan, C.; Chrostowska, A.; Li, B.; Liu, S.-Y. *Dalton Trans.* **2019**, *48*, 2807–2812. (g) Abengózar, A.; García-García, P.; Sucunza, D.; Frutos, L. M.; Castaño, O.; Sampedro, D.; Pérez-Redondo, A.; Vaquero, J. J. *Org. Lett.* **2017**, *19*, 3458–3461. (h) Valencia, I.; García-García, P.; Sucunza, D.; Mendicuti, F.; Vaquero, J. J. *J. Org. Chem.* **2021**, *86*, 16259–16267. (i) Lu, J.-S.; Ko, S.-B.; Walters, N. R.; Kang, Y.; Sauriol, F.; Wang, S. *Angew. Chem.* **2013**, *125*, 4642–4646.
- [6] Ishibashi, J. S. A.; Dargelos, A.; Darrigan, C.; Chrostowska, A.; Liu, S.-Y. *Organometallics* **2017**, *36*, 2494–2497.
- [7] Stojanović, M.; Baranac-Stojanović, M. *New J. Chem.*, **2018**, *42*, 12968–12976.
- [8] (a) Cížek, J. *Advances in Chemical Physics*, **1969**, *14*, 35 (Wiley Interscience, New York) (b) Purvis, G.; Bartlett, R. *J. Chem. Phys.*, **1982**, *76*, 1910–1918. (c) Scuseria, G.; Janssen, L.; Schaefer, H. *J. Chem. Phys.*, **1988**, *89*, 7382–7387.
- [9] (a) Koch, H.; Jørgensen, P. *J. Chem. Phys.*, **1990**, *93*, 3333–3344. (b) Stanton, J.; Bartlett, R. *J. Chem. Phys.*, **1993**, *98*, 7029–7039. (c) Koch, H.; Kobayashi, R.; Sánchez de Merás, A.; Jørgensen, P. *J. Chem. Phys.*, **1994**, *100*, 4393.
- [10] Gaussian 16, Revision C.01, Frisch, M. J.; Trucks, G. W.; Schlegel, H. B.; Scuseria, G. E.;

Robb, M. A.; Cheeseman, J. R.; Scalmani, G.; Barone, V.; Petersson, G. A.; Nakatsuji, H.; Li, X.; Caricato, M.; Marenich, A. V.; Bloino, J.; Janesko, B. G.; Gomperts, R.; Mennucci, B.; Hratchian, H. P.; Ortiz, J. V.; Izmaylov, A. F.; Sonnenberg, J. L.; Williams-Young, D.; Ding, F.; Lipparini, F.; Egidi, F.; Goings, J.; Peng, B.; Petrone, A.; Henderson, T.; Ranasinghe, D.; Zakrzewski, V. G.; Gao, J.; Rega, N.; Zheng, G.; Liang, W.; Hada, M.; Ehara, M.; Toyota, K.; Fukuda, R.; Hasegawa, J.; Ishida, M.; Nakajima, T.; Honda, Y.; Kitao, O.; Nakai, H.; Vreven, T.; Throssell, K.; Montgomery, J. A., Jr.; Peralta, J. E.; Ogliaro, F.; Bearpark, M. J.; Heyd, J. J.; Brothers, E. N.; Kudin, K. N.; Staroverov, V. N.; Keith, T. A.; Kobayashi, R.; Normand, J.; Raghavachari, K.; Rendell, A. P.; Burant, J. C.; Iyengar, S. S.; Tomasi, J.; Cossi, M.; Millam, J. M.; Klene, M.; Adamo, C.; Cammi, R.; Ochterski, J. W.; Martin, R. L.; Morokuma, K.; Farkas, O.; Foresman, J. B.; Fox, D. J. Gaussian, Inc., Wallingford CT, 2016.

- [11] (a) Hegarty, D.; Robb, M. *Mol. Phys.*, **1979**, *38*, 1795–1812. (b) Eade, R.; Robb, M. *Chem. Phys. Lett.*, **1981**, *83*, 362–368. (c) Klene, M.; Robb, M.; Frisch, M.; Celani, P. *J. Chem. Phys.*, **2000**, *113*, 5653–5665.
- [12] (a) Werner, H.; Knowles, P.; Knizia, G.; Manby, F.; Schütz, M. *WIREs. Comput. Mol. Sci.* **2012**, *2*, 242–253. (b) Werner, H.; Knowles, P. *J. Chem. Phys.*, **1985**, *82*, 5053.
- [13] (a) Becke, A.; *J. Chem. Phys.* **1993**, *98*, 5648–5652. (b) Lee, B.; Yang, W.; Parr, R.; *Phys. Rev. B.* **1988**, *37*, 785–789. (c) Vosko, S.; Wilk, L.; Nusair, M.; *Can. J. Phys.* **1980**, *58*, 1200–1211. (d) Stephens, P.; Devlin, F.; Chabalowski, C.; Frisch, M. *J. Chem. Phys.* **1994**, *98*, 11623–11627.
- [14] Adamo, C.; Barone, V. *J. Chem. Phys.* **1999**, *110*, 6158–6169.
- [15] Yanai, T.; Tew, D.; Handy, N. *Chem. Phys. Lett.* **2004**, *393*, 51–57.
- [16] Chai, J.-D.; Head-Gordon, M. *Phys. Chem. Chem. Phys.* **2008**, *10*, 6615–6620.
- [17] Zhao, Y.; Truhlar, D. *Theor. Chem. Acc.* **2008**, *120*, 215–241.
- [18] (a) McLean, A.; Chandler, G. *J. Chem. Phys.*, **1980**, *72*, 5639–5648. (b) Raghavachari, K.; Binkley, J.; Seeger, R.; Pople, J. *J. Chem. Phys.*, **1980**, *72*, 650–654.
- [19] Dunning, T. *J. Chem. Phys.*, **1989**, *90*, 1007–1023.
- [20] (a) Weigend, F.; Ahlrichs, R. *Phys. Chem. Chem. Phys.* **2005**, *7*, 3297–3305. (b) Rappoport, D.; Furche, F. *J. Chem. Phys.* **2010**, *133*, 134105.

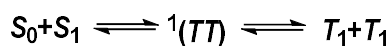
- [21] Schleyer, P.; Maerker, C.; Dransfeld, A.; Jiao, H.; Hommes, N. *J. Am. Chem. Soc.* **1996**, *118*, 6317–6318.
- [22] (a) Mayer, I. *Chem. Phys. Lett.*, **1983**, *97*, 270–274. (b) Mayer, I. *Int. J. Quantum Chem.*, **1984**, *26*, 151–154. (c) Bridgeman, A.; Cavigliasso, G.; Irelanda B.; Rothery, J. *J. Chem. Soc., Dalton Trans.*, **2001**, *14*, 2095–2108.
- [23] Becke, A.; Edgecombe, K. *J. Chem. Phys.* **1990**, *92*, 5397–5403. (b) Santos, J.; Tizando, W.; Contreras, R.; Fuentealba, P. *J. Chem. Phys.* **2004**, *120*, 1760–1763.
- [24] Lu, T.; Chen, Q. *J. Comput. Chem.*, **2012**, *33*, 580–592.
- [25] Xenides, D.; Karamanis, P. *Chem. Phys.* **2022**, *561*, 111600.
- [26] Clar, E. *The Aromatic Sextet*. New York, NY: Wiley. **1972**.
- [27] Nakano, M.; Kishi, R.; Nakagawa, N.; Ohta, S.; Takahashi, H.; Furukawa, S.; Kamada, K.; Ohta, K.; Champagne, B.; Botek, E.; Yamada, S.; Yamaguchi, K. *J. Phys. Chem. A* **2006**, *110*, 4238–4243.
- [28] Nagami, T.; Miyamoto, H.; Yoshida, W.; Okada, K.; Tonami, T.; Nakano, M. *J. Phys. Chem. A* **2020**, *124*, 6778–6789.

Chapter 3. Computational Design of Donor- π -Acceptor Systems with BN-doped PAHs as Effective π -Bridges for Singlet Fission Applications.

3.1 Introduction

BN-doped PAHs have potential applications in organic semiconductors such as organic field-effect transistors (OFETs),¹ organic light-emitting diodes (OLEDs)² and singlet fission (SF)³ materials as demonstrated in the first chapter. Significant progress has been achieved in both OFETs⁴ and OLEDs⁵ applications, in contrast with the moderate applications of SF materials. In this section, we will focus on the design of potential BN-doped PAHs using computational simulations in the application of SF materials.

The SF phenomenon has been known and studied in the delayed fluorescence of crystalline anthracene since 1965,⁶ but significant attention in SF has not been received until Hanna and Nozik⁷ suggested SF as a path to overcome the Shockley–Queisser limit ($\sim 33\%$),⁸ which is the theoretical limit of solar energy conversion efficiency. The maximum efficiency can be raised to 46% via SF owing to double low-energy triplet excitons can be generated by the absorption of one photon.⁹ In general, SF is regarded as a physical process in which a photoexcited singlet-state exciton shares its energy with a neighboring ground-state molecule, generating two triplet-state excitons. The proposed mechanism of this complex phenomenon is described as two consecutive steps.¹⁰



Where ${}^1(TT)$ is a triplet-triplet pair formed by the coupling of the lowest singlet excited state (S_1) and a neighboring ground state (S_0) in an ultrafast time scale. Due to the singlet coherence of triplet-triplet pair, singlet fission can be considered as a spin-allowed process. Two separated triplet excitons are subsequently generated by losing their electronic and spin coherence. Scholes suggests that the second step should undergo a ${}^1(T\cdots T)$ transition state which retains spin coherence but loses electronic coupling.¹¹ In addition, numerous dimers and oligomers are also found to exhibit the intramolecular singlet fission (iSF) process.¹² Considering that the energy of the two triplet-state excitons comes from the energy of single-

state exciton, SF process should agree with energy conservation. In order to prevent recombination of the triplet exciton pairs being converted to a higher triplet, the $E(T_2)$ should be higher than $2E(T_1)$. Furthermore, the $E(T_1)$ should be close to the silicon bandgap (1.1 eV) to obtain a high efficiency.¹³

$$E(S_1) \geq 2E(T_1) \quad \text{and} \quad E(T_2) > 2E(T_1)$$

Most molecules do not meet the SF conditions, as S_1 state and T_1 state usually have a narrow energy gap. During the past few decades, a number of experimental and theoretical studies have been conducted to explore potential chromophores for the application of SF.¹⁴ As a result, tetracene and pentacene have become the standard reference systems for singlet fission.¹⁵ Most of the recently reported singlet fission molecules are based on tetracene and pentacene derivatives, dimers or oligomers.¹⁶ Other reported promising examples include 1,3-diphenylisobenzofuran,¹⁷ perylenediimide (PDI),¹⁸ carotenoids,¹⁹ perylene,²⁰ zethrenes²¹ and bithiophene²². Most of these SF molecules have a clear diradical character. Based on the diradical character, Zeng theoretically investigated B_2N_2 -doped benzene and azulene small chromophores as potential candidates in SF applications.²³ Furthermore, they found that the synthesized B_2N_2 -doped pyrene is suitable for singlet fission, which is the only experimentally identified case of SF occurring in BN-doped PAHs.³ Few other B_2N_2 -doped PAHs such as anthracene,²⁴ phenanthrene²⁵ and perylene²⁶ have been explored in recent years. However, the limitation of the synthesis method makes the application of BN PAHs in SF difficult to step forward. In this work, we will explore mono BN-doped PAHs with SF potential based on the provided empirical principles in the second chapter. In addition, we will explore the effect of substituents on the excitation energy of BN-doped molecules and their potential applications in SF.

3.2 Computational details

All calculations presented in this chapter were performed using Gaussian 16 (C.01) program. The geometries were initially optimized with tight convergence restrictions at the density functional theory (DFT) level with the hybrid wB97XD functional and 6-311G(d,p) basis set. Vibrational frequency computations have been conducted in each case to ensure that the optimized structures are true minima of the corresponding potential energy surface. The optimized ground state (S_0) geometries were used as starting points for all other calculations. The adiabatic energies of excited states (S_1 and T_1) were obtained independently from TDDFT-optimized S_1 geometries and UDFT-optimized T_1 geometries. The vertical energies of excited states (S_1 and T_1) were obtained from single-point calculation by TD-DFT. Electron-hole analysis²⁷ used in the rationalization of the results have been carried out with the Multiwfn 3.8 (dev) program.

3.3 Results and discussion

In the first step, we calculated the adiabatic energies of the first singlet (S_1) and triplet (T_1) excited states of tetracene and pentacene (Table 3.1). Compared with experimental results of tetracene²⁸ and pentacene²⁹ which reported from fluorescence and phosphorescence emission spectra in solid state, the predicted excitation energies are slightly found higher.

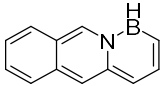
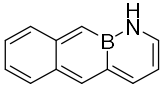
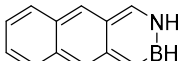
Table 3.1. Experimental and calculational excited states energies of tetracene and pentacene.

Molecule	Experimental			wB97XD/6-311G(d,p)		
	E_{S1} (eV)	E_{T1} (eV)	Δ_{SF} (eV)	E_{S1} (eV)	E_{T1} (eV)	Δ_{SF} (eV)
Tetracene	2.24	1.20	-0.16	2.68	1.29	0.09
Pentacene	1.83	0.86	0.11	2.18	0.85	0.48

The distribution of S_1 and T_1 energy of anthracene is not conducive to the occurrence of SF process due to large endoergonic effects. However, the BN/CC single bond replacement in anthracene could significantly lower the energy of excited states from our research in the second chapter. Three isosteres of anthracene, namely BN-9a,1-anthracene, BN-1,9a-anthracene and

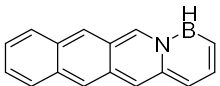
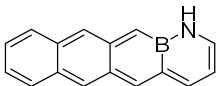
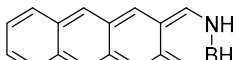
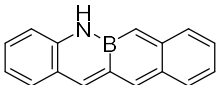
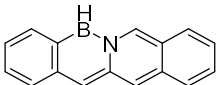
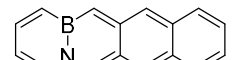
BN-2,3-anthracene, have slightly lower adiabatic energy of S_1 and T_1 than all-carbon tetracene at wB97XD/6-311G(d,p) level (Table 3.2).

Table 3.2. Computational excited states energies of BN-9a,1-anthracene, BN-1,9a-anthracene and BN-2,3-anthracene at wB97XD/6-311G(d,p) level.

wB97XD	 BN-9a,1-Anth	 BN-1,9a-Anth	 BN-2,3-Anth
E_{S_1} (eV)	2.56	2.66	2.64
E_{T_1} (eV)	1.25	1.21	1.19
Δ_{SF} (eV)	0.06	0.25	0.26

The distribution of S_1 and T_1 energy of tetracene exhibited a small endoergonicity, which could be easily achieved by room temperature for SF process. The strategy of BN/CC single bond replacement in tetracene could provide lower energy of excited states (Table 3.3). Specifically, BN-12a,1-tetracene and BN-1,12a-tetracene exhibited lower energy of excited states than all-carbon pentacene.

Table 3.3. Computational excited states energies of selected BN-tetracene isomers at wB97XD/6-311G(d,p) level.

wB97XD	 BN-12a,1-Tetra	 BN-1,12a-Tetra	 BN-2,3-Tetra
E_{S_1} (eV)	1.96	2.05	2.25
E_{T_1} (eV)	0.69	0.66	0.97
Δ_{SF} (eV)	0.59	0.73	0.31
wB97XD	 BN-11,11a-Tetra	 BN-11a,11-Tetra	 BN-6a,10a-Tetra
E_{S_1} (eV)	2.38	2.25	2.46
E_{T_1} (eV)	0.94	0.97	0.98
Δ_{SF} (eV)	0.50	0.31	0.49

Due to limited effect of BN doping on the energy of excited states, not all molecules can be modified by a solely BN/CC replacement strategy. For instance, phenanthrene is not suitable as a SF material owing to relatively high energy of excited states. At the same level of theory, the adiabatic energy of S_1 and T_1 are 4.19 eV and 2.89 eV, respectively. Among all BN analogues of phenanthrene, BN-9,8a-phenanthrene exhibits the lowest adiabatic energies for S_1 (3.21 eV) and T_1 (1.73 eV), but still, it does not meet the conditions for SF processes. In this case, we attempted to further control the energy of the excited states by adding substituents. To the best of our knowledge, a thorough investigation of how the substituents affect the excited state energies of BN-doped PAHs has not been performed in connection to SF applications. In a first step we studied the vertical excitation energies of all mono-amino phenanthrene isomers and mono-nitro phenanthrene isomers separately. In the second step we used combinations of these functional groups to investigate substitution effects on their excited state energies.

Our computation suggested that all the amino phenanthrene isomers have slightly lower energy of S_1 than parent phenanthrene, whereas the energies of T_1 rarely change. On the other hand, the nitro phenanthrene isomers also exhibit a slightly lower energy for S_1 than pure phenanthrene. Also, we have noticed that the electron-withdrawing nitro-substituted phenanthrene isomers have lower excited state energies (S_1 and T_1) than the electron-donating amino-substituted phenanthrene isomers.

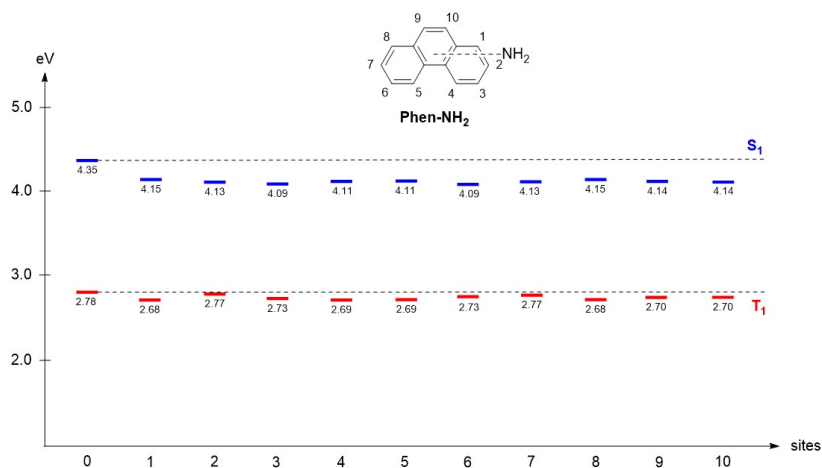


Figure 3.1. Vertical excitation energy of aminophenanthrene isomers. All calculations have been carried out at wB97XD/6-311G(d,p).

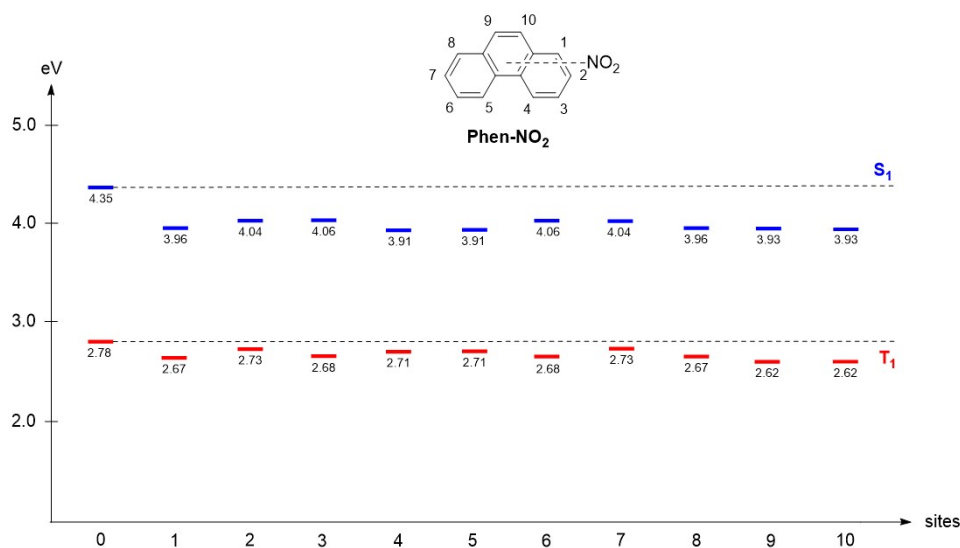


Figure 3.2. Vertical excitation energy of nitrophenanthrene isomers. All calculations have been carried out at wB97XD/6-311G(d,p).

In terms of excitation energy, both amino phenanthrene and nitro phenanthrene showed less regioselectivity. To understand the substituent effects on energy of excited states, we performed the molecular orbitals (MO) and natural transition orbitals (NTO) related to the excitation from S_0 to S_1 . We found that the first excitation of phenanthrene could not be described by single dominant MO or NTO transition. The first excitation can be described approximately by HOMO to LUMO+1 transition (contribution: 52.0%) and HOMO-1 to LUMO transition (contribution: 45.2%). The NTO analysis provided a similar result which included NTO-47 to NTO-48 transition (contribution: 55.3%) and NTO-46 to NTO-49 transition (contribution: 41.6%).

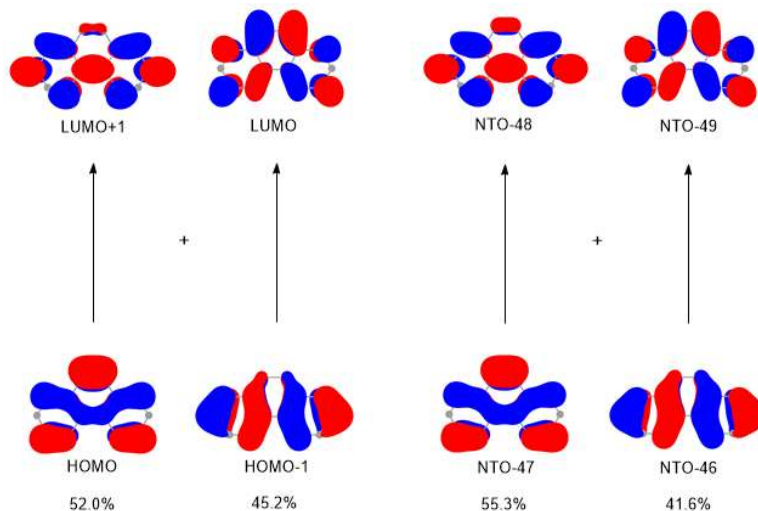


Figure 3.3. Related MO and NTO transition of the first excitation. All calculations have been carried out at wB97XD/6-311G(d,p).

To explore the differences of each substitution site in the excitation, the hole-electron analysis was performed in this work using Multiwfn 3.8(dev) program which is one of most powerful tools to analyze electron excitation characteristic. In the hole-electron analysis, the contribution of all MO transitions to hole and electron distributions can be fully involved. The hole-electron analysis described transition as hole and electron model, hole indicates decrease of the electron density in the excitation, on the contrary, electron indicates increase of electron density in the excitation. From the hole-electron analysis of phenanthrene, red isosurface represents hole region which is consistent with π bonding orbitals, blue isosurface represents electron region which is consistent with π anti-bonding orbitals. From the perspective of the molecular orbital model, the hole to electron transition can be regarded as π to π^* transition. Furthermore, the contribution of the substitutable site atom to the hole/electron were calculated to reveal substitution effects in the excitation. In the first singlet excitation of phenanthrene, all carbon atoms had similar unseparated hole and electron density, which is consistent with the local excitation characteristic as well as all amino phenanthrene isomers or nitro phenanthrene isomers had similar S_1 energy. Although the transition from S_0 to T_1 is spin forbidden, we can still investigate the transition characteristics via TD-DFT. From the hole-electron analysis of S_0 to T_1 transition, each atom also had highly overlapped hole and electron density, resulting

similar T_1 energy of each amino phenanthrene or nitro phenanthrene isomers.

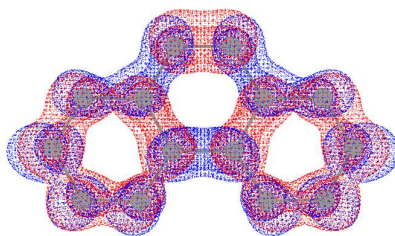


Figure 3.4. Hole and electron distribution of phenanthrene in S_0 to S_1 excitation. All calculations have been carried out at wB97XD/6-311G(d,p).

Table 3.4. Contribution of each substitutable site atoms to hole and electron in S_0 to S_1 excitation of phenanthrene.

Site	Hole (%)	Electron (%)	Overlap (%)	Difference (%)
1	6.55	6.22	6.38	-0.33
2	6.51	8.64	7.50	2.13
3	7.10	5.76	6.31	-1.49
4	6.59	7.31	6.94	0.72
5	6.59	7.31	6.94	0.72
6	7.10	5.76	6.31	-1.49
7	6.51	8.64	7.50	2.13
8	6.55	6.22	6.38	-0.33
9	8.68	6.99	7.79	-1.68
10	8.68	6.99	7.79	-1.68

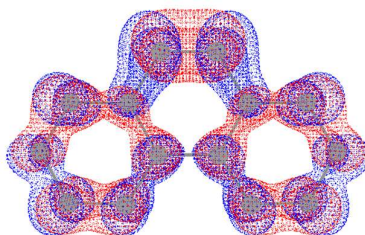


Figure 3.5 Hole and electron distribution of phenanthrene in S_0 to T_1 excitation. All calculations have been carried out at wB97XD/6-311G(d,p).

Table 3.5 Contribution of each substitutable site atoms to hole and electron in S_0 to T_1 excitation of phenanthrene.

Site	Hole (%)	Electron (%)	Overlap (%)	Difference (%)
1	8.12	7.98	8.05	-0.14
2	4.26	4.20	4.23	-0.06
3	7.11	7.16	7.13	0.05
4	6.83	6.75	6.79	-0.08
5	6.83	6.75	6.79	-0.08
6	7.11	7.16	7.13	0.05
7	4.26	4.20	4.23	-0.06
8	8.12	7.98	8.05	-0.14
9	13.45	13.56	13.51	0.12
10	13.45	13.56	13.51	0.12

The hole-electron analysis was also performed in excitation of BN doped phenanthrene analogues. It is useful to recall here that in the second chapter of this thesis, we had divided all BN phenanthrene analogues into four groups based on the bond characteristic, involving single bond, partial single bond, double bond and partial double bond. Herein, we selected four representative isomers, which included BN-9,8a-phenanthrene, BN-2,3-phenanthrene, BN-1,2-phenanthrene, and BN-9,10-phenanthrene, instead of all BN isomers to investigate the substituent effects towards the energy of excited states. Compared with all-carbon phenanthrene, BN-9,8a-phenanthrene had apparent regioselectivity on substituent effects. Among all amino BN-9,8a-phenanthrene isomers, more than half isomers, including 1-NH₂, 3-NH₂, 5-NH₂, 7-NH₂, 9-NH₂ and 10-NH₂, had similar S_1 and T_1 energy with unsubstituted BN-9,8a-phenanthrene. Interestingly, 3-NH₂ isomer features slightly higher excitation energy than BN-9,8a-phenanthrene. The rest amino BN-9,8a-phenanthrene isomer, 2-NH₂, 4-NH₂, 6-NH₂ and 8-NH₂, bear lower excitation energy. The lowest excitation energy amongst all amino BN-9,8a-phenanthrene isomers is spotted in 6-NH₂ isomer. Among all nitro BN-9,8a-phenanthrene isomers, 2-NO₂, 4-NO₂, 5-NO₂, 6-NO₂, 7-NO₂ and 8-NO₂ had similar excitation energy with unsubstituted BN-9,8a-phenanthrene, whereas isomers of 1-NO₂, 3-NO₂, 9-NO₂ and 10-NO₂ had lower excitation energy. Especially, 9-NO₂ and 10-NO₂ had significant decrease on energy of S_1 and T_1 .

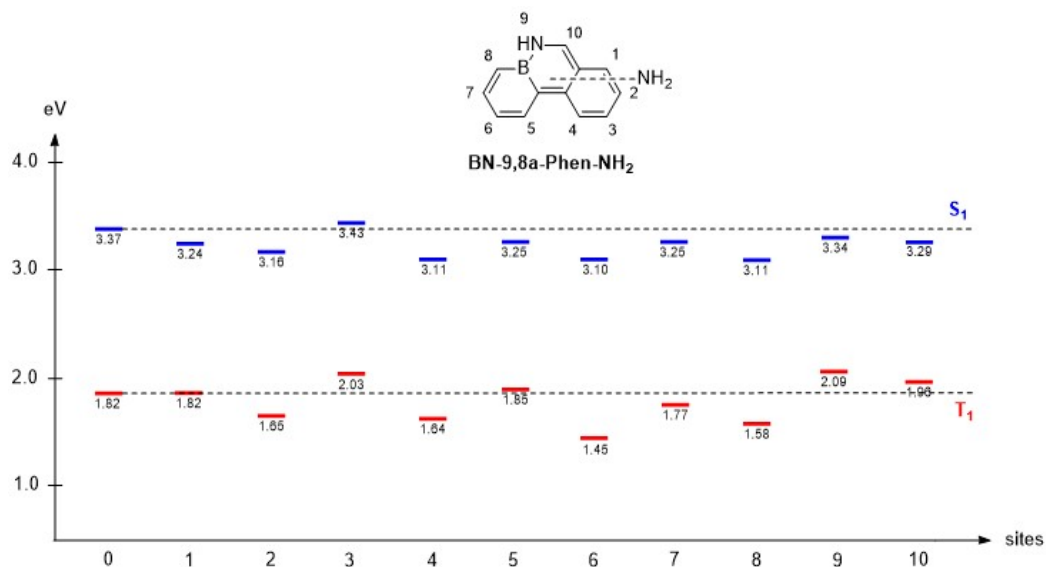


Figure 3.6. Vertical excitation energy of amino BN-9,8a-phenanthrene isomers. All calculations have been carried out at wB97XD/6-311G(d,p).

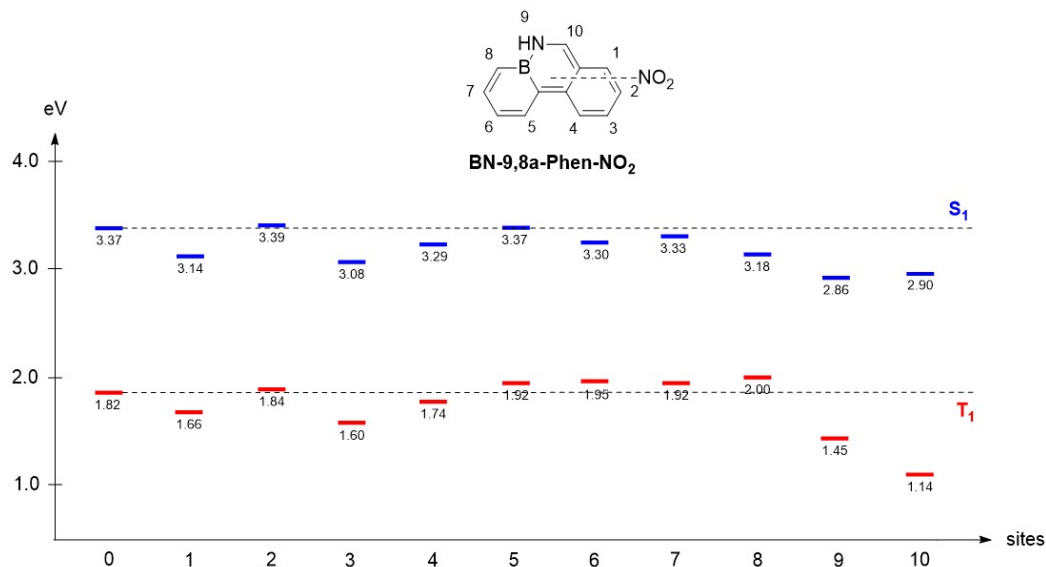


Figure 3.7 Vertical excitation energy of nitro BN-9,8a-phenanthrene isomers. All calculations have been carried out at wB97XD/6-311G(d,p).

Unlike the all-carbon phenanthrene, the BN-9,8a-phenanthrene has partially separated hole and electron density. From the contribution of each atom, C6 had the highest hole density, meanwhile, 6-NH₂ had the lowest energy of S₁ and T₁. C2 and C4 had higher hole density, and 2-NH₂ and 4-NH₂ had lower energy of S₁ and T₁. We consider that the introduction of an

electron donor, such as an amino group, at sites with high hole density produces a localized charge transfer, which enhances the charge transfer characteristics of the whole molecule in the excitation. This is directly related to the decreased excited state energy. However, 8-NH₂ had lower energy of S₁ and T₁, but density of hole and electron is lower and highly overlapped. The possible reason could be that the linked boron atom owns high hole density enabling the charge transfer occurred from amino group to boron fragment. On the other hand, C10 position has the highest electron density, and N, C3 and C1 positions have higher electron density which are consistent with that the 10-NO₂, 9-NO₂, 3-NO₂ and 1-NO₂ have lower energy of S₁ and T₁. Comparison of amino and nitro, electron acceptor is more functional than electron donor to reduce energy of excited states.

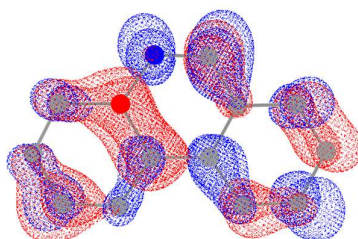


Figure 3.8. hole and electron distribution of BN-9,8a-phenanthrene in S₀ to S₁ excitation. All calculations have been carried out at wB97XD/6-311G(d,p).

Table 3.6. Contribution of each substitutable site atoms to hole and electron in S₀ to S₁ excitation of BN-9,8a-phenanthrene

Site	Hole (%)	Electron (%)	Overlap (%)	Difference (%)
1	5.89	7.68	6.73	1.79
2	7.05	0.96	2.60	-6.10
3	3.17	11.93	6.15	8.76
4	8.04	3.54	5.34	-4.50
5	1.48	3.62	2.32	2.14
6	14.01	5.52	8.80	-8.48
7	2.52	2.84	2.67	0.32
8	5.63	6.13	5.87	0.50
9	1.34	13.53	4.25	12.19
10	11.29	21.96	15.75	10.66

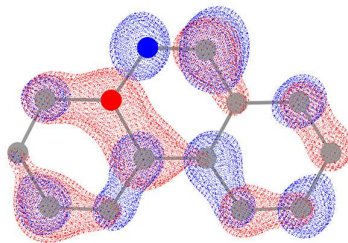


Figure 3.9. Hole and electron distribution of BN-9,8a-phenanthrene in S_0 to T_1 excitation. All calculations have been carried out at wB97XD/6-311G(d,p).

Table 3.7 Contribution of each substitutable site atoms to hole and electron in S_0 to T_1 excitation of BN-9,8a-phenanthrene

Site	Hole (%)	Electron (%)	Overlap (%)	Difference (%)
1	4.84	7.64	6.08	2.80
2	4.86	1.29	2.50	-3.57
3	3.23	9.25	5.46	6.02
4	6.77	3.58	4.92	-3.20
5	2.92	4.53	3.64	1.61
6	15.52	7.80	11.00	-7.72
7	2.13	1.30	1.67	-0.83
8	7.91	5.84	6.79	-2.07
9	0.16	13.13	1.45	12.97
10	13.83	25.81	18.89	11.98

Furthermore, we investigated the effect of different electronic donor substituted at the C6 position on the excited state energy. In selected few electron donors, amino BN-9,8a-phenanthrene has the lowest excitation energy. On the contrary, N,N-dimethyl amino substituted BN-9,8a-phenanthrene has almost same excitation energy, it could be caused by the inability to form a p - π conjugation of the N,N-dimethylamino perpendicular to the plane of the phenanthrene. The σ - π hyperconjugation from methyl has less effect on the excitation energy. For π - π conjugation, vinyl reduces excited state energy more than phenyl. Although the chlorine is an electron withdrawing group, we still want to examine whether p - π conjugation can reduce the excited state energy, the answer is negative. From excitation energy of 10-acceptor-BN-9,8a-phenanthrenes, many electron acceptors can significantly reduce the excitation energy, such as CN, COOH, CHO and pyrazinyl. F and CF_3 have less effect on decrease of the

excitation energy because of the π - π^* transition.

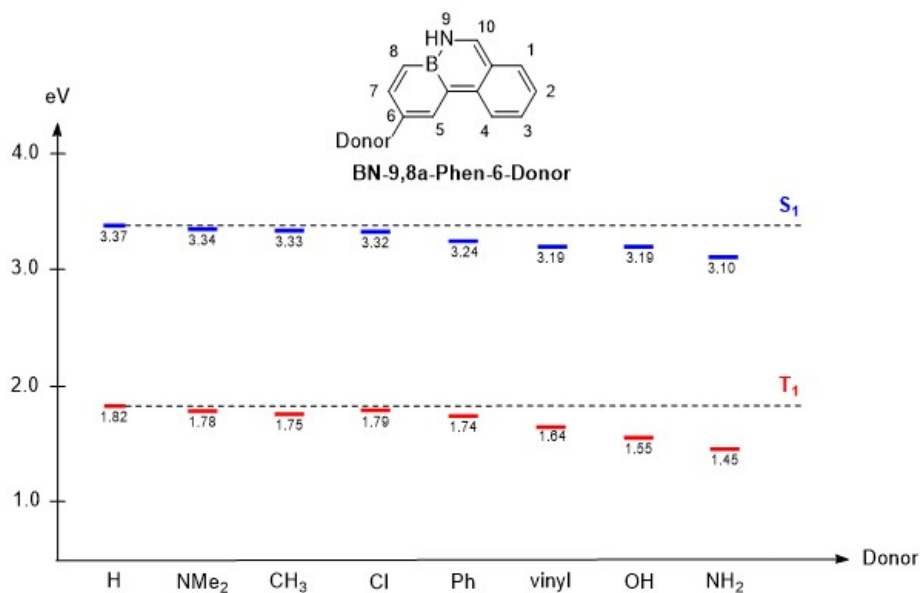


Figure 3.10. Vertical excitation energy of 6-donor-BN-9,8a-phenanthrenes. All calculations have been carried out at wB97XD/6-311G(d,p).

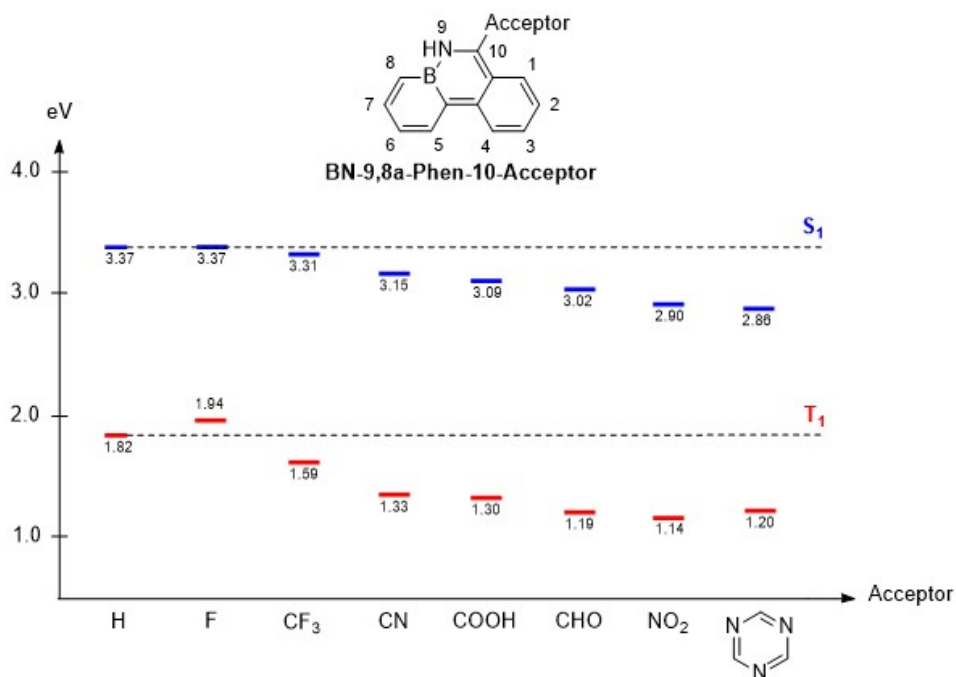


Figure 3.11. Vertical excitation energy of 10-acceptor-BN-9,8a-phenanthrenes. All calculations have been carried out at wB97XD/6-311G(d,p).

From the excitation energy of amino BN-2,3-phenanthrene isomers, the substituent effect on excitation energy was not significant as BN-9,8a-phenanthrene, relatively 3-NH₂ and 4-NH₂ have slightly reduced excitation energy. Two nitro BN-2,3-phenanthrene isomers, 1-NO₂ and 2-NO₂, have significantly lower excitation energy than unsubstituted BN-2,3-phenanthrene. These results could be also explained by the distribution of hole and electron density. We found C4 position has 14.58% hole and 15.51% electron density, which should be unfavorable for electron donor substitution. However, 4-NH₂ has the lowest excitation energy in whole amino BN-2,3-phenanthrene isomers, which is not consistent with our initial analysis. The possible reason is that C4 and B position have a large linked hole density which enable the charge transfer from amino to these two atoms. As a result, in some cases, the distribution of adjacent electrons or holes needs to be considered to predict the feasibility of charge transfer.

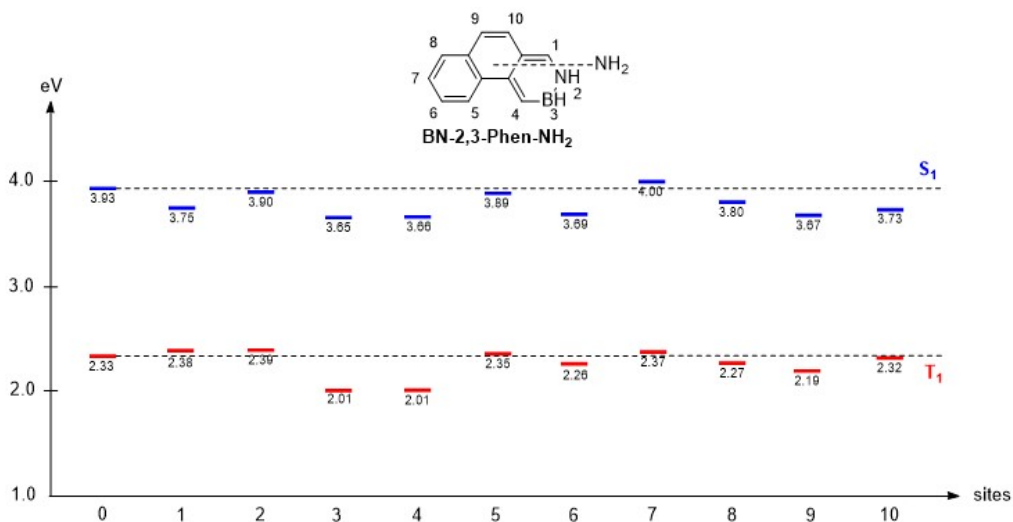


Figure 3.12. Vertical excitation energy of amino BN-2,3-phenanthrene isomers. All calculations have been carried out at wB97XD/6-311G(d,p).

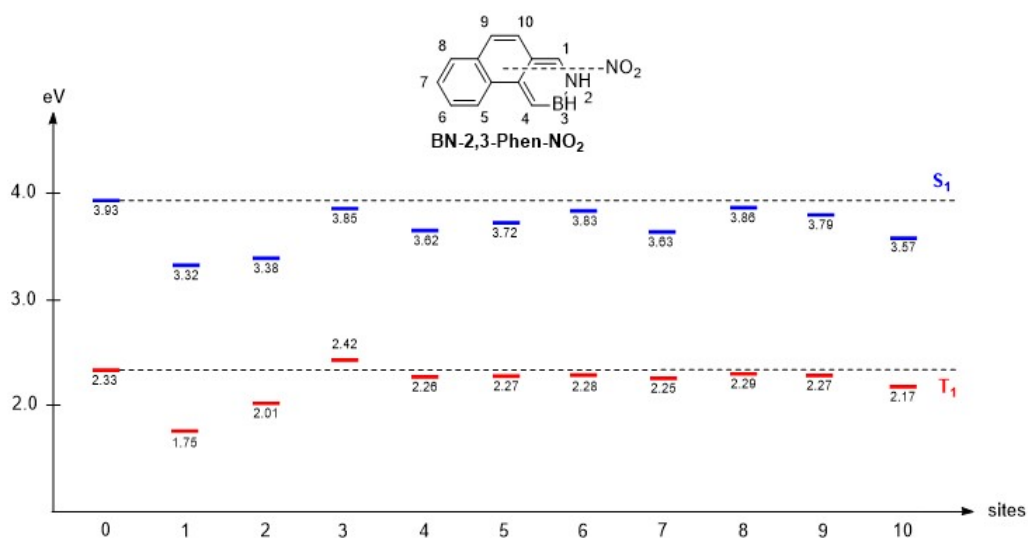


Figure 3.13. Vertical excitation energy of nitro BN-2,3-phenanthrene isomers. All calculations have been carried out at wB97XD/6-311G(d,p).

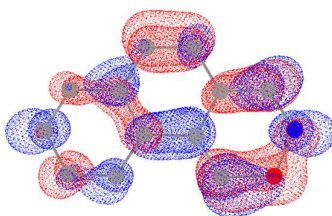


Figure 3.14. Hole and electron distribution of BN-2,3-phenanthrene in S_0 to S_1 excitation. All calculations have been carried out at wB97XD/6-311G(d,p).

Table 3.8. Contribution of each substitutable site atoms to hole and electron in S_0 to S_1 excitation of BN-2,3-phenanthrene.

Site	Hole (%)	Electron (%)	Overlap (%)	Difference (%)
1	12.98	15.64	12.25	2.66
2	3.07	9.60	5.43	6.54
3	10.52	4.41	6.81	-6.11
4	14.58	15.51	15.04	0.93
5	1.21	6.26	2.75	5.05
6	6.35	2.08	3.64	-4.27
7	1.63	8.80	3.78	7.81
8	4.38	1.60	2.65	-2.78
9	14.01	1.54	4.65	-12.47
10	10.57	5.11	7.35	-5.46

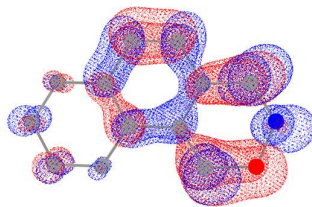


Figure 3.15. Hole and electron distribution of BN-2,3-phenanthrene in S_0 to T_1 excitation. All calculations have been carried out at wB97XD/6-311G(d,p).

Table 3.9 Contribution of each substitutable site atoms to hole and electron in S_0 to T_1 excitation of BN-2,3-phenanthrene

Site	Hole (%)	Electron (%)	Overlap (%)	Difference (%)
1	16.45	24.77	20.18	8.32
2	0.70	8.99	2.51	8.29
3	11.55	0.03	0.58	-11.52
4	21.87	16.43	18.96	-5.44
5	1.25	2.31	1.70	1.07
6	3.81	3.18	3.48	-0.63
7	1.89	3.68	2.64	1.79
8	2.29	1.61	1.92	-0.68
9	12.06	7.19	9.31	-4.87
10	8.35	10.57	9.40	2.22

From the excitation energy of amino BN-1,2-phenanthrene and nitro BN-1,2-phenanthrene isomers, the energy of T_1 state of all isomers show less difference with the unsubstituted BN-1,2-phenanthrene, whereas energy of S_1 differ from the substituent sites. The most favorable substituent sites for electron donor and electron acceptor are C3 and C9 position respectively.

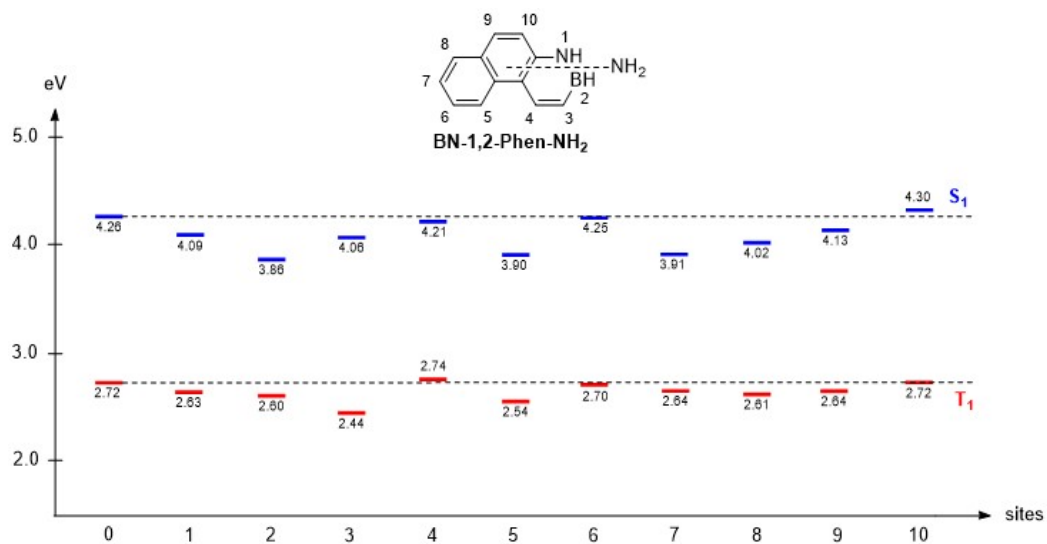


Figure 3.16. Vertical excitation energy of amino BN-1,2-phenanthrene isomers. All calculations have been carried out at wB97XD/6-311G(d,p).

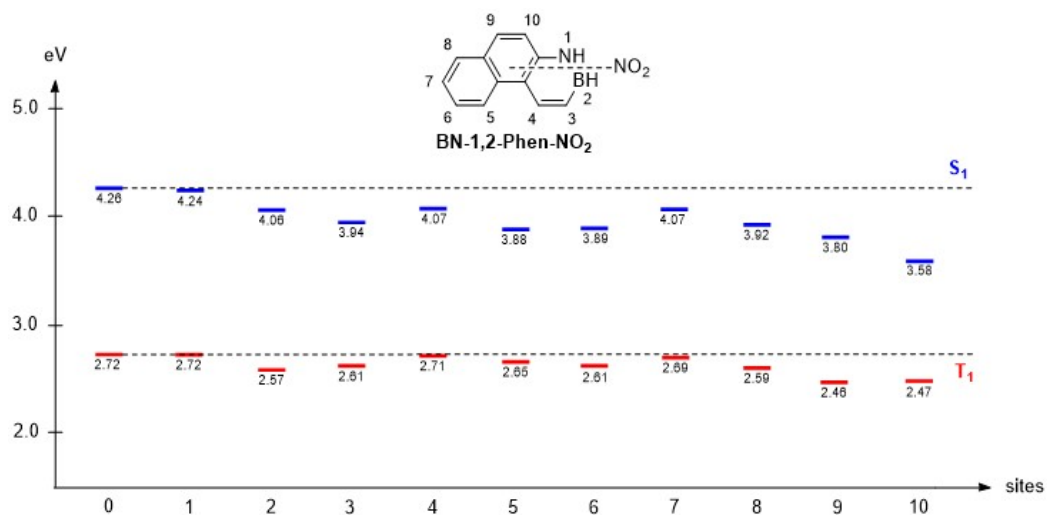


Figure 3.17. Vertical excitation energy of nitro BN-1,2-phenanthrene isomers. All calculations have been carried out at wB97XD/6-311G(d,p).

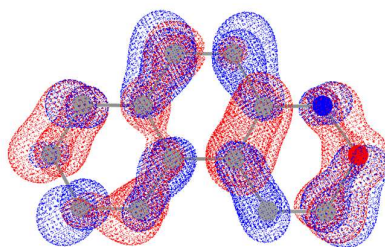


Figure 3.18. Hole and electron distribution of BN-1,2-phenanthrene in S_0 to S_1 excitation. All calculations have been carried out at wB97XD/6-311G(d,p).

Table 3.10 Contribution of each substitutable site atoms to hole and electron in S_0 to S_1 excitation of BN-1,2-phenanthrene

Site	Hole (%)	Electron (%)	Overlap (%)	Difference (%)
1	12.98	15.64	12.25	2.66
2	3.07	9.60	5.43	6.54
3	10.52	4.41	6.81	-6.11
4	14.58	15.51	15.04	0.93
5	1.21	6.26	2.75	5.05
6	6.35	2.08	3.64	-4.27
7	1.63	8.80	3.78	7.81
8	4.38	1.60	2.65	-2.78
9	14.01	1.54	4.65	-12.47
10	10.57	5.11	7.35	-5.46

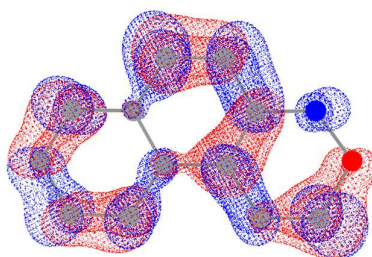


Figure 3.19. Hole and electron distribution of BN-1,2-phenanthrene in S_0 to T_1 excitation. All calculations have been carried out at wB97XD/6-311G(d,p).

Table 3.11. Contribution of each substitutable site atoms to hole and electron in S_0 to T_1 excitation of BN-1,2-phenanthrene.

Site	Hole (%)	Electron (%)	Overlap (%)	Difference (%)
1	0.26	3.75	0.99	3.48
2	4.60	0.79	1.91	-3.81
3	13.57	11.20	12.33	-2.37
4	2.93	5.55	4.03	2.62
5	9.49	7.15	8.23	-2.34
6	5.99	6.80	6.38	0.81
7	4.84	3.39	4.05	-1.45
8	8.76	9.17	8.97	0.41
9	14.75	17.79	16.20	3.04
10	7.85	10.24	8.97	2.39

From the excitation energy of amino BN-9,10-phenanthrene and nitro BN-9,10-phenanthrene isomers, the energy of T₁ state of all isomers except 10-NO₂ show less difference with the unsubstituted BN-9,10-phenanthrene. Interestingly, we found the hole and electron density of boron only have 2.07% and 2.21% respectively in the S₀ to T₁ excitation. However, the isomer 10-NO₂ has lower energy of T₁. Although the hole and electron of nitrogen also have very low density, the T₁ energy of isomer 9-NO₂ is same as parent BN-9,10-phenanthrene. In this case, the substituent effect cannot be explained by the hole-electron analysis. On the other hand, both 1-NH₂ and 9-NO₂ have reduced S₁-T₁ gap, which could be applied in design of TADF materials.

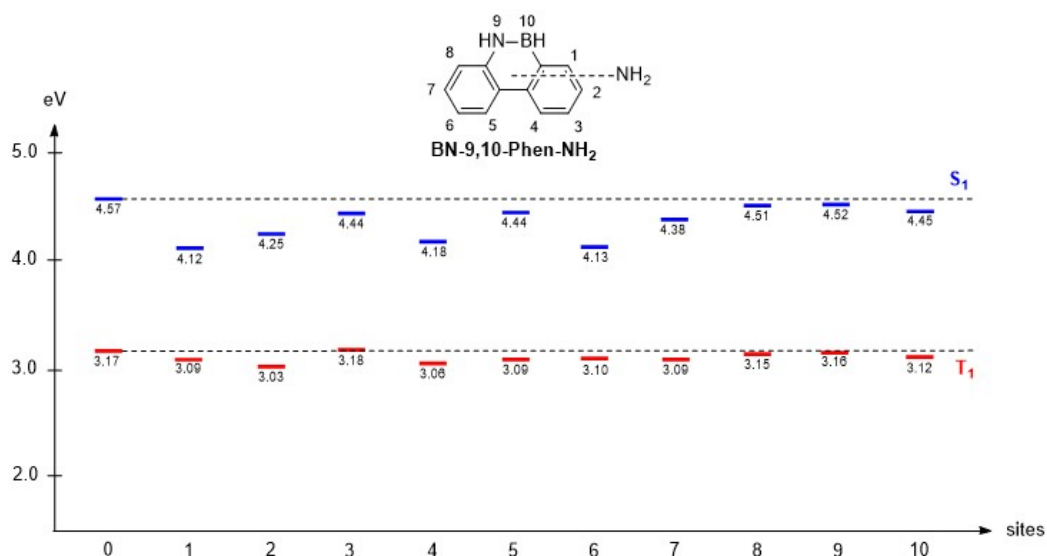


Figure 3.20. Vertical excitation energy of amino BN-9,10-phenanthrene isomers. All calculations have been carried out at wB97XD/6-311G(d,p).

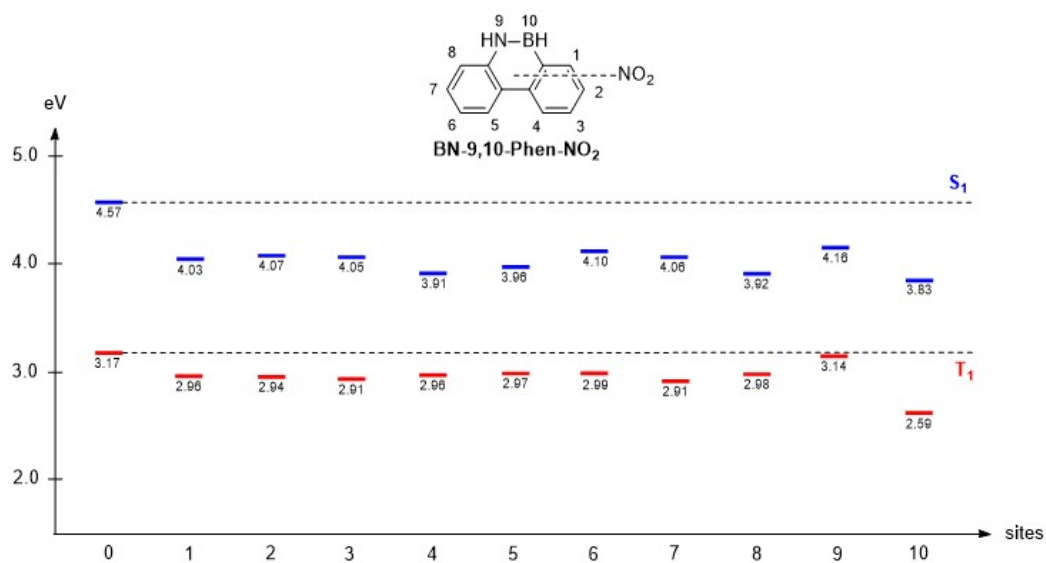


Figure 3.21. Vertical excitation energy of nitro BN-9,10-phenanthrene isomers. All calculations have been carried out at wB97XD/6-311G(d,p).

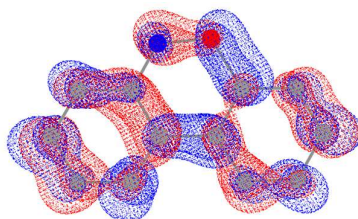


Figure 3.22. Hole and electron distribution of BN-9,10-phenanthrene in S_0 to S_1 excitation. All calculations have been carried out at wB97XD/6-311G(d,p).

Table 3.12. Contribution of each substitutable site atoms to hole and electron in S_0 to S_1 excitation of BN-9,10-phenanthrene.

Site	Hole (%)	Electron (%)	Overlap (%)	Difference (%)
1	6.34	3.35	4.61	-2.99
2	8.07	7.66	7.86	-0.42
3	3.09	7.29	4.74	4.21
4	10.21	3.76	6.19	-6.45
5	3.34	12.05	6.35	8.71
6	10.51	3.35	5.93	-7.17
7	6.90	10.40	8.47	3.50
8	5.40	8.67	6.84	3.27
9	8.72	2.61	4.77	-6.11
10	4.08	9.57	6.25	5.49

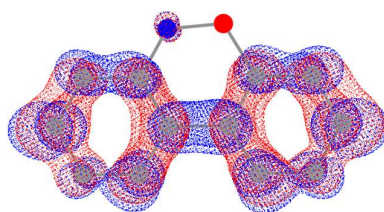


Figure 3.23. Hole and electron distribution of BN-9,10-phenanthrene in S_0 to T_1 excitation. All calculations have been carried out at wB97XD/6-311G(d,p).

Table 3.13. Contribution of each substitutable site atoms to hole and electron in S_0 to T_1 excitation of BN-9,10-phenanthrene.

Site	Hole (%)	Electron (%)	Overlap (%)	Difference (%)
1	7.09	7.37	7.23	0.29
2	11.79	11.06	11.42	-0.73
3	4.32	4.69	4.50	0.36
4	10.65	10.12	10.38	-0.52
5	8.78	9.50	9.13	0.72
6	4.35	3.59	3.95	-0.76
7	10.35	11.06	10.70	0.71
8	5.52	6.11	5.81	0.60
9	1.47	1.45	1.46	-0.01
10	2.07	2.21	2.14	0.14

Calculations show that the electron acceptor has a greater effect on the excitation energy of BN-doped molecules than the electron donor. In addition, BN/CC single bond replaced molecules are more suitable as π -bridges in the D- π -A system for SF molecules. From Figure 3.24, six BN-doped phenanthrene isomers including BN-9,8a-phenanthrene, BN-8a,9-phenanthrene, BN-4a,4b-phenanthrene, BN-4,4a-phenanthrene, BN-4a,4-phenanthrene and BN-2,3-phenanthrene can satisfy the SF condition by substituted donor and acceptor. Donor and acceptor substituted BN-3,2-phenanthrene cannot achieve the exothermic condition due to the lowest S_1 energy caused by vibrational relaxation.

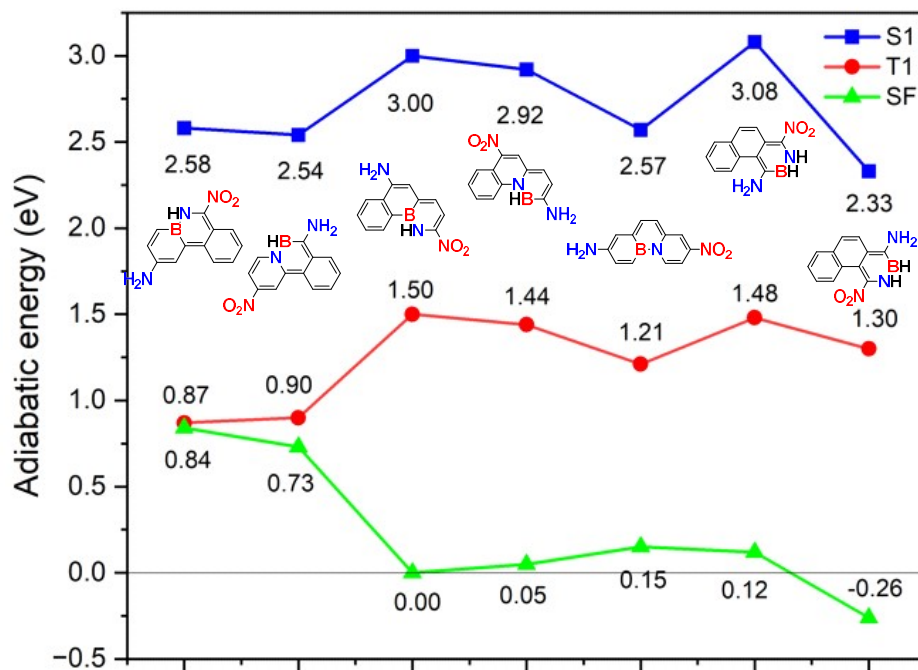


Figure 3.24. Selected BN-doped phenanthrene isomers designed as D- π -A systems in SF. All calculations have been carried out at wB97XD/6-311G(d,p).

3.4 Conclusion

In conclusion, introducing small size electron donors and/or electron acceptors to phenanthrene and BN isosteres have been computationally investigated to understand the substituent effects on the properties of excited states. The results indicate that mono donor (amino) or acceptor (nitro) substituted phenanthrene isomers have similar energies of the first singlet (S_1) and the first triplet (T_1) excited states, which are also close to the unsubstituted phenanthrene. BN doped phenanthrene analogues have varied substituent effects from positioning of the BN unit. Following the given empirical principle established the second chapter of this thesis, four types of BN-doped phenanthrene are involved for the exploration of substituent effects. The privileged substitution sites are revealed by the hole-electron analysis, in which the substitution site with the highest density of hole or electron will result to a significant decrease on the energies of excited states by substitution of a donor or an acceptor respectively. Usually, the privileged substitution sites will locate at the place where are parallel with the BN bond, which increase the distance of charge transfer to maximum from direction of donor to acceptor. The isomer which BN bond located at localized double bond position, such as BN-9,10-phenanthrene, the privileged substitution site is located at boron atom for electron acceptors. The strategy of increasing the charge transfer distance through a BN bond should be potentially applied in the design of organic light-emitting or singlet fission materials.

En conclusion, l'introduction de donneurs et/ou d'accepteurs d'électrons de petite taille dans le phénanthrène et les isostères de BN a fait l'objet d'une étude théorique pour comprendre les effets des substituants sur les propriétés des états excités. Les résultats indiquent que les isomères de phénanthrène substitués par un donneur (amino) ou un accepteur (nitro) ont des énergies similaires pour le premier singulet (S1) et le premier triplet (T1) des états excités, qui sont également proches du phénanthrène non substitué. Les analogues du phénanthrène dopés au BN ont des effets de substitution variés en raison du positionnement de l'unité BN. Suivant le principe empirique établi dans le deuxième chapitre de cette thèse, quatre types de phénanthrène dopé au BN sont impliqués dans l'évaluation des effets de substitution. Les sites de substitution privilégiés sont révélés par l'analyse trou-électron, dans laquelle le site de substitution avec la plus grande densité de trou ou d'électron entraînera une diminution significative des énergies des états excités par la substitution d'un donneur ou d'un accepteur respectivement. En général, les sites de substitution privilégiés se situent à des endroits parallèles à la liaison BN, ce qui augmente la distance de transfert de charge au maximum de la direction du donneur à l'accepteur. Pour l'isomère dont la liaison BN est située en position de double liaison localisée, comme le BN-9,10-phénanthrène, le site de substitution privilégié est situé au niveau de l'atome de bore pour les accepteurs d'électrons. La stratégie consistant à augmenter la distance de transfert de charge par le biais d'une liaison BN devrait être potentiellement appliquée à la conception de matériaux organiques émetteurs de lumière ou de fission de singulets.

Reference

- [1] Zhao, K.; Yao, Z.-F.; Wang, Z.-Y.; Zeng, J.-C.; Ding, L.; Xiong, M.; Wang, J.-Y.; Pei, J. *J. Am. Chem. Soc.* **2022**, *144*, 3091–3098.
- [2] Hatakeyama, T.; Shiren, K.; Nakajima, K.; Nomura, S.; Nakatsuka, S.; Kinoshita, K.; Ni, J.; Ono, Y.; Ikuta, T. *Adv. Mater.* **2016**, *28*, 2777–2781.
- [3] Zeng, T.; Møllerup, S. K.; Yang, D.; Wang, X.; Wang, S.; Stampelcoskie, K. *J. Phys. Chem. Lett.* **2018**, *9*, 2919–2927.
- [4] Li, W.; Du, C.; Chen, X.; Fu, L.; Gao, R.; Yao, Z.; Wang, J.; Hu, W.; Pei, J.; Wang, X. *Angew. Chem. Int. Ed.* **2022**, *61*.
- [5] Kondo, Y.; Yoshiura, K.; Kitera, S.; Nishi, H.; Oda, S.; Gotoh, H.; Sasada, Y.; Yanai, M.; Hatakeyama, T. *Nat. Photonics* **2019**, *13*, 678–682.
- [6] Singh, S.; Jones, W. J.; Siebrand, W.; Stoicheff, B. P.; Schneider, W. G. *J. Chem. Phys.* **1965**, *42*, 330–342.
- [7] Hanna, M. C.; Nozik, A. J. *J. Appl. Phys.* **2006**, *100*, 074510.
- [8] Shockley, W.; Queisser, H. J. *J. Appl. Phys.*, **1961**, *32*, 510–519.
- [9] Xia, J.; Sanders, S. N.; Cheng, W.; Low, J. Z.; Liu, J.; Campos, L. M.; Sun, T. *Adv. Mater.* **2017**, *29*, 1601652.
- [10] (a) Smith, M. B.; Michl, J. *Chem. Rev.* **2010**, *110*, 6891–6936. (b) Casanova, D. *Chem. Rev.* **2018**, *118*, 7164–7207.
- [11] Pensack, R. D.; Ostroumov, E. E.; Tilley, A. J.; Mazza, S.; Grieco, C.; Thorley, K. J.; Asbury, J. B.; Seferos, D. S.; Anthony, J. E.; Scholes, G. D. *J. Phys. Chem. Lett.* **2016**, *7*, 2370–2375.
- [12] (a) Millington, O.; Montanaro, S.; Leventis, A.; Sharma, A.; Dowland, S. A.; Sawhney, N.; Fallon, K. J.; Zeng, W.; Congrave, D. G.; Musser, A. J.; Rao, A.; Bronstein, H. *J. Am. Chem. Soc.* **2023**, *145*, 2499–2510. (b) Busby, E.; Xia, J.; Wu, Q.; Low, J. Z.; Song, R.; Miller, J. R.; Zhu, X.-Y.; Campos, L. M.; Sfeir, M. Y. *Nat. Mater.* **2015**, *14*, 426–433. (c) Margulies, E. A.; Miller, C. E.; Wu, Y.; Ma, L.; Schatz, G. C.; Young, R. M.; Wasielewski, M. *Nat. Chem.* **2016**, *8*, 1120–1125. (d) Fuemmeler, E. G.; Sanders, S. N.; Pun, A. B.; Kumarasamy, E.; Zeng, T.; Miyata, K.; Steigerwald, M. L.; Zhu, X.-Y.; Sfeir, M. Y.; Campos, L. M.; Ananth, N. *ACS Cent. Sci.* **2016**, *2*, 316–324.
- [13] Paci, I.; Johnson, J. C.; Chen, X.; Rana, G.; Popović, D.; David, D. E.; Nozik, A. J.; Ratner, M. A.;

- Michl, J. *J. Am. Chem. Soc.* **2006**, *128*, 16546–16553.
- [14] (a) Minami, T.; Ito, S.; Nakano, M. *J. Phys. Chem. Lett.* **2012**, *3*, 2719–2723. (b) Korovina, N.; Joy, J.; Feng, X.; Feltenberger, C.; Krylov, A. Bradforth, S.; Thompson, M. *J. Am. Chem. Soc.* **2018**, *140*, 10179–10190. (c) Bakouri, O.; Smith, J.; Ottosson, H. *J. Am. Chem. Soc.* **2020**, *142*, 5602–5617.
- [15] Burdett, J. J.; Bardeen, C. J. *J. Am. Chem. Soc.* **2012**, *134*, 8597–8607.
- [16] Korovina, N. V.; Das, S.; Nett, Z.; Feng, X.; Joy, J.; Haiges, R.; Krylov, A. I.; Bradforth, S. E.; Thompson, M. E. *J. Am. Chem. Soc.* **2016**, *138*, 617–627.
- [17] Johnson, J. C.; Nozik, A. J.; Michl, J. *J. Am. Chem. Soc.* **2010**, *132*, 16302–16303.
- [18] Eaton, S. W.; Shoer, L. E.; Karlen, S. D.; Dyar, S. M.; Margulies, E. A.; Veldkamp, B. S.; Ramanan, C.; Hartzler, D. A.; Savikhin, S.; Marks, T. J.; Wasielewski, M. R. *J. Am. Chem. Soc.* **2013**, *135*, 14701–14712.
- [19] Musser, A. J.; Maiuri, M.; Brida, D.; Cerullo, G.; Friend, R. H.; Clark, J. *J. Am. Chem. Soc.* **2015**, *137*, 5130–5139.
- [20] Ni, W.; Gurzadyan, G. G.; Zhao, J.; Che, Y.; Li, X.; Sun, L. *J. Phys. Chem. Lett.* **2019**, *10*, 2428–2433.
- [21] Lukman, S.; Richter, J. M.; Yang, L.; Hu, P.; Wu, J.; Greenham, N. C.; Musser, A. J. *J. Am. Chem. Soc.* **2017**, *139*, 18376–18385.
- [22] Varnavski, O.; Abeyasinghe, N.; Aragón, J.; Serrano-Pérez, J. J.; Ortí, E.; López Navarrete, J. T.; Takimiya, K.; Casanova, D.; Casado, J.; Goodson, T. *J. Phys. Chem. Lett.* **2015**, *6*, 1375–1384.
- [23] Zeng, T.; Ananth, N.; Hoffmann, R. *J. Am. Chem. Soc.* **2014**, *136*, 12638–12647.
- [24] Nagami, T.; Okada, K.; Miyamoto, H.; Yoshida, W.; Tonami, T.; Nakano, M. *J. Phys. Chem. C* **2020**, *124*, 11800–11809.
- [25] Nagami, T.; Miyamoto, H.; Yoshida, W.; Okada, K.; Tonami, T.; Nakano, M. *J. Phys. Chem. A* **2020**, *124*, 6778–6789.
- [26] Singh, A.; Humeniuk, A.; Röhr, M. I. S. *Phys. Chem. Chem. Phys.* **2021**, *23*, 16525–16536.
- [27] Liu, Z.; Lu, T.; Chen, Q. *Carbon* **2020**, *165*, 461–467.
- [28] Pope, M.; Geacintov, N. E.; Vogel, F. *Mol. Cryst.* **1969**, *6*, 83–104.
- [29] Jundt, C.; Klein, G.; Sipp, B.; Le Moigne, J.; Joucla, M.; Villacys, A. A. *Chem. Phys. Lett.* **1995**, *241*, 84–88.

ECOLE DOCTORALE :
(SEA)

LABORATOIRE :
(IPREM)

CONTACT

(chen.zhang@univ-pau.fr)